Peter Pippan

Quantum Monte Carlo Simulations of Bosonic Systems

DOCTORAL THESIS

For obtaining the academic degree of

Doktor der Technischen Wissenschaften

Doctoral Programme of Technical Sciences
Technical Physics

Graz University of Technology

Graz University of Technology

Betreuer:
Ao.Univ.-Prof. Dipl.-Phys. Dr.rer.nat. Hans Gerd EVERTZ

Institute of Theoretical and Computational Physics

Graz, October 2010

Deutsche Fassung:
Beschluss der Curricula-Kommission für Bachelor-, Master- und Diplomstudien vom 10.11.2008
Genehmigung des Senates am 1.12.2008

EIDESSTATTLICHE ERKLÄRUNG

Ich erkläre an Eides statt, dass ich die vorliegende Arbeit selbstständig verfasst, andere als die angegebenen Quellen/Hilfsmittel nicht benutzt, und die den benutzten Quellen wörtlich und inhaltlich entnommene Stellen als solche kenntlich gemacht habe.

Graz, am ……. ……..
(Unterschrift)

Englische Fassung:

STATUTORY DECLARATION

I declare that I have authored this thesis independently, that I have not used other than the declared sources / resources, and that I have explicitly marked all material which has been quoted either literally or by content from the used sources.

……. ……..
date (signature)

Abstract

In this thesis several strongly correlated bosonic systems are studied by means of Quantum Monte Carlo (QMC). The QMC method is introduced and first applied to cold atoms in optical lattices as well as a to a recently proposed system of coupled light modes in cavities. The Bose–Hubbard model is studied in one and two dimensions with and without a parabolic confining potential. The cavities are described by the so called Jaynes–Cummings–Hubbard model which is studied in one dimension. Although these two models describe completely different systems, the physics is similar in many respects – even in their dynamical properties.

The focus lies on the calculation of excitation spectra such as the dynamical structure factor and one particle spectral functions. These quantities are accessible experimentally by means of spectroscopy, which has recently been applied to cold atomic systems. A comparison to approximate methods is made. This is important since most of the experimental data is compared to such calculations, like mean field or Bogoliubov approaches. It is shown, in which regions of the phase diagram of the Bose–Hubbard model such approaches give reasonable results when dynamical properties are investigated and more importantly, where more involved calculations should be used.

Furthermore, the Holstein model which is a model of spinless fermions that couple to phononic degrees of freedom is investigated. To this end an extension to an existing method is introduced. This method was developed for spin–Peierls systems in which the phonon degrees of freedom are sampled in Fourier space for each electron configuration in the Monte Carlo. Here a variant of the algorithm is presented, that uses a path integral representation of the electronic part of the partition sum instead of the stochastic series expansion (SSE) representation.

Again the main interest is in dynamical properties such as the dynamical structure factor or the phonon spectral function.

Kurzfassung

In dieser Arbeit werden verschiedene stark korrelierte Systeme, die bosonische Freiheitsgrade besitzen, mit Hilfe der Quanten Monte Carlo (QMC) Methode untersucht. Nach einer Einführung in die Methode werden ultrakalte Atome in optischen Gittern untersucht. Diese Systeme werden sehr gut durch das Bose–Hubbard Modell beschrieben, welches wir in einer und in zwei Dimensionen untersuchen. In einer Dimension wird weiters der experimentell interessante Fall mit einem zusätzlichen quadratisches Potential betrachtet. Weiters werden Systeme von gekoppelten Lichtmoden in Kavitäten untersucht, welche mit dem sogenannten Jaynes–Cummings–Hubbard Modell beschrieben werden. Obwohl das Bose–Hubbard Modell und das Jaynes–Cummings–Hubbard Modell sowohl formal sehr verschieden sind als auch sehr unterschiedliche Systeme beschreiben gibt es weitreichende Gemeinsamkeiten in der beobachteten Physik.

Das Hauptaugenmerk liegt in der Berechnung von dynamischen Größen, wie etwa der Einteilchen–Spektralfunktion. Diese Anregungsspektren sind mit spektroskopischen Methoden dem Experiment zugänglich und wurden kürzlich auch bei kalten Atomen gemessen. Wir vergleichen unsere Ergebnisse mit approximativen Ergebnissen, wie Mean Field oder Bogoliov Theorie, die häufig herangezogen werden um experimentelle Daten zu beschreiben. Wir zeigen in welchen Regionen des Phasendiagramms des Bose–Hubbard Modells solche Methoden korrekte Ergebnisse für spektrale Größen liefern und wo exakte Methoden herangezogen werden sollten.

Weiters untersuchen wir das Holstein Modell, welches freie spinlose Fermionen beschreibt, die an phononische Freiheitsgrade koppeln. Dazu wird eine existierende Methode erweitert, die entwickelt wurde um Spin–Peierls Modelle zu untersuchen indem die bosonischen Freiheitsgrade für jede elektronische Konfiguration im Fourier Raum behandelt werden.

In dieser Arbeit wird eine Variante des Algorithmus entwickelt, bei der eine alternative Darstellung für den elektronischen Teil der Zustandssumme verwendet wird.

Wiederum liegt der Fokus in der Berechnung dynamischer Größen, etwa der Phononen–Spektralfunktion oder des dynamische Strukturfaktors.

Table of Contents

Part I

Introduction

1 Outline of the Thesis

This thesis contains two major parts.

Part II deals with the simulation of artificial quantum systems, namely gases of cold atoms in optical lattices and so called quantum cavity electro dynamics which describes the interaction of light and matter in systems of coupled cavities.

The large amount of experimental achievements during the last years made it not only possible to produce Bose–Einstein condensed atoms. They have also been immersed into standing laser fields to create lattice models (e.g. the Bose–Hubbard model). The Mott insulator to superfluid transition [1] and many more phenomena from many-body physics have been observed (see Ref. [2] and references therein). Recently, even basic quantum excitations have been measured with spectroscopic accuracy in these artificial strongly correlated systems [3, 4].

However there are many experimental complications, like heating of the condensate due to the lattice lasers, which make an interpretation of results difficult. Thus it is important, that *unbiased* methods are applied to simulate these systems. Within this thesis, Quantum Monte Carlo (QMC) is used to obtain spectral properties as they are measured in the experiments mentioned above.

A different approach, using light modes in coupled cavities, that interact with two level systems, strongly correlated systems can be simulated as well. This experimental setup allows to construct Bose–Hubbard like models (the so called Jaynes–Cummings–Hubbard model) with the advantage of local addressability of sites (See Ref. [5] for a review). Again QMC is applied to obtain spectral properties and to investigate the phase transition that occurs in such models in more detail.

In chapter 3, these artificial quantum systems are explained in more detail.

Results are presented in chapter 4, which deals with dynamical properties of the Bose–Hubbard model in one dimension with constant chemical potential. This chapter mainly follows Ref. [6]. Furthermore, the Jaynes–Cummings–Hubbard model (see section 3.2) in one dimension is studied. The main focus lies apart from the unperturbative calculation of spectral properties on the comparison of the two models, which show very similar physics, even in their dynamical behavior. In chapter 5 results for the 2D Bose Hubbard model are presented. In particular, the effects of finite temperature on spectral properties are investigated. Finally, in chapter 6 the situation of cold atoms in a quadratic trapping potential in one dimension is studied. This case is most closely related to recent experiments.

In part III the Holstein model of spinless fermions, that treats the effects of phonons

on fermionic systems, is investigated. Different from the topics presented in part II, in a solid state system one has to rely on severe approximations to model certain properties. Thus it is important to include as many physical effects of the solid as possible. Here we address the problem of phonons, and how they affect the electronic system in a low dimensional solid. While part II *applies* well established methods the focus in part III lies on the algorithm itself. After a short introduction to the Holstein model (section 7.1) the algorithm is presented in detail in section 7.2. Benchmark results are presented in section 7.3.

Although the physics presented in the parts II and III is very different, we apply related Quantum Monte Carlo methods. The methods and the concepts they are based on are described in chapter 2.

A summary of the results can be found in chapter 8.

2 QMC Simulations of Strongly Correlated Systems

Strongly correlated systems are of great interest mainly in solid state physics for their unconventional physical properties such as high temperature superconductors of the cuprates and pnictides, colossal magneto-resistance in the manganities, one dimensional conductors and many others.

When there are strong correlations, local approaches such as density functional theory in the local density approximation do not work. The alternative approach is to find effective Hamiltonians that describe the important physical processes and that consider correlations between the main constituents (electrons, spins, phonons, etc.). A well–known example is the Hubbard model. It is hoped that variants of it describe high temperature superconductors. Unfortunately, despite its simplicity, there is no exact solution except for the one dimensional case and many analytical approaches suffer from uncontrollable approximations.

For many such models QMC is the method of choice since it suffers only from statistical errors without any systematical bias. Unfortunately for fermionic systems, QMC suffers from the infamous sign problem. Within this work we apply the method to bosonic systems, where no sign problem occurs.

In this chapter, a quick review of the methods used throughout this thesis is given. A review of the Quantum Monte Carlo methods can be found in [7, 8, 9].

2.1 Representations of the Partition Sum

All the QMC methods discussed in this thesis rely on the evaluation of observables

$$\langle O \rangle = \frac{1}{Z} \mathrm{Tr}(\hat{O} e^{-\beta \hat{H}}) = \frac{\mathrm{Tr}(\hat{O} e^{-\beta \hat{H}})}{\mathrm{Tr}(e^{-\beta \hat{H}})}, \tag{2.1}$$

with $\beta = 1/T$ the inverse temperature[1], some Hamiltonian $\hat{H}$ and the partition sum $Z = \mathrm{Tr}(e^{-\beta \hat{H}})$. A direct evaluation of the trace in not manageable on today's classical computers[2] due to the exponential size of the Hilbert space. We thus need a represen-

[1] If not otherwise noted, we leave out factors of $\hbar$ and the Boltzmann constant k_b.

[2] Since the problem is exponentially hard also an exponential growth of computer power does not solve the problem.

tation of the partition sum, such that we can apply a Monte Carlo scheme. That is, we want to draw configurations C out of the sum Eq. 2.1 such that the approximation $\langle O\rangle_{MC} = \frac{\sum_c O_c e^{-\beta E_c}}{\sum_c e^{-\beta E_c}}$ approaches the real expectation value.

In the subsections below, I shortly review two commonly used representations of the partition sum, the so called world line representation (sec. 2.1.1), which is a path integral evaluation of Z, and the *stochastic series expansion* (SSE) (sec. 2.1.2), which is a high temperature expansion in β.

Then, I will show in section 2.1.3 how one can map from one representation to the other to make use of the advantages of both. [10, 11, 12]

Furthermore I will shortly review the update algorithm used throughout this work in section 2.2.

2.1.1 Path Integral Representation

The path integral representation of lattice Hamiltonians presented below relies on the Suzuki-Trotter decomposition [13, 14] of the partition sum. The trick is to divide the Hamiltonian H into parts, where all terms in each part commute with each other. E.g. the simple tight binding Hamiltonian on a chain $\hat{H} = -t\sum \hat{a}_i^\dagger \hat{a}_{i+1} + h.c.$ is split into one part which acts only where i is even while the other part acts only for i odd

$$H = -t \sum_{i \text{ even}} \underbrace{(\hat{a}_i^\dagger \hat{a}_{i+1} + h.c.)}_{H_e} - t \sum_{i \text{ odd}} \underbrace{(\hat{a}_i^\dagger \hat{a}_{i+1} + h.c.)}_{H_o}. \tag{2.2}$$

All terms in H_e and H_o commute with each other while $[H_e, H_o] \neq 0$.

The partition sum is then written as a successive application of small imaginary time evolutions

$$\begin{aligned}
\mathrm{Tr}(e^{-\beta H}) =& \mathrm{Tr}(e^{-\Delta\tau(H_e+H_o)})^M \\
=& \mathrm{Tr}(e^{-\Delta\tau H_e} e^{-\Delta\tau H_o})^M + O(\Delta\tau^2) \\
=& \sum_{\{\alpha_1,\alpha_2,\ldots\alpha_{2m}\}} \underbrace{\langle\alpha_1|e^{-\Delta\tau H_e}|\alpha_2\rangle \langle\alpha_2|e^{-\Delta\tau H_o}|\alpha_3\rangle \ldots \langle\alpha_{2m}|e^{-\Delta\tau H_o}|\alpha_1\rangle}_{W(\{|\alpha_k\rangle\})} + O(\Delta\tau^2).
\end{aligned} \tag{2.3}$$

$|\alpha_k\rangle$ are complete basis sets - e.g. in the case of free fermions we chose the occupation number basis and the sum goes over all possible basis states. One can visualize this representation graphically (Fig. 2.1) by drawing shaded squares for the action of one operator $e^{-\Delta\tau H_e}$ or $e^{-\Delta\tau H_o}$. The configuration along each time slice corresponds to one of the states $|\alpha_k\rangle$. One usually connects particles on neighboring time slices with lines. Each of these so called "world line" configurations corresponds to one configuration of $\{|\alpha_k\rangle\}$ and thus to one term in Eq. 2.3 associated with some weight $W(\{|\alpha_k\rangle\}) \equiv W_{\mathrm{wc}}$.[3]

We finally arrived at a mapping from a d-dimensional quantum system to a $d+1$-dimensional classical system, which can now be sampled by standard Monte Carlo schemes. The Monte Carlo samples in the space of possible world line configurations.

[3] wc stands for world line configuration.

Observables can be evaluated as

$$\langle \hat{O} \rangle = \frac{\sum_{\mathrm{wc}} O_{\mathrm{wc}} W_{\mathrm{wc}}}{\sum_{\mathrm{wc}} W_{\mathrm{wc}}}, \tag{2.4}$$

meaning that $\langle \hat{O} \rangle$ is given as the average of some estimator O_{wc} over all sampled world line configurations

$$\langle \hat{O} \rangle = \langle O_{\mathrm{wc}} \rangle \tag{2.5}$$

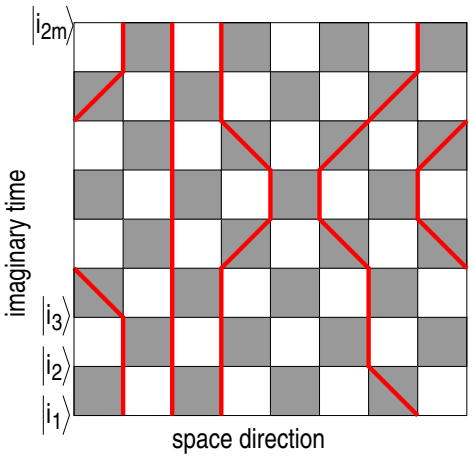

Figure 2.1: The Suzuki Trotter decomposition: Thick red lines connect sites which are occupied by one particle. These are the so called "worldlines".

The Suzuki-Trotter decomposition, as presented above, introduces a time discretization error which is proportional to $\Delta\tau^2$. However, when the representation of the model is discrete [4], it is possible to perform the continuum limit $\Delta\tau \to 0$ to get a path integral representation without any discretization error. Since the probability for a non-diagonal plaquette (jump of a world line from one site to an other) in the tight binding model is $\sinh(\Delta\tau\ t) \propto \Delta\tau \propto 1/M$, it follows that the number of jumps remains constant even in the limit $M \to \infty$. From a technical point of view, that means instead of storing the states in all of the $2M$ time slices one simply stores the times where a jump of a world line occurs.

We will perform this limit in section 7.2.1 in the context of the Holstein model.

2.1.2 Stochastic Series Expansion (SSE)

The *stochastic series expansion* (SSE) [15] is a generalization of a method invented by Handscomb [16, 17], which relies on a Taylor expansion of the partition sum. In the end, similar to the wordline formulation, we will derive a representation in terms of a $d+1$ dimensional classical system, which can by simulated by means of Monte carlo.

Given that the Hamiltonians we are interested in can be written as sum over – in general – non commuting operators that act on bonds $\hat{H} = \sum \hat{H}_b$. Here, $\hat{H}_b$ can be something like $a_i^\dagger a_j$ or $n_i + n_j$, where the sites i and j are connected by a bond.

Expanding the partition sum in a Taylor series reads

$$Z = \mathrm{Tr}\left(\sum_n \frac{(-\beta)^n}{n!} \hat{H}^n \right) = \sum_\alpha \sum_n \frac{\beta^n}{n!} \left\langle \alpha \middle| \left(\sum (-\hat{H}_b) \right)^n \middle| \alpha \right\rangle, \tag{2.6}$$

[4] This is already necessary for the worldline picture

where we chose some convenient set of basis states $\{|\alpha\rangle\}$. In most of the work presented this will be the occupation number basis $|n\rangle = |n_1\rangle \otimes |n_2\rangle \otimes \ldots |n_L\rangle$.

Since the operators $\hat{H}_b$ generally do not commute one has to sum over all possible expansions of $\left(\sum(-\hat{H}_b)\right)^n$. Let us call one expansion in the sum of $\hat{H}^n$

$$S_n := \prod_{i=1}^{n} \hat{H}_{b_i}^{t_i} \tag{2.7}$$

an *operator string* S_n of length n, where b_i labels the bond on which the operator acts and t_i should be the type of the operator (e.g. density-density interaction, spin-flip, or hopping). One usually includes identity operators $\hat{H}^1 = \mathbb{1}$ to get rid of the sum over n in Eq. 2.6. Thus one operates only on one operator string of length L, that has $n < L$ non unitary operators.[5] The partition sum finally becomes

$$Z = \sum_{\alpha} \sum_{\{S_L\}} \underbrace{\frac{\beta^n (L-n)!}{L!} \left\langle \alpha \left| \prod_{i=1}^{L} (-\hat{H}_{b_i}^{t_i}) \right| \alpha \right\rangle}_{W(S_L,\alpha)}. \tag{2.8}$$

With that at hand one can formulate a Monte Carlo algorithm that samples in the space of possible operator strings and states $(S_L,|\alpha\rangle)$. That is of course only possible if the weight function $W(S_L, \alpha)$ is always positive or zero, i.e. all matrix elements of each bond operator have to be negative or zero. For diagonal operators one can always add a constant to the Hamiltonian to ensure that.[6]

Unfortunately for non diagonal operators this simple trick does not work. However for many Hamiltonians one can show that only an even number of negative signs in the product of Eq. 2.8 occurs and thus the Monte Carlo is sign problem free in many cases (e.g. for bosons or for spins on non frustrated lattices).

One can represent one configuration in the partition sum graphically as operators H_b acting on some state $|\alpha\rangle$ (see Fig. 2.2). The trace in Eq. 2.8 ensures "periodic boundary conditions" in the index direction. From Fig. 2.2 one can already see, that SSE resembles the wordline picture. Again we have "worldlines" connecting states with the same local quantum number.

Given the weight $W(S_L, \alpha)$ of each configuration, one can easily calculate expectation values of observables as

$$\langle \hat{O} \rangle = \frac{\sum_{\alpha} \sum_{\{S_L\}} O(\alpha, S_L) W(S_L, \alpha)}{\sum_{\alpha} \sum_{\{S_L\}} W(S_L, \alpha)}, \tag{2.9}$$

[5] In principle one has to sum over all lengths L of the operator string too. But one can chose L very large and increase the size if n becomes comparable large.

[6] One should not forget to subtract the constant from the energy in the end.

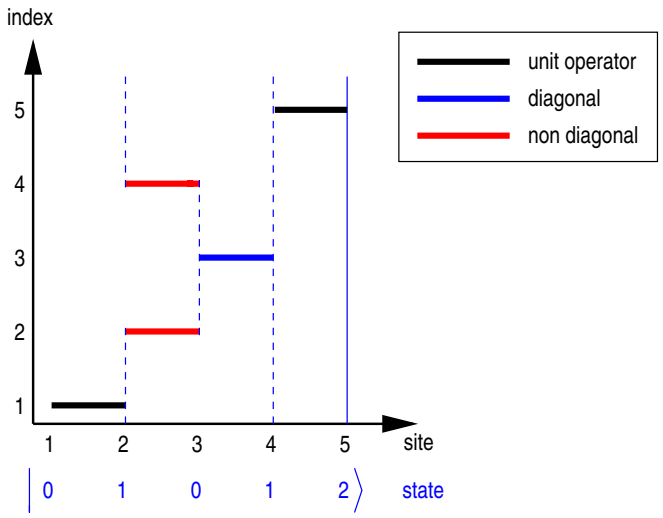

Figure 2.2: Graphical representation of one configuration of the partition sum (S_L,$|\alpha\rangle$). Thick horizontal lines represent operators. States are represented by vertical lines (no line $\sim |0\rangle$, dashed line $\sim |1\rangle$), and solid line $\sim |2\rangle$).

that is, the simulation estimate $\langle \hat{O} \rangle$ is given by the average of the estimator $O(\alpha, S_L)$ over the sampled configurations

$$\langle \hat{O} \rangle = \langle O(\alpha, S_L) \rangle \,. \tag{2.10}$$

For many observables, there exist simple estimators. E.g. the internal energy $E = \langle \hat{H} \rangle$ involves only the number of non identity operators n [18]

$$E = -\langle n \rangle / \beta, \tag{2.11}$$

and the heat capacity is simply given by [18]

$$C = \langle n^2 \rangle - \langle n \rangle^2 - \langle n \rangle \,. \tag{2.12}$$

2.1.3 Mapping from SSE to a Path Integral Representation

As shown above, there exist many estimators for observables that can be calculated very easily in the SSE representation. Unfortunately it is very cumbersome to obtain correlation functions like $\langle \hat{O}_i(\tau) \hat{O}_j(0) \rangle$ since they involve a convolution of Green's functions at different SSE distances. Even with very involved methods most of the computational time is consumed by the calculation of correlation functions.[19]

Thus although the SSE representation is convenient from a computational point of view, since only integer values need to be assigned in the operator index sequence, it becomes inefficient when correlation functions are measured.

In Ref. [20] it has been shown that a MC procedure can be directly formulated in a continuous time formulation of the path integral. For Hamiltonians of the form

$$\hat{H} = \hat{H}_0 + \hat{V} \tag{2.13}$$

with diagonal and off-diagonal parts $\hat{H}_0$ and $\hat{V}$ respectively, one performs the standard time–ordered perturbation expansion in $\hat{V}$

$$\begin{aligned} Z = \sum_{n=0}^{\infty} (-1)^n \int_0^{\beta} d\tau_n \dots \int_0^{d\tau_2} \tau_2 \int_0^{d\tau_1} \tau_1 \\ \times \mathrm{Tr}[e^{-\beta H_0} V(\tau_1) V(\tau_2) \dots V(\tau_n)]. \end{aligned} \tag{2.14}$$

In Ref. [10] it has been shown, that using this perturbation also the update schemes developed for the SSE representation can be used.

Michel and Evertz showed [11, 12], that the problem of measuring Green's functions in an SSE simulation can be solved by going one step further. By doing the perturbation expansion in all terms of the Hamiltonian instead of $\hat{V}$ one can directly map an SSE operator string to a continuous time world line representation. One can then perform the MC updates in the SSE representation – having only integer values to operate with – and perform measurements of time dependent correlations in continuous time with nearly no extra computational cost.

In practice the SSE operator string S_L is updated using standard schemes. Then a time $0 < \tau < \beta$ is assigned stochastically to each operator in S_L. The times must be sampled uniformly out of $[0, \beta)$. We do that by sampling $L + 1$ distances $\Delta\tau_i$ out of a Poisson distribution and calculate the times using

$$\tau_i = \frac{\beta \sum_{k=1}^{i} \Delta\tau_k}{\sum_{k=1}^{L+1} \Delta\tau_k}. \tag{2.15}$$

Doing that one arrives at a valid world line configuration. Graphically one can visualize that by going from (c) → (b) in Fig. 2.3 (The diagonal terms are taken into account by imaginary time evolution in the world line picture). For diagonal[7] operators $\hat{O}$ correlation functions like $\langle \hat{O}_i(\tau) \hat{O}_j(0) \rangle$ can then directly be measured. For off diagonal operators like $\langle \hat{a}\ (\tau) \hat{a}_j^{\dagger}(0) \rangle$ this is slightly more complicated and will be discussed below. However also in that case the computational extra cost is negligible.

[7] diagonal in the chosen basis $\{|\alpha\rangle\}$

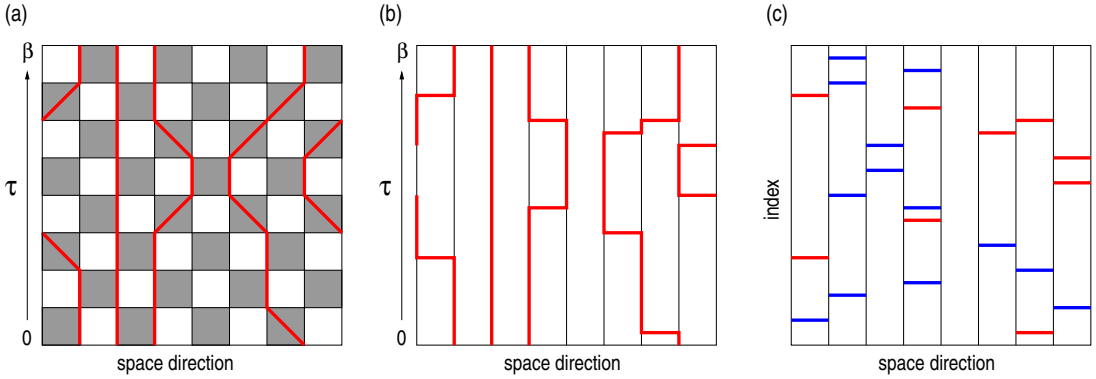

Figure 2.3: Equivalence of the world line representation and SSE of the partition sum. Suzuki-Trotter decomposition (a), continuous time path integral representation (b), and SSE (c). The continuous time in the path integral is replaced by an integer index in the operator string, at the cost of diagonal terms (blue lines).

2.2 Efficient Monte Carlo Update Schemes

In the previous chapter, we showed how to map quantum system onto classical world lines. In this representation standard Metropolis Monte Carlo algorithms with local updates of the configuration are applicable. This approach however suffers from critical slowing down at second order phase transitions. Furthermore the number of world lines remains unchanged, meaning that simulations have to be performed at constant particle number or magnetization.

A solution to these problem was provided by the loop algorithm [21, 9], which was originally formulated in discrete imaginary time, but later extended to continuous time [22]. There exist other methods like the worm algorithm [23], the operator loop update [24] or, as a generalization, the directed loop algorithm [25], which have in common, that they construct some path – either in world line picture or the SSE – along which the quantum number is changed. The construction of the path follows local rules, while the change of the configuration is of global nature.

A sketch of the procedure can be seen in Fig. 2.4. In that case a continuous time world line representation is used, but the idea is the same in the SSE representation. Given some valid worldline configuration (Fig. 2.4 (a)), an operator pair $\hat{a}^\dagger\ \hat{a}$ is inserted. One usually calls one of them loop head and the other one loop tail. The loop head moves around in the space–time plane changing the local state. The movement is governed by local rules. This is continued until the head hits the tail of the loop again (Fig. 2.4 (b)). When the loop is closed, we finally arrive at a valid world line configuration, that is globally different from the original one (Fig. 2.4 (c)).

Using such update algorithms one can simulate large systems at very low temperature due to very small auto-correlation times.

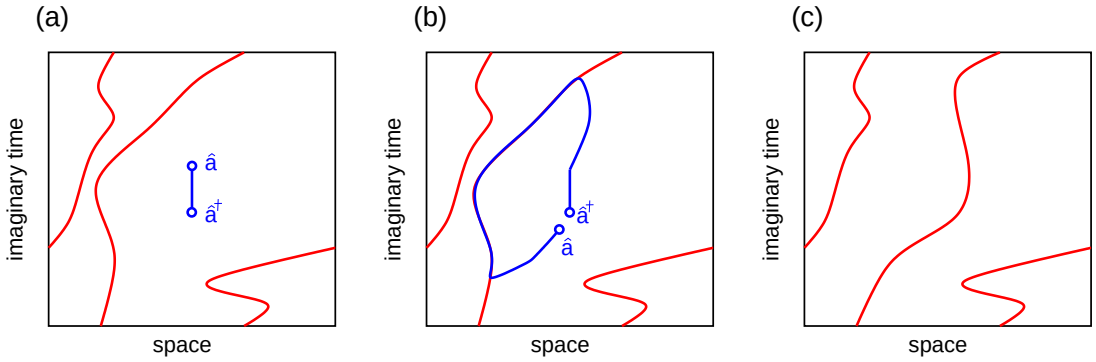

Figure 2.4: Directed loop algorithm: Starting from a valid world line configuration, an operator pair $\hat{a}^\dagger\ \hat{a}$ is inserted (a). The loop head $\hat{a}$ moves around following *local* rules until it hits the loop tail $\hat{a}^\dagger$ again (b), arriving at a valid world line configuration (c).

Within this work we use the directed loop algorithm in the SSE representation in part II and in a path integral representation in part III of this thesis. In section 7.2.1 we demonstrate how to obtain the rules for the movement of the loop head.

2.2.1 Simulation of Bosonic Systems

Within this thesis, mainly bosonic systems are investigated. For bosonic problems these methods are extremely well suited, since there is no sign problem as long, as there is no geometric frustration.

In part II a straight forward application of the directed loop algorithm is applied. That is, one uses the bosonic occupation number as basis states $|\alpha\rangle$ and restricts the maximum number of allowed bosons per site to some number N_{max}. We check throughout the simulation, that $|N_{max}\rangle$ is never reached. Thus we are able to simulate bosonic systems *without* any systematic errors.

In part III a different approach is applied to the Holstein model of spinless fermions. In that model, (bosonic) phonon modes couple to otherwise free fermions. We show in detail in section 7.2 how an efficient update of the phonon degrees of freedom can be formulated in Fourier space.

2.2.2 Measurement of the Propagator

During the loop update the configuration is not a valid contribution to the partition sum. However one can directly measure the propagator $\langle \hat{a}_i(\tau)\hat{a}_j^\dagger(0)\rangle$ during the movement of the loop head. To this end, we introduce some time grid to measure the time dependent correlation function only on discrete times $0, \Delta\tau, 2\Delta\tau, \ldots$. Whenever the loop head crosses a time slice we measure the propagator at one specific distance in space and imaginary time.

Here, $\Delta\tau$ has nothing to to with the time discretization of the Suzuki-Trotter decomposition, but limits only the maximum energy $E_{max} \sim 1/\Delta\tau$ that can be investigated.

2.3 Inversion of Dynamical Correlation Functions

The main interest is of course not into imaginary time dependent correlation functions, but into quantities that are experimentally accessible. In particular, we want to calculate ARPES/IPES spectra $A(k,\omega)$, the dynamical structure factor $S(k,\omega)$ – which is obtained by Bragg spectroscopy – or the phonon spectral function $S_x(k,\omega)$.

Let us discuss only the one particle spectral function $A(k,\omega)$. The discussion for $S(k,\omega)$ and $S_x(k,\omega)$ follows the same arguments and will be described in part II and III in more detail.

$A(k,\omega)$ is given in the spectral representation as

$$A(k,\omega) = \frac{1}{Z}\sum_{m,n} |\langle m|\hat{a}^\dagger|n\rangle|^2 e^{-\beta E_n}(e^E - \varepsilon)\delta(E-(E_n - E_m)), \tag{2.16}$$

where $\varepsilon = -1$ for the fermionic version of Eq. 2.16 and $\varepsilon = +1$ for the bosonic one, respectively.

In the fermionic case, one can relate the spectral function to the propagator via

$$\langle \hat{a}_k(0)\hat{a}_k^\dagger(\tau)\rangle = \int_{-\infty}^{\infty} d\omega \frac{A(k,\omega)}{e^{\beta\omega}+1} e^{-\omega\tau}. \tag{2.17}$$

Unfortunately the inversion of the equation above is very ill conditioned. Since the correlation function is subject to statistical errors, we can not invert Eq. 2.17 in a straight forward way.

A solution to the problem was given with *maximum entropy* methods [26, 27].

This is used to invert Eq. 2.17 as well as a similar equation to get the dynamic structure factor by inverting the density–density correlation function or the phonon spectral function out of the phonon–phonon correlation function $\langle x_{-k}(\tau)x_k(0)\rangle$.

2.3.1 Note on Fourier Transformation

We measure the propagator in real space, i.e. as a function of spatial distances $i-j$. However we need it in $k-$space (see Eq. 2.17) to obtain the spectral function. One can simply calculate the k-spece dependent correlation function with a Fourier transformation.

Care must be taken since the propagator in real space is not only subject to statistical errors, but the data may be strongly correlated, thus a straight forward error propagation is not applicable. How to perform the calculation properly with the Jackknife method is described in appendix A.

Part II

Quantum Simulators

3 Using Cold Atoms and Cavity Systems as Quantum Simulators

The two dimensional fermionic Hubbard model is just one example of a model that describes interesting physics, probably realized in, e.g. high temperature superconductors, but which remains unsolved. Although there exist many approximate methods, there is no analytical solution nor does the QMC work well away from half filling – which is the region of interest – due to a severe sign problem. Also variational methods like the DMRG which are extremely efficient in one dimension can not be applied to higher dimensional problems so far. But not only the 2D Hubbard model, also frustrated spin systems suffer from the problem, that there are no efficient algorithms for classical computers.

The situation would be different if one could build a quantum computer, where all these quantum problems could be simulated in polynomial time. Although one is still far away from assembling a quantum computer that can be used like today's classical computers, with the fabrication of ultra cold quantum gases in optical lattices it has been possible to simulate strongly correlated quantum systems experimentally [28, 1, 2]. Current cooling techniques allow to Bose-condense cold atoms and to transfer the Bose–Einstein condensate (BEC) into optical lattices which are then a nearly ideal realization of a bosonic Hubbard model. The ultimate goal is the realization of fermionic Hubbard models, but with today's cooling techniques this is still out of reach.

The goal of this work was to calculate various properties of bosonic systems that can be built also experimentally. The Bose–Hubbard model as well as the Jaynes–Cummings–Hubbard model (which we will discuss in subsequent chapters) can be simulated with the QMC method without any systematic errors. It is very important to have unbiased methods at hand, because although strongly correlated models have never been *built* that cleanly before, there are still many technical problems that need to be fully understood. E.g. due to the influence of lattice- or measurement lasers, the condensate is heated significantly. Further more it is a quite subtle task to measure temperatures at all. Having an unbiased method at hand for the calculation of thermal properties can thus be of great importance for the understanding of many experimental results.

In particular we are interested in the calculation of spectral properties such as the one particle spectral function or the dynamic structure factor.

In the subsequent sections 3.1 and 3.2 a short review of the basic concepts of these

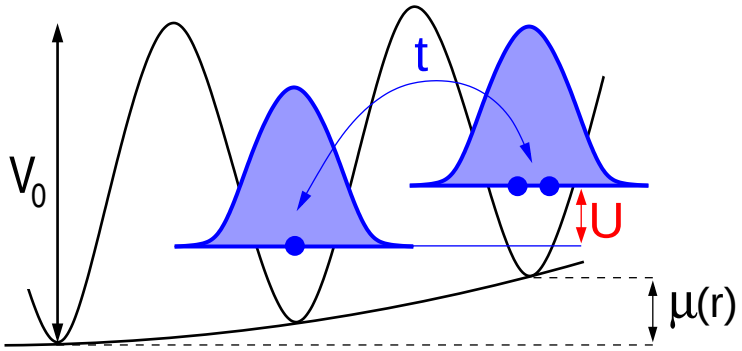

Figure 3.1: Sketch of the energy scales involved in a cold atom gas in an optical lattice. The laser intensity V_0 is directly related to the hopping integral t and the on-site energy U. A trapping potential $\mu(r)$ keeps the atoms localized.

artificial systems that simulate strongly correlated systems is given. In the chapers 4-6 QMC results are presented.

3.1 Ultra-cold atoms in optical lattices

As proposed by Jaksch *et al.* [28] Bose-Einstein condensed atoms transferred to an optical lattice are extremely well described by the Bose–Hubbard model

$$\hat{H} = -t \sum_{\langle i,j \rangle} \hat{a}_i^\dagger \hat{a}_j + \frac{U}{2} \sum_i \hat{n}_i(\hat{n}_i - 1) - \sum_i \mu_i \hat{n}_i. \tag{3.1}$$

$\hat{a}_i^\dagger$ and $\hat{a}_j$ are bosonic creation and annihilation operators respectively, $[\hat{a}_j, \hat{a}_i^\dagger] = \delta_{i,j}$. $\hat{n}_i$ is the density operator and $\langle \cdot \rangle$ symbolizes a sum over nearest neighbors.

The cold atoms are usually trapped in a magneto–optical trap. The trapping potential $\mu(\mathbf{r}) = K\mathbf{r}^2$ localizes the Bose–Einstein condensate. Two counter-propagating laser beams generate a periodic potential, which can be one, two, or three dimensional. Due to an AC Stark shift the atoms feel a periodic potential with height V_0 – which can of course be different for each dimension. If V_0 is strong enough, the atoms tend to localize around the minima of the potential. Each minimum is, in the description of Eq. 3.1, one lattice site $i, j, \ldots$ respectively. The overlap integral of neighboring atoms is the hopping strength t. If two or more atoms are on the same lattice site the Coulomb energy U has to be payed (Fig. 3.1).

Jaksch *et al.* [28] assumed that the bosons are, expressed in the Wannier basis, in their lowest vibrational state $w(\mathbf{x})$. They calculated the Coulomb repulsion strength

$$U = 4\pi a_s \hbar^2 \int d^3x |w(\mathbf{x})|^4 / m$$

and the hopping integral

$$t = \int d^3x \; w^*(\mathbf{x} - \mathbf{x}_i) \left[-\frac{\hbar^2}{2m}\nabla^2 + V_0(x) \right] w(\mathbf{x} - \mathbf{x}_i).$$

Thus given the Wannier functions $w(\mathbf{x})$ and the s-wave scattering length a_s one can determine the parameters of the model numerically.

To assure that the bosons are in their lowest vibrational level, V_0 has to be strong enough. A convenient measure for the strength of V_0 is the so called recoil energy $E_r = \hbar^2 k^2/2m$, with k the wave-number of the standing laser beam. If $V_0 \gg E_r$ an exact result for t and U was found [29]

$$t = \frac{4}{\sqrt{\pi}} E_r \left(\frac{V_0}{E_r} \right)^{3/4} e^{-2\sqrt{V_0/E_r}}, \tag{3.2}$$

$$U = \sqrt{\frac{8}{\pi}} k a_s E_r \left(\frac{V_0}{E_r} \right)^{3/4}. \tag{3.3}$$

In typical experiments V_0 can be as high $V_0 \approx 20 - 30 E_r$ which corresponds to very deep Mott insulators. However, if V_0 is that large the heating of the condensate should not be neglected anymore. If the superfluid state of the Bose Hubbard model is studied, where $V_0 \gg E_r$ is not given anymore, one should also consider higher order terms in the evaluation of the parameters t and U of the model.

Apart from the Mott insulator to superfluid transition [1], many more experiments have been performed that demonstrated interesting many body physics with such systems (See Ref. [2] and references therein).

In recent experiments also dynamical properties have been measured using Bragg spectroscopy [30, 3, 31, 4]. This allows to determine the dynamical structure factor as well as the one particle spectral function.

3.2 The Jaynes–Cummings–Hubbard model

As seen in the last section, cold atoms in optical lattices allow to build strongly correlated models and to fine tune the parameters very precisely. Since the lattice spacing is on the order of hundreds of nanometers, it is however very difficult – but not impossible, as recently shown [32] – to perform *local* measurements. In this section we describe another approach in which also single sites can be addressed. This artificial system, that has recently been proposed to use as a quantum simulator consists of arrays of cavities in which atoms interact with photons [33, 34, 35, 36, 5]. See figure 3.2 for a sketch. Photons and atoms usually interact only very weakly. This interaction can be increased significantly, when the light is put into a resonator. Let us consider only one such light mode in the i-th cavity coupled to a simple two-level system. This simple

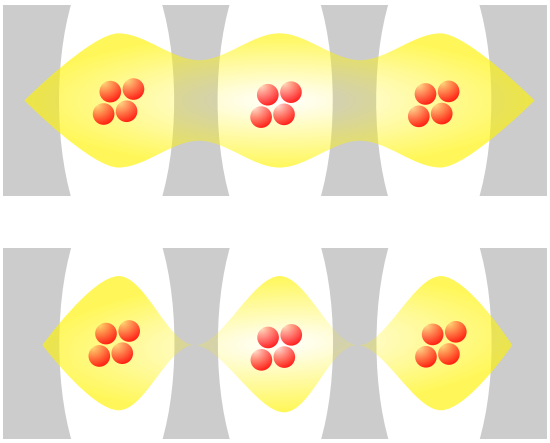

Figure 3.2: The photons (yellow) inside of a cavity array that can move freely (top) might be dressed due to strong atom-photon coupling (bottom).

system is very well described – using the dipole and rotating wave approximations – by the Jaynes–Cummings Hamiltonian [37]

$$\hat{H}_i^{\mathrm{JC}} = \varepsilon \left|\uparrow\right\rangle_i \left\langle\uparrow\right|_i + \omega_0 \, \hat{a}_i^\dagger \hat{a}_i + g \left(\left|\uparrow_i\right\rangle \left\langle\downarrow_i\right| \hat{a}_i + \left|\downarrow_i\right\rangle \left\langle\uparrow_i\right| \hat{a}_i^\dagger \right) . \tag{3.4}$$

We denote the two levels of the atom as $|\downarrow\rangle$ and $|\uparrow\rangle$ respectively. The photon field is described in the occupation number basis with creation and annihilation operators $a^\dagger$ and a. ω_0 and ε are the frequencies of the resonant mode of the cavity and the atomic transition, respectively. g is the coupling of the photon to the two-level system.

In addition to the coherent transition as described in Eq. 3.4, there are two main loss processes: On the one hand there is spontaneous emission from $|\uparrow\rangle$ to $|\downarrow\rangle$ with a rate γ and on the other hand photons of the cavity mode are lost with a rate κ. A convenient measure for the coherence of the system is the so called *cooperativity factor*

$$\xi = \frac{g^2}{2\kappa\gamma}, \tag{3.5}$$

which should be $\xi \gg 1$ for the coherent processes to dominate over loss processes (Fig. 3.3 (a)).

Up to now we only considered one cavity. Interesting strongly correlated physics is observed, if these cavities are coupled to each other (see Figures 3.2 and 3.3 (b)). A small overlap of the wave-functions of neighboring light modes allows the hopping of photons from one cavity to a neighboring one.

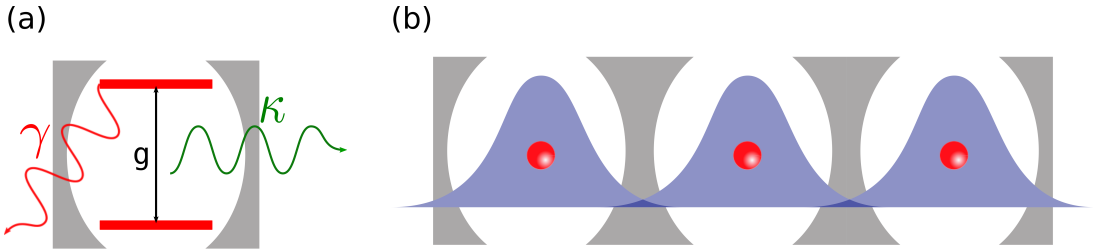

Figure 3.3: (a) One two-level system in an array interacting with a photon mode. If the cavity decay rate κ and spontaneous emission rate γ is small, the system is described by Eq. 3.4. (b) Coupled cavities: each cavity is described by the Jaynes Cummings Hamiltonian Eq. 3.4 with a two level system (red dots) and light modes (blue). A small overlap of photon wave-functions allows the photon to hop to a neighboring cavity.

This is described by the so called Jaynes–Cummings–Hubbard Hamiltonian

$$\hat{H} = \sum_i \hat{H}_i^{\mathrm{JC}} - t \sum_{\langle i,j \rangle} (\hat{a}_i^\dagger \hat{a}_j + h.c.) + \sum_i \mu \underbrace{\left(|\uparrow\rangle \langle\uparrow| + \hat{a}_i^\dagger \hat{a}_i \right)}_{N_p}. \tag{3.6}$$

We defined the conserved quantity of the polariton number N_p.

Interestingly, even though there is no strong coupling term (like $\hat{n}_i \hat{n}_i$ in the Bose Hubbard model Eq. 3.1), this model not only has a very similar phase diagram as the Bose Hubbard model, but also shows many other features of a strongly correlated model.

This is due to an effective repulsive polariton–polariton interaction U_{eff} mediated by the atom–photon coupling. For the Jaynes–Cummings model on one site, with $\omega_0 = \varepsilon$ the energy to add one polariton to the system can be calculated exactly as $U_{eff} = g\sqrt{n}$, where n is the polariton number. This resembles the Coulomb repulsion strength U in the Hubbard model.

Results will be presented in chapter 4, together with a detailed comparison to the Bose–Hubbard model.

3.2.1 Experimental Realizations

Experimental realizations of large arrays of such cavities have still not been built, however there are many promising candidates for such systems (See Ref. [5] and references therein):

- Quantum dots coupled to photonic band gap cavities reach $\xi \sim 10$ and $\xi \sim 10^6$ have been predicted. Currently, spontaneous emission rates and the fact that it is hard to produce a large array limits this approach.

- Another approach for building arrays of cavities uses silicon structures of a disc or a toroidal shape. To realize the Hamiltonian Eq. 3.6 atoms are placed close to the surface of the discs, where cooperativity factors of $\xi \sim 50$ are reached. The main challenge using this approach is to keep the atoms trapped for a sufficiently long time.

- It has been reported that optical fibres have been used to transfer the photons between Fabri-Pérot cavities. The cavities are formed between the tips of two fibres which are placed on top of an atom chip. Within this approach high cooperativity factors of $\xi = 145$ can be reached. However due to the optical fibres the hopping term in Eq. 3.6 might get modified.

- Cooper-pair boxes coupled to superconducting transmission line resonators are a promising experimental architecture to realize the Jaynes–Cummings–Hubbard Hamiltonian in the microwave regime. Cooper pair boxes are two superconducting islands, connected with an Josephson junction. These systems are coupled with quasi one-dimensional waveguides, which are formed on a chip and have resonance frequencies in the microwave range. It has been predicted that up to 10 of such boxes can be coupled.

To conclude, in contrast to realizations of the Bose–Hubbard model in terms of optical lattices, implementations of the Jaynes–Cummings Hubbard model would allow to address singles sites. Unfortunately it seems to be rather difficult to build large lattices with current technologies. Furthermore such systems need to be driven by some external field, such as a pumping laser. Thus it would be more appropriate to describe a steady state instead of the thermal state. However at least in the case of only one site, the steady state is equivalent to the thermal state. Also in the weak pumping limit, i.e. the hopping processes are much faster than the pump rate, a decription in terms of thermal states is valid.

4 Dynamics of One Dimensional Bose Hubbard and Polariton Models

PHYSICAL REVIEW A **80**, 033612 (2009)

Excitation spectra of strongly correlated lattice bosons and polaritons

Peter Pippan,[1] Hans Gerd Evertz,[1] and Martin Hohenadler[2,*]
[1]*Institute for Theoretical and Computational Physics, TU Graz, 8010 Graz, Austria*
[2]*Cavendish Laboratory, University of Cambridge, Cambridge CB3 0HE, United Kingdom*
(Received 20 April 2009; published 16 September 2009)

Spectral properties of the Bose-Hubbard model and a recently proposed coupled-cavity model are studied by means of quantum Monte Carlo simulations in one dimension. Both models exhibit a quantum phase transition from a Mott insulator to a superfluid phase. The dynamic structure factor $S(k,\omega)$ and the single-particle spectrum $A(k,\omega)$ are calculated, focusing on the parameter region around the phase transition from the Mott insulator with density one to the superfluid phase, where correlations are important. The strongly interacting nature of the superfluid phase manifests itself in terms of additional gapped modes in the spectra. Comparison is made to recent analytical work on the Bose-Hubbard model. Despite some subtle differences due to the polaritonic particles in the cavity model, the gross features are found to be very similar to the Bose-Hubbard case. For the polariton model, emergent particle-hole symmetry near the Mott lobe tip is demonstrated and temperature and detuning effects are analyzed. A scaling analysis for the generic transition suggests mean-field exponents, in accordance with field-theory results.

DOI: 10.1103/PhysRevA.80.033612 PACS number(s): 03.75.Kk

This chapter follows Ref. [6] almost literally.

4.1 Abstract

Spectral properties of the Bose-Hubbard model and a recently proposed coupled-cavity model are studied by means of quantum Monte Carlo simulations in one dimension. Both models exhibit a quantum phase transition from a Mott insulator to a superfluid phase. The dynamic structure factor $S(k,\omega)$ and the single-particle spectrum $A(k,\omega)$ are calculated, focusing on the parameter region around the phase transition from the Mott insulator with density one to the superfluid phase, where correlations are important. The strongly interacting nature of the superfluid phase manifests itself in terms of additional gapped modes in the spectra. Comparison is made to recent analytical work on the Bose-Hubbard model. Despite some subtle differences due to the polaritonic particles in the cavity model, the gross features are found to be very similar to the Bose-Hubbard case. For the polariton model, emergent particle-hole symmetry near the Mott lobe tip is demonstrated, and temperature and detuning

effects are analyzed. A scaling analysis for the generic transition suggests mean field exponents, in accordance with field theory results.

4.2 Introduction

The Mott insulator (MI) to superfluid (SF) quantum phase transition in the generic Bose-Hubbard model[38] has attracted a lot of attention in recent years due to the progress in experiments on cold atomic gases in optical lattices.[39] More recently, there have also been significant advances in the coherent coupling of single atoms and cold atomic gases to cavity radiation (cavity quantum electrodynamics).[40, 41] A clean realization of the Jaynes-Cummings Hamiltonian has been achieved by coupling a superconducting qubit to a microwave cavity.[42] On the theory side, multi-component Bose gases coupled to light have e.g. been shown to support a superradiant Mott insulator phase with polariton condensation.[43]

In parallel, several theoretical proposals have shown the possibility of having a state of strongly correlated photons or polaritons in solid-state systems of coupled cavity arrays (also referred to as polariton models or Jaynes-Cummings-Hubbard models),[33, 34] and a review of work along these lines has been given.[5] The possibility of preparing a system of photons in a Mott state with one photon per site is a promising starting point for quantum information processing. An important feature shared with cold atomic gases coupled to light is the composite nature of the polaritons. Particularly attractive properties of cavity arrays would include accessibility of local properties in measurements and scalability in terms of size. Perhaps the most likely candidate for setting up such a model experimentally is based on extending the work on superconducting qubits to arrays.[44, 42] In contrast to cold atomic gases, where the interaction and/or hopping strength can be varied, the phase transition may be observed by changing the detuning between the two-level system and the resonator. Analysis of coupled cavity models is fruitful in its own right, as a detailed understanding of the corresponding models offers insight into strongly correlated polariton systems. An important aspect of such studies is the extent to which such systems resemble the familiar Bose-Hubbard physics.

From the above examples and many more in the literature, it is apparent that interacting boson systems on a lattice are of great interest for the progress of both theory and experiment. Compared to Bose fluids, the lattice changes the physics in several aspects. Although long-range phase coherence still gives rise to phonon excitations—despite the breaking of translational symmetry—the quenching of the kinetic energy makes the system much more strongly correlated.[45] Besides, the lattice allows the formation of incompressible MI states with the same integer particle number at each site.

A large amount of work has been devoted to detailed studies of the Bose-Hubbard

model, leading to a wealth of knowledge with and without additional complications such as trapping potentials or disorder. However, the dynamical properties and excitations in particular of the SF phase in the vicinity of the quantum phase transition, are still not completely understood. A number of authors have addressed the dynamics of the Bose-Hubbard model in different dimensions, [46, 47, 48, 49, 50, 51, 52, 53, 54, 55, 56, 57] with results providing valuable information about the underlying physics, while corresponding work on coupled cavity models has just begun.[58, 59] The two most important dynamic observables are the dynamic structure factor and the single-particle spectral function, which are also at the heart of theoretical and experimental works on Bose fluids.[60] Experimentally, the dynamic structure factor may be measured by Bragg spectroscopy or lattice modulation (in cold atomic gases) as well as by neutron scattering (in liquid helium), and single-particle excitations of optical solid-state systems are accessible by means of photoluminescence measurements.

Whereas the standard Bose-Hubbard model only supports MI and SF phases, the physics of the polariton models is slightly richer. Owing to the composite nature of the conserved particles (polaritons), these phases can either be of polaritonic, excitonic or photonic character[58, 61, 62, 63] with distinct dynamic properties. Which of the cases is realized depends on the value of the detuning between the cavity mode and the transition frequency of the atoms that mediate polariton repulsion. Very recently it has been proposed that the fractional quantum Hall effect may also be realized in coupled cavity arrays.[64]

In general, accurate and unbiased results are very hard to obtain. Most existing work on spectral properties in the Mott phase is based on mean-field and/or strong-coupling approximations, in which fluctuations of the particle numbers are more or less restricted. Results of extensive strong coupling expansions for the phase diagram [65, 47] do, however, agree very well with precise density-matrix renormalization group (DMRG)[48] and quantum Monte Carlo (QMC) results.[55, 54] Bogoliubov type descriptions have been found to accurately describe the SF phase only in the limit of weak interaction, and fail to account for the transition to a MI and correlation features in the SF close to the transition. Hence the most interesting (and most difficult) regime is that near the quantum phase transition, where quantum fluctuations and correlation effects cannot be neglected.

In one dimension (1D), quantum fluctuation effects are particularly pronounced and mean-field methods are in general insufficient. Notable exceptions include situations where coupling to additional degrees of freedom provides an effective long-range interaction.[43] An interesting aspect of 1D is that for strong (repulsive) interaction, fermions and bosons behave in a very similar way, and that the low-energy, long-wavelength physics is described by the Luttinger liquid model.[66]

In the present paper we employ the directed loop quantum Monte Carlo method,[67] which is exact and therefore yields unbiased results also in difficult parameter regimes. Importantly, our simulations preserve the full quantum dynamics.

Few nonperturbative results are available for the spectra in the Bose-Hubbard model, namely for the dynamical conductivity,[48] for the dynamic structure factor $S(k,\omega)$[49, 50] on small systems, and for the single-boson spectral function $A(k,\omega)$ in the Mott phase deduced from small systems,[52] all in 1D. For the polariton model considered here, only $A(k,\omega)$ in the Mott phase has been calculated.[58]

The focus of our work is therefore on the calculation of excitation spectra for both the Bose-Hubbard model and the polariton model within and around the first Mott lobe (i.e., the lobe with density one), for which comparison to recent analytical and numerical results is made. Other issues addressed include the sound velocity in the SF phase, particle and hole masses, as well as temperature and detuning effects for the case of the polariton model.

Our simulations are performed at low but finite temperatures. On one hand, this complicates the analysis of the results, but on the other hand it matches the experimental situation.[60, 68]

The paper is organized as follows. In Sec. 4.3 we introduce the two models considered. Section 4.4 contains some details about the method. Results are discussed in Sec. 4.5, and in Sec. 4.6 we present our conclusions.

4.3 Models

The polariton model we consider is the simplest among several recent proposals.[33, 34, 35, 36, 5] It describes an array of L optical microcavities, each of which contains a single two-level atom with states $|\downarrow\rangle$, $|\uparrow\rangle$ separated by energy ε. Within the rotating wave approximation one such cavity is represented by the Jaynes-Cummings Hamiltonian[37] ($\hbar = 1$)

$$\begin{aligned}\hat{H}_i^{\mathrm{JC}} &= \varepsilon\,|\uparrow_i\rangle\langle\uparrow_i| + \omega_0 a_i^\dagger a_i \\ &\quad + g(|\uparrow_i\rangle\langle\downarrow_i|\,a_i + |\downarrow_i\rangle\langle\uparrow_i|\,a_i^\dagger)\,. \end{aligned} \tag{4.1}$$

Here ω_0 is the cavity photon energy, and $\Delta = \varepsilon - \omega_0$ defines the detuning. The atom-photon coupling g ($a_i^\dagger$, a_i are photon creation and annihilation operators) gives rise to formation of polaritons (combined atom-photon or exciton-photon excitations). Allowing for nearest-neighbor photon hopping between cavities with amplitude t leads to the lattice Hamiltonian

$$\hat{H}^{\mathrm{PM}} = -t\sum_{\langle i,j\rangle} a_i^\dagger a_j + \sum_i \hat{H}_i^{\mathrm{JC}} - \mu\hat{N}_{\mathrm{p}}\,. \tag{4.2}$$

The conserved polariton number $\hat{N}_{\mathrm{p}} = \sum_i \hat{n}_{\mathrm{p},i}$, with $\hat{n}_{\mathrm{p},i} = a_i^\dagger a_i + |\uparrow_i\rangle\langle\uparrow_i|$, is determined by the chemical potential μ.[69] Polaritons experience an effective repulsion $U_{\mathrm{eff}}(n_{\mathrm{p}})$ [see Eq. (4.11)] due to the nonlinear dependence of the single-site energy on the local

occupation number $n_{\rm p}$. We use g as the unit of energy and set ω_0/g, $k_{\rm B}$ and the lattice constant equal to unity. The rotating wave approximation becomes unjustified for g comparable to ε. The motivation for setting $g = \varepsilon$ is direct comparison to previous work. The Hamiltonian (4.2) has been studied in Ref. [33, 69, 35, 70, 58, 71, 5, 62, 61, 63, 59, 44].

We also consider the Bose-Hubbard Hamiltonian

$$\hat{H}^{\rm BHM} = -t \sum_{\langle i,j \rangle} b_i^\dagger b_j + \frac{U}{2} \sum_i n_i(n_i - 1) - \mu \hat{N} \,, \tag{4.3}$$

describing soft-core bosons with repulsion U and hopping t. Here $\hat{N} = \sum_i \hat{n}_i = \sum_i b_i^\dagger b_i$, is the total number of bosons, and we use U as the unit of energy.

As an alternative to the spin language used here, the polariton model (4.2) can be written as a two-band Bose-Hubbard Hamiltonian;[72] one boson species is itinerant, whereas the other is immobile (corresponding to localized excitons) with a hard-core constraint. This correspondence provides a direct connection to recent work on cold atomic gases in optical lattices, with the natural extension to the case where the excitons are mobile as well.[43]

We shall see below that owing to the composite nature of the bosonic particles in the polariton model, it is generally easier to understand the features of the Bose-Hubbard model first, and then explore similarities to the polariton model. Moreover, analytical approximations are more readily available for the Bose-Hubbard model and provide insight into the numerical data. Periodic boundary conditions in real space are applied in all simulations, and the system size is denoted as L.

4.4 Method

We use the directed loop method,[67] a generalization of the loop algorithm,[21, 73] which has no systematic errors and is efficient (low autocorrelations), facilitating the simulation of large systems at low temperatures. We make use of the ALPS library [74, 75] and of the ALPS applications,[76] which use the stochastic series expansion (SSE) representation[15] of worldline path integrals. We have verified that we obtain the correct phase boundary in 1D for selected points in parameter space.

In contrast to most previous QMC calculations of the Bose-Hubbard model, the focus of the current paper is on dynamical properties. The SSE representation has the drawback that dynamical correlation functions in imaginary time, which we need to obtain spectra, are very inefficient to calculate, since they involve a convolution of Green functions at different SSE distances.[19] On the other hand, Green functions can be measured easily in an imaginary time representation. For this reason we revert a mapping from continuous time to SSE[10] when measuring Green functions. To each operator in a given SSE operator string we associate a time $\tau \in [0, \beta]$ which is

stochastically sampled out of a uniform distribution. This maps the SSE configuration into a worldline configuration in continuous imaginary time.[77]

Correlation functions of diagonal operators can then be measured directly. For example, in the case of $\langle\hat{\rho}_i(\tau)\hat{\rho}_j(0)\rangle$ we evaluate the density $\rho_i(\tau)$ on a fine time grid. This time discretization limits the high energy range of the Green function, but does not introduce any discretization error to the QMC algorithm itself. With the Fourier transformation of the density $\mathcal{F}(\hat{\rho}_i(\tau)) = \hat{\rho}_{k,\omega}$, we measure the correlation function $\mathcal{F}(\langle\hat{\rho}_i(\tau)\hat{\rho}_j(0)\rangle) = \langle\hat{\rho}_{k,\omega}\hat{\rho}_{-k,\omega}\rangle$ using fast Fourier transforms.

The evaluation of off-diagonal single-particle correlation functions of the form $\langle\psi_i(\tau)\psi_0^\dagger(0)\rangle$ requires some care. We again make use of the worldline picture, in which two operators $\psi^\dagger$ and ψ are inserted whenever a new loop update starts. Let us assume that ψ moves around (loop head) while $\psi^\dagger$ is pinned (loop tail). The time and position of the loop tail are set as the new origin of our coordinate system, and we store the values $\langle\alpha|\psi_i(\tau)\psi_0^\dagger(0)|\beta\rangle$ whenever the loop head $\psi_i(\tau)$ crosses a point on the time grid with distance (i,τ) from the new origin. Here $|\alpha\rangle$, $|\beta\rangle$ are the states in the world line configuration prior to the arrival of the loop head. We then again use fast Fourier transformation to evaluate the correlation functions in Fourier space.

Let us now define the observables of interest. The quantum phase transition can be detected by calculating the superfluid density ρ_s, measured in the simulations in terms of the spatial winding number w as $\rho_\mathrm{s} = L\langle w^2\rangle/\beta$,[78, 79] $\beta = 1/kT$ being the inverse temperature. Another important observable in the context of the MI-SF transition is the total density, $n = \langle\hat{N}\rangle/L$ in the Bose-Hubbard model, and $n_\mathrm{p} = \langle\hat{N}_\mathrm{p}\rangle/L$ in the polariton model.

Concerning dynamical properties, we compute the dynamic structure factor $S(k,\omega)$ and the single-particle spectral function $A(k,\omega)$. The dynamic structure factor at momentum k and energy ω is given by

$$\begin{aligned} S(k,\omega) &= \frac{1}{2\pi L}\int_{-\infty}^{\infty} d\tau e^{\mathrm{i}\omega\tau}\,\langle\hat{\rho}_k(\tau)\hat{\rho}_k^\dagger(0)\rangle \\ &= \frac{1}{L}\sum_{n,m}\frac{e^{-\beta E_n}}{Z}\left|\langle m|\,\hat{\rho}_k^\dagger\,|n\rangle\right|^2\delta[\omega-(E_m-E_n)]\,, \end{aligned} \tag{4.4}$$

with the grand-canonical partition function Z and the energy of the nth eigenstate E_n. In our simulations, $S(k,\omega)$ is obtained from

$$\langle\hat{\rho}_k(\tau)\hat{\rho}_{-k}(0)\rangle = \int d\omega S(k,\omega)\frac{e^{-\tau\omega}}{1+e^{-\omega\beta}} \tag{4.5}$$

by means of the maximum entropy method.

For the Bose-Hubbard model, the density operator $\hat{\rho}_i = \hat{n}_i$, and $\rho_k^\dagger = \sum_q b_{q+k}^\dagger b_q$. For the polariton model, we can calculate the dynamic structure factor for photons

$[S^{\rm ph}(k,\omega)]$, atoms $[S^{\rm at}(k,\omega)]$ or polaritons $[S(k,\omega)]$ by using

$$\hat{\rho}_i = \begin{cases} a_i^\dagger a_i & \text{for photons}\,, \\ |\uparrow_i\rangle\langle\uparrow_i| & \text{for atoms}\,, \\ a_i^\dagger a_i + |\uparrow_i\rangle\langle\uparrow_i| & \text{for polaritons}\,, \end{cases} \tag{4.6}$$

respectively.

The single-particle spectral function is defined as

$$\begin{aligned} A(k,\omega) &= -\frac{1}{\pi}\mathrm{Im}\,\langle\langle\hat{\psi}_k;\hat{\psi}_k^\dagger\rangle\rangle_\omega \\ &= \sum_{n,m}\frac{e^{-\beta E_n}}{Z}\left|\langle m|\,\hat{\psi}_k^\dagger\,|n\rangle\right|^2\delta[\omega-(E_m-E_n)]\,, \end{aligned} \tag{4.7}$$

where the real-space operator $\hat{\psi}_i$ entering the Green function is given by $\hat{\psi}_i = b_i$ for the Bose-Hubbard model, and by $\hat{\psi}_i = a_i$ for the polariton model. maximum entropy is again used to map to real frequencies.

The QMC algorithm samples the partition function in the grand canonical ensemble. However, using only those configurations which have a given number of polaritons enables us to measure observables in the canonical ensemble as well. Here this simple but powerful trick permits us to study the fixed-density phase transition which occurs in the polariton model as a function of t/g.

The SSE representation requires to set a maximum boson number per site. In the Bose-Hubbard model, we allow a maximum of six bosons per site. In the polariton model we allow from six (Mott insulator, fixed-density transition) up to 16 (SF phase) photons per site. Convergence has been monitored by plotting histograms of the photon number distribution, and the cut-offs have been chosen generously such that there was no truncation error.

4.5 Results

We begin with a review of the properties of the Bose-Hubbard model and the polariton model as they emerge from previous work. Whereas a substantial literature exists for the Bose-Hubbard model, work on the polariton model began only recently, based on mean-field theory,[33, 44] exact diagonalization,[69] the DMRG,[70] the variational cluster approach,[58], QMC[80] and strong coupling theory.[59] Our discussion focuses on 1D, and follows Fisher *et al.* [38] and Kühner *et al.* [48]

The *Bose-Hubbard model* describes the competition of kinetic energy and local, repulsive interaction. Depending on the ratio t/U and the density of bosons n (the system is superfluid for any $t > 0$ if n is not integer), the Bose-Hubbard model at temperature $T = 0$ is either in a MI state or in a SF state. The MI is characterized by an

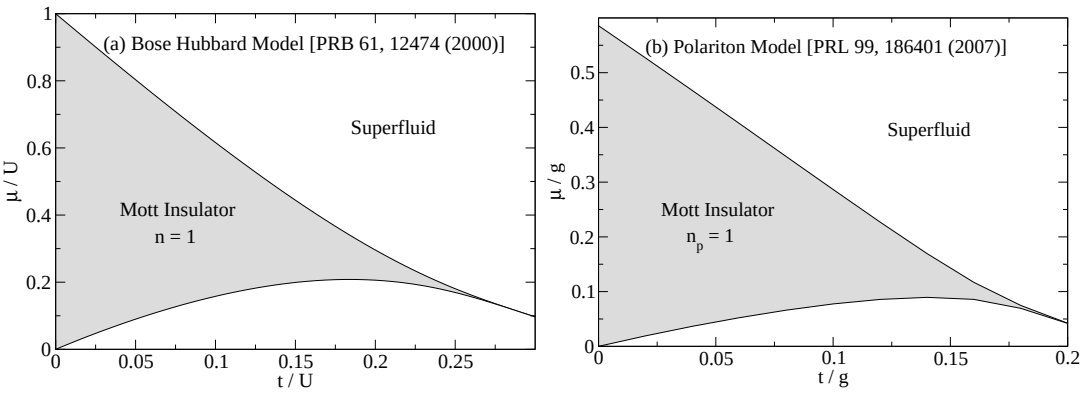

Figure 4.1: Zero-temperature phase diagram for (a) the Bose-Hubbard model and (b) the polariton model in 1D. We only show the Mott lobes with density one. These DMRG results were obtained by (a) Kühner *et al.* [48] and (b) Rossini *et al.* [70]

integer particle density, phase fluctuations and a gap in the single-particle excitation spectrum. In the SF phase, we have significant density fluctuations, phase coherence, and nonzero superfluid density ρ_s, as well as gapless (phonon) excitations with linear dispersion at small k.

For the case of one dimension considered here, a precise zero-temperature phase diagram in the $\mu/U, t/U$ plane has been determined by Kühner *et al.*,[48] and these data are shown in Fig. 4.1(a). There exists a Mott lobe inside which the density $n = 1$ (higher lobes with integer $n > 1$ are not shown), and which is surrounded by the SF phase.

There are two qualitatively different ways to make a transition from the MI to the SF.[38] The generic MI-SF transition is driven by addition or subtraction of small numbers of particles to the incompressible MI phase, the total energy cost for which is given by the distance in μ-direction from the nearest phase boundary. Since additional particles or holes (which Bose condense at $T = 0$) can move freely, the gain in kinetic energy can outweigh the interaction energy, leading to the MI-SF transition. Across the generic transition, which is mean-field like in character, the density varies continuously and the single-particle gap closes linearly as a function of the distance from the phase boundary, $E_g \propto \delta$, where $\delta = t - t_c$ or $\mu - \mu_c$ is the distance from the phase boundary.[38]

There also exists a MI-SF transition at fixed density, driven by the onset of boson hopping due to the increase of the ratio t/U, i.e. by quantum fluctuations. It has been shown that this transition occurs at the tip of the Mott lobe, and that it has a different universality class than the generic transition.[38] In d dimensions, the universality class is that of the $(d + 1)$ dimensional XY model, so that in 1D there is a Kosterlitz-Thouless phase transition at the multicritical point. For this case, the Mott gap $E_g \propto$ exp(-const/$\sqrt{t_c - t}$) closes exponentially (i.e., very slowly) as a function of the distance

from the lobe tip,[47] and strong deviations from the parabolic lobes predicted by mean-field theory[38] are observed in both strong-coupling[81, 65, 47] and DMRG results.[82] Another remarkable aspect of the 1D case is the occurrence of multiple MI-SF transitions along lines of constant chemical potential over an extended range of $\mu \lesssim 0.2$ [see Fig. 4.1(a)].[82, 48]

The *polariton model* also shows a series of Mott lobes, in which the polariton density n_p is pinned to an integer (see Fig. 4.1(b) for the phase boundaries of the $n_\mathrm{p} = 1$ lobe obtained by DMRG[70]). Even for pinned n_p the photon and exciton densities can fluctuate. Deep in the Mott phase and for $n_\mathrm{p} \geq 1$, we can approximate the ground state by a product over single sites, each of which is described by the Jaynes-Cummings eigenstates (see, e.g., Ref. [59])

$$\begin{aligned} |n_\mathrm{p}, -\rangle &= \cos\theta(n_\mathrm{p})\,|n_\mathrm{p}, \downarrow\rangle - \sin\theta(n_\mathrm{p})\,|n_\mathrm{p}-1, \uparrow\rangle \ , \\ |n_\mathrm{p}, +\rangle &= \sin\theta(n_\mathrm{p})\,|n_\mathrm{p}, \downarrow\rangle + \cos\theta(n_\mathrm{p})\,|n_\mathrm{p}-1, \uparrow\rangle \ , \end{aligned} \tag{4.8}$$

where $\tan\theta(n_\mathrm{p}) = 2g\sqrt{n_\mathrm{p}}/[2\chi(n_\mathrm{p}) - \Delta]$, $\chi(n_\mathrm{p}) = \sqrt{g^2 n_\mathrm{p} + \Delta^2/4}$, and with eigenvalues $E^{\pm}(n_\mathrm{p}) = -(\mu - \omega_0)n_\mathrm{p} + \Delta/2 \pm \chi(n_\mathrm{p})$. Hence for fixed polariton number n_p, the ground state $|n_\mathrm{p}, -\rangle$ is a coherent superposition of two states which differ by the state of the atom (or spin) as well as the number of photons; this hybridization provides the connection to exciton polaritons.

The extent of the lobes in both the μ and t directions diminishes quickly with increasing n_p due to the reduced polariton-polariton repulsion $U_\mathrm{eff}(n_\mathrm{p})$; the $t = 0$ vertical width of the lobes in the Bose-Hubbard model is always U. At large values $\zeta t > \omega - \mu$ (ζ being the coordination number), beyond those considered in the present work, the polariton model shows an instability.[44]

In this work we restrict our discussion to the region in the phase diagram in or close to the Mott lobes with density $n_\mathrm{p} = 1$ or $n = 1$. This lobe is the largest in the polariton model with zero detuning, and quantum effects are most pronounced. A density of one is also the most interesting case for experimental realizations.[33, 58]

All the discussion so far has been for $T = 0$. Both experiments and our simulations are carried out at low but finite temperatures, with several important consequences. Strictly speaking, there is no true MI at $T > 0$ due to thermal excitations. However, there exist quasi-MI regions which have finite but very small compressibility (see also the discussion of temperature effects later). As long as the density remains close to an integer, these regions may be regarded as Mott insulating. Corresponding "phase diagrams" at finite T have been obtained for both the polariton and the Bose-Hubbard model.[83, 58, 56] Except for our analysis of temperature effects in Sec. 4.5, the simulations have been carried out at values of $\beta = 3L$, large enough to ensure that we have an (almost) integer density in the Mott phase.

The Bose-Hubbard model in more than one dimension (and most likely the polariton model as well) exhibits a phase transition from a SF to a normal state (gapless with

no phase coherence), related to the well-known λ transition in liquid helium, at a temperature T_λ.[54, 55] This gives rise to an intervening normal region in the phase diagram, between the MI (at small t/U) and the SF (at large t/U).[83] In the 1D case considered here we have $T_\lambda = 0$, so that for any $T \neq 0$ only quasi-MI and normal states exist in the thermodynamic limit. However, when the temperature is so low that the SF correlation length in the thermodynamic limit far exceeds the system size L, results will be representative of the SF state. Making use of finite size and finite temperature effects, a scaling analysis in fact yields accurate results for the $T = 0$ phase boundaries.[84, 80] Remarkably, interacting 1D bosons can be realized using cold atomic gases (the Tonks-Girardeau gas)[85, 86] and are described by the Bose-Hubbard model at low but finite temperatures.[66]

Similar to Bose fluids, the low-energy excitations in the SF phase are phonons. Within Bogoliubov theory,[87] these quasiparticles are described by a creation operator $\psi_k^\dagger = \mathsf{u}_k b_k^\dagger + \mathsf{v}_k b_{-k}$, and they have been observed experimentally in ultracold atom systems.[88] As some of our results can be understood in terms of Bogoliubov theory, let us state some key results for the Bose-Hubbard model. The coefficients of the coherent superpositions of particle and hole excitations are given by[89]

$$\begin{aligned} |\mathsf{u}_k|^2 =& \frac{K(k) + n_0 U + \omega_k}{2\omega_k}\,, \\ |\mathsf{v}_k|^2 =& \frac{K(k) + n_0 U - \omega_k}{2\omega_k} = |\mathsf{u}_k|^2 - 1\,, \end{aligned} \tag{4.9}$$

with excitation energy

$$\begin{aligned} \omega_k &= \sqrt{K(k)(2n_0 U + K(k))}\,, \\ K(k) &= 4t \sin^2(k/2)\,. \end{aligned} \tag{4.10}$$

Here n_0 is the condensate fraction, equal to $n_0 = (\mu + t)/U$ in the simple Bogoliubov approach at $T = 0$.[57] For small $k \approx 0$, we have a linear dispersion $\omega_k \approx \pm\sqrt{2n_0 tU}k$, and both $|\mathsf{u}_k|$ and $|\mathsf{v}_k|$ are nonzero. For large $k \approx \pi$, the energy dispersion is $\pm(-ck^2 + 2\sqrt{4t^2 + 2n_0 Ut})$ and thus free particle like. If we assume $t \gg U$, which is the parameter region where Bogoliubov theory is valid, then $|\mathsf{u}_k|^2 \approx 1$ and $|\mathsf{v}_k|^2 \approx 0$ for $k \gg 0$, i.e. only one excitation branch is populated at large momenta. This also holds true for the parameters studied numerically in this work. We further compare to the higher order approximation proposed in Ref. [89]. For the Bose-Hubbard model, the latter yields the same equations for $|\mathsf{u}_k|^2$, $|\mathsf{v}_k|^2$ and ω_k, but n_0 is determined self-consistently, allowing for depletion effects.

In the case of free bosons at $T = 0$, all particles condense in the same $k = 0$ state. However, finite temperature and/or interactions cause a certain fraction of these particles to occupy states of higher energy. Indeed, both for $U \to 0$ (noninteracting bosons) and $n_0 \to 0$ (high temperature limit) we have $|\mathsf{u}_k|^2 = 1$, $|\mathsf{v}_k|^2 = 0$. Moreover,

with decreasing U or n_0, $|\mathsf{v}_k|^2$ approaches zero most quickly at large k since in this case $K(k) \gg n_0 U$ so that $\omega_k \approx K(k)$, canceling the term $-\omega_k$ in the expression for $|\mathsf{v}_k|^2$. This will explain the temperature evolution of the single-particle spectrum shown in Sec. 4.5.

4.5.1 Bose-Hubbard model

Despite the extensive literature on this model, there are few nonperturbative results available for the spectra, as mentioned in Sec. 4.2. Therefore, we investigate the single-boson spectral function $A(k,\omega)$ and the dynamic structure factor $S(k,\omega)$, with results shown in Figs. 4.2 and 4.4.

4.5.1.1 Single-particle spectrum

Menotti and Trivedi reviewed previous work on the single-particle spectrum, and presented results from a random phase approximation.[57] Their main findings are as follows. For large t/U, a weakly interacting SF exists, and the spectrum consists of the usual two gapless phonon modes which exhaust the sum rule for $A(k,\omega)$. Reducing t/U, two additional gapped modes appear at small k whose spectral weight increases upon approaching the quantum phase transition. At the transition, one of the phonon modes evolves into the particle or hole mode (depending on which of the gaps $E_{\mathrm{g,p}}$, $E_{\mathrm{g,h}}$ is smaller), whereas one of the gapped modes in the SF becomes a gapped mode in the MI. Menotti and Trivedi[57] argued that the appearance of gapped modes and the redistribution of spectral weight from coherent phonon modes to incoherent gapped modes indicate the strongly correlated nature of the SF state near the transition. Let us point out that particle and hole dispersions in the MI have been calculated by several authors before, [57, 47, 56, 90, 91, 53, 46, 51, 92, 52] whereas the full spectral function of the MI (which also reveals the spectral weight and the width of the excitations) was only shown in Ref. [52, 57].

Our numerical results for the single-particle spectral function $A(k,\omega)$ are shown in Fig. 4.2. The four different values of the ratio t/U cover the range in which the generic MI-SF transition takes place. According to Fig. 4.1(a), for the chosen value of $\mu/U = 0.5$ the transition occurs at $t/U \approx 0.14$. In each panel we also report the total density n to three decimal places, although our simulations provide much higher accuracy. The MI [(a) and (b)] exhibits the familiar gapped particle and hole bands.[47] The additional particles exhibit a free-particle dispersion since the energy penalty for double occupation is the same at every site. In particular, we see in Fig. 4.2(a), (b) that the particle band width is $8t$ (the factor of two arising from the fact that particle hopping involves a doubly occupied site), whereas the hole bandwidth is $4t$. The Mott gap decreases with increasing t and a symmetry of particle and hole bands emerges.[38, 58, 54] In addition to our QMC results we plot the mean-field

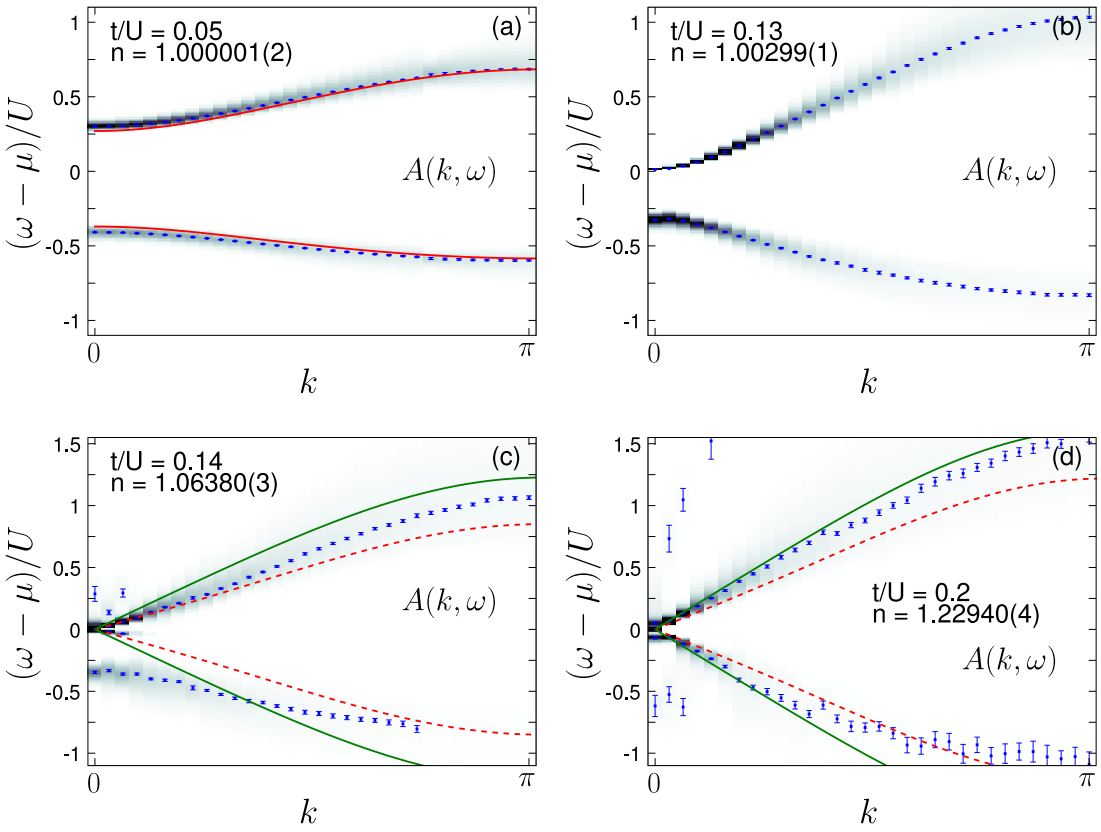

Figure 4.2: (color online) Single-boson spectral function $A(k,\omega)$ of the 1D Bose-Hubbard model, for different hoppings t (and total density n), corresponding to (a) the MI phase, (b) just below the MI-SF transition, (c) just above the transition, and (d) the SF phase. Here $\mu/U = 0.5$, $L = 64$ and $\beta U = 3L$. Here and in subsequent spectra, the symbols and errorbars indicate the maxima of the peaks and the associated errors obtained by the maximum entropy method. As discussed in Sec. 4.5.1.2, features with very small spectral weight are difficult to determine accurately. The solid red lines in (a) are mean field results.[90] The solid lines in (c) and (d) are the Bogoliubov results, while the dashed lines are a fourth order approximation (see text).[89]

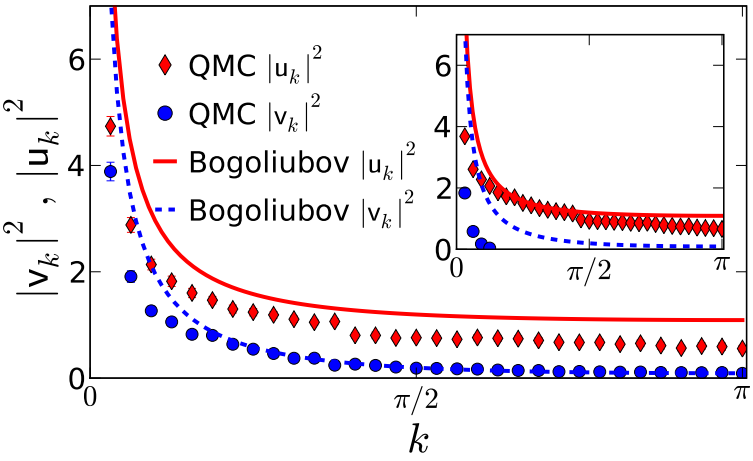

Figure 4.3: (color online) Quasiparticle weights u_k and v_k of the gapless modes at $t/U = 0.2$. The symbols are integrated intensities from QMC and maximum entropy, the lines are the predictions from Bogoliubov-theory. The inset shows data at $t/U = 0.14$. Again, $\mu = 0.5$, $L = 64$ and $\beta = 3L$.

dispersion [90] in Fig. 4.2(a). For larger $t/U = 0.13$, mean-field theory already predicts a superfluid, although the critical hopping in 1D is $t_c/U \approx 0.14$.

In the SF phase [Fig. 4.2(c),(d)], we obtain the expected Goldstone modes with linear dispersion at small k. Additionally, we see two gapped signals which we relate to the gapped modes discussed by other authors.[51, 53, 57] Whereas the negative-energy gapped mode is clearly visible in Fig. 4.2(c) just above t_c, the gapped modes have almost disappeared in Fig. 4.2(d). Since we approach the phase transition above the lobe tip ($\mu/U = 0.5$) the particle band becomes the gapless mode and carries more spectral weight, while the gapped hole band evolves into a gapped mode in the SF. This agrees well with the findings of Menotti and Trivedi.[57] In accordance with Bogoliubov theory, the excitations in the SF phase are free-particle like for large k. The bandwidths of the excitations both in the MI and the SF phase scale roughly linearly with t.

In Figs. 4.2(c) and (d) we also show results for the phonon dispersion $\pm\omega_k$ (without taking into account the weights $|u_k|$, $|v_k|$) from Bogoliubov theory as well as the higher-order approximation of Ref. [89]. Whereas the simple Bogoliubov approach (neglecting depletion of the condensate) agrees quite well with our data despite the rather small value of t/U, we do not find the higher order approach to be systematically better. In particular, at large k, the phonon bandwidth is noticeably underestimated, which may be a result of an overestimate of depletion effects (these are most visible at large k). The agreement with Bogoliubov theory at small k coincides with the findings of Menotti and Trivedi.[57] Rey *et al.* [89] found the higher order approximation to be consistent with numerical results for other observables but do not show the spectra seen

in Fig. 4.2. Note that these authors consider larger particle densities $n \geq 5$ where the Bogoliubov-type approximations are more reliable. Finally, we tried to use our QMC results for the superfluid fraction for n_0 in the expressions obtained from Bogoliubov theory, but the results are worse than for $n_0 = n$.

The spectral weight of the excitations decreases with increasing k in all spectra of Fig. 4.2, although this is more pronounced in the SF phase than in the MI. In Fig. 4.3 we show the quasiparticle weights of the massless modes in the SF phase, obtained by integrating over the quasiparticles peaks in the spectra, and compare them to Bogoliubov theory (Eqs. 4.9 and 4.10). We verified that the QMC spectra satisfy the sum rule. The spectral weight of the lower branch decreases more quickly, consistent with the Bogoliubov picture. However, Bogoliubov theory overestimates the quasiparticle weights, especially at small k. Besides, there is a significant broadening of the peaks on approaching the zone boundary. At strong coupling close to the phase transition (inset of Fig. 4.3), the quasiparticle weight of the lower branch decays much more quickly than Bogoliubov theory would predict.

Sound velocity. The sound velocity $v_s = \frac{\partial \omega_k}{\partial k}|_{k\to 0}$ of the phonon excitations in the SF phase was calculated for the Bose-Hubbard model by Menotti and Trivedi using a random phase approximation.[57] They concluded that v_s vanishes at the generic transition, but remains nonzero when crossing the multicritical point.[57, 53] In their results, there is a very sharp downturn of v_s toward zero close to t_c. We are not aware of any calculations of v_s for the polariton model.

From our QMC simulations, we can determine v_s from linear fits to the spectrum. Apart from the limited accuracy of the maximum entropy inversion, this works quite well away from t_c. In agreement with Bogoliubov theory, we find for the Bose-Hubbard model a linear dependence $v_s \propto |t - t_c|$ and good agreement of results for $L = 32$ and 64.

Determining the behavior of v_s as $t \to t_c$ is more difficult for two reasons. First, the phonon spectrum becomes nonlinear due to finite-temperature effects (see discussion below), rendering linear fits ill-defined. Second, the position of the phase transition changes with system size, so that no reliable finite-size scaling of v_s can be carried out. The situation is similar for the polariton model, and we therefore do not show results for v_s here, leaving this as an interesting issue for future work.

4.5.1.2 Dynamic structure factor

The single-particle spectral function provides information about the energy and lifetime of particles or holes added to the interacting ground state. In contrast, the dynamic structure factor—corresponding to the imaginary part of the dressed particle-hole propagator—yields insight into the density fluctuations in the ground state. In general the two quantities do not exhibit the same features. However, for broken U(1) gauge symmetry in the SF phase, they are both dominated by the same single-particle

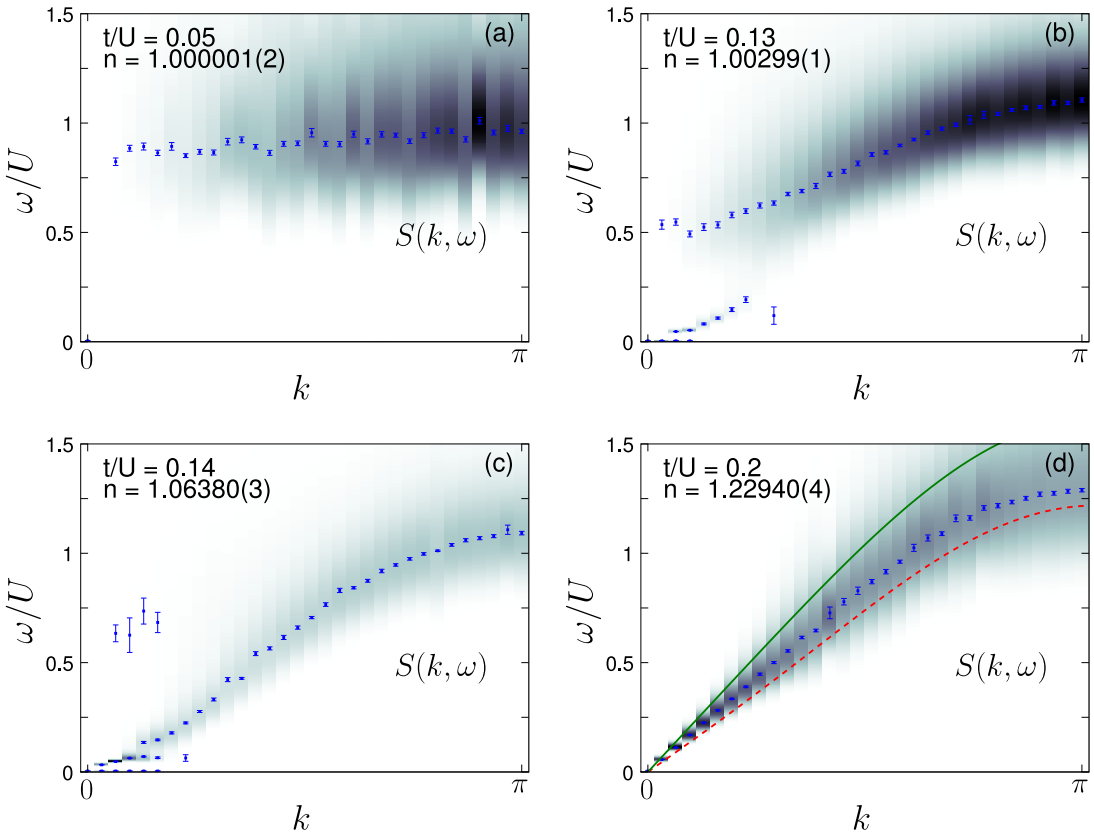

Figure 4.4: (color online) Dynamic structure factor $S(k,\omega)$ of the Bose-Hubbard model for the same parameters as in Fig. 4.2. Panel (d) includes the same analytical approximations as Fig. 4.2(d).

excitations (phonons).[60] We find this statement to hold in 1D even though no symmetry breaking occurs.

The density operator in the Bose-Hubbard model is $\rho_k^\dagger = \sum_l e^{-ikl}\hat{n}_l$. For $k = 0$, we have $\rho_k^\dagger = \sum_l \hat{n}_l$, and $S(k,\omega)$ has a trivial contribution at $\omega = 0$ which we dismiss by considering $\widetilde{\rho}_k^\dagger = \sum_l e^{-ikl}(\hat{n}_l - \langle\hat{n}_l\rangle)$. The above-mentioned relation to particle-hole excitations becomes evident by rewriting the density operator as $\rho_k^\dagger = \sum_q b_{q+k}^\dagger b_q$.

We show results for $S(k,\omega)$ in Fig. 4.4. According to Huber *et al.*,[53] $S(k,\omega)$ in the MI phase should exhibit a continuum of particle-hole excitations, starting at $\omega = E_\mathrm{g}$ due to the Mott gap in the single-particle spectrum (see Fig. 4.2). For the parameters in Fig. 4.4(a), $E_\mathrm{g}/U \approx 0.7$. The dispersion of the particle and hole bands is very weak, Note that we find no agreement with the two single-particle excitations $E_\mathrm{g}^\mathrm{p} + \varepsilon_\mathrm{h}(k)$, $E_\mathrm{g}^\mathrm{h} + \varepsilon_\mathrm{p}(k)$ discussed by Huber *et al.* This may be a result of their mean-field treatment of the two-dimensional case. Our results do agree qualitatively with exact numerical results on small clusters.[49]

For larger t/U, the Mott state contains nontrivial density fluctuations, and the upper band in $S(k,\omega)$ acquires some k dependence. The energy of the excitations in $S(k,\omega)$ [following $\sum_q\{\varepsilon_\mathrm{h}(q) + \varepsilon_\mathrm{p}(k-q)\}$] [53] generally increases with increasing k. This is obvious from the momentum dependence of the particle and hole bands in $A(k,\omega)$, and also agrees with the expectation that long-wavelength density fluctuations in a Mott state require less energy than fluctuations with short periods in real space.

For $t \lesssim t_\mathrm{c}$ in Fig. 4.4(b), we find a low-energy mode with nonlinear dispersion, which we interpret as a precursor of the linear excitations of the SF phase [see panel (d)]. Even for $t \gtrsim t_\mathrm{c}$ [Fig. 4.4(c)], the gapless low-energy mode in our numerical results is not linear. A linear spectrum is a result of the condensation of bosons in the SF phase, but is not expected in the normal phase. Since our simulations are done at finite temperature, and because the phase coherence length is small close to t_c, we can understand the absence of a clear, linear signature in Fig. 4.4(c). Going to larger t_c, we indeed see linear excitations near $k = 0$ [Fig. 4.4(d)]. Similar effects are expected for the single-particle excitations, but are difficult to see on the scale of Fig. 4.2. Coming back to Fig. 4.4(c), away from $k = 0$, we find a free-particle like contribution, similar to the case of the MI. This excitation carries negligible spectral weight near $k = 0$.

Apart from finite-temperature effects, these features are qualitatively similar to the excitations discussed by Huber *et al.*,[53] namely a gapless sound mode (related to phase and density modulations) dominant at small k, and a massive mode (corresponding to exchange between condensate and noncondensate at fixed density) acquiring spectral weight at $k > 0$. Additionally, we see in Fig. 4.4(c) the (weak) signature of a gapped mode at small k, the nature of which we cannot determine from our present simulations. For $t/U = 0.2$ [Fig. 4.4(d)] the excitation "band" in $S(k,\omega)$ follows closely the Bogoliubov mode, in accordance with the discussion at the beginning of this section.

At this point, a comment concerning the accuracy of the spectra obtained from the maximum entropy inversion is in order. The spectral weight of the features visible in density plots such as Fig. 4.4(d) varies over orders of magnitude. Some very weak signals, such as the group of points located at around $k = \pi/2$ below the main excitation band (with a weight that is a factor 10000 smaller than that of the dominant features), are expected to be artifacts. We shall see below that in the polariton model, there actually exist real excitations with very small spectral weight which are easy to miss in the maximum entropy inversion. To reliably study such excitations, analytical approaches (if available) are clearly superior.[59]

Our findings for the dynamic structure factor are consistent with previous numerical results on small systems ($L = 10, 20$).[50, 49] We can confirm the broadening of the excitations with increasing k in the SF phase,[50] related to two-particle continua.[53] However, the maximum entropy method is not capable of resolving fine structures as (generically) seen in exact diagonalization results for small clusters.[49]

4.5.2 Polariton model

For the polariton model, the only published results on dynamic properties are for the single-particle spectrum of the MI phase at zero temperature.[58, 59] As pointed out before, the nature of the conserved particles in the polariton model is determined by the detuning. We start by discussing the case $\Delta = 0$ for which the polaritonic character of the excitations is most pronounced. This can readily be seen from Eq. (4.8), where $|n_\mathrm{p}, \downarrow\rangle$ and $|n_\mathrm{p} - 1, \uparrow\rangle$ contribute with equal weight.

4.5.2.1 Single-particle spectrum

In Fig. 4.5 we show our QMC results for the single-photon spectral function. As for the Bose-Hubbard model, the values of the ratio t/g range from deep in the Mott phase across the generic transition well into the SF phase. According to a finite size scaling analysis for $\mu/g = 0.4$, the phase transition occurs at $t_\mathrm{c}/g = 0.0626(1)$ (see Fig. 4.14), in agreement with Fig. 4.1(b). Hence panels (a) and (b) are for the MI regime, whereas (c) and (d) are for the SF phase.

The results in the MI shown in Fig. 4.5(a), (b) agree well with previous numerical work.[58] Similar to the Bose-Hubbard model, there exist particle and hole bands, separated by the Mott gap. It is important to stress that although we add bare photons to the system, the particle and hole excitations reflect the properties of the polaritons in the system. Whereas the ratio of particle and hole bandwidths is two to one in the Bose-Hubbard model, it depends on the character of the quasiparticles (polaritons) in the polariton model and varies with detuning.[58] With increasing t/g, the gap closes and the bandwidths of excitations increase (effective masses decrease).

Recent analytical work revealed the existence of so-called upper polariton modes at

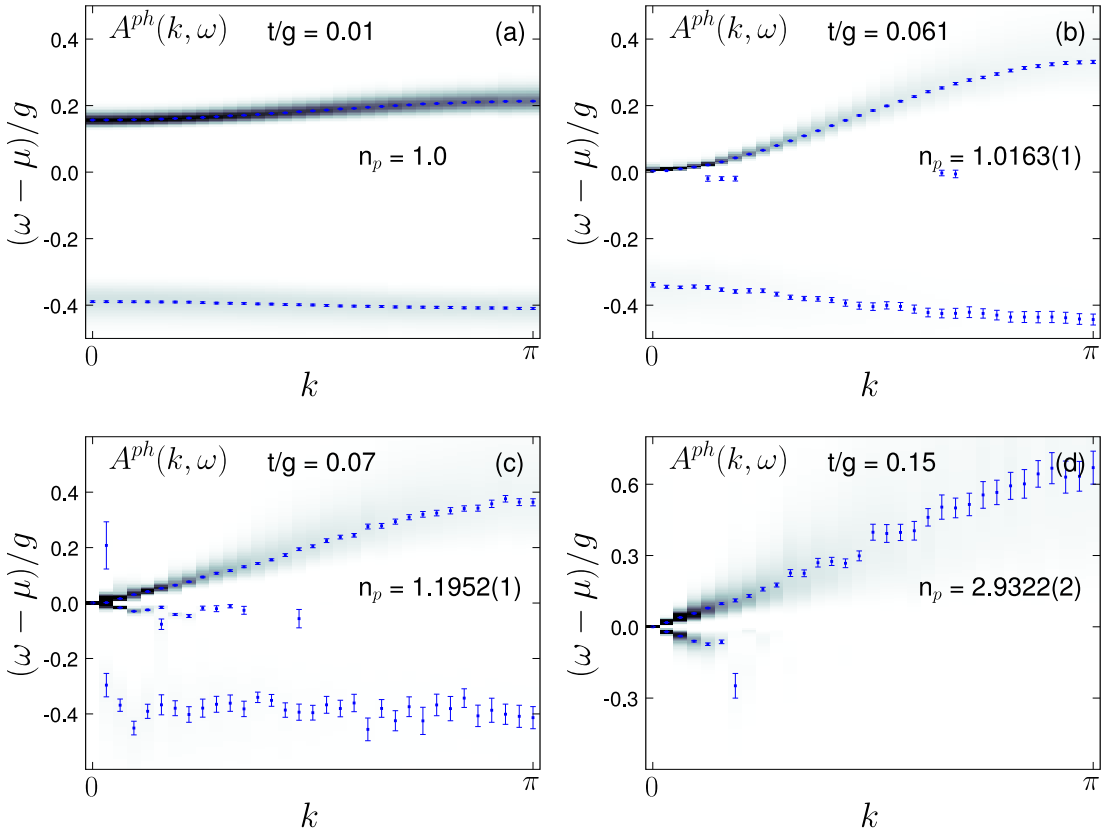

Figure 4.5: Single-photon spectral function $A^{\mathrm{ph}}(k,\omega)$ of the 1D polariton model at $\mu/g = 0.4$ for different hoppings t, corresponding to (a) deep in the MI, (b) just below the MI-SF transition, (c) just above the transition, and (d) in the SF phase. Here $\beta g = 3L$ and $L = 64$. With increasing t, the density plots are more and more "overexposed" to see less dominant features.

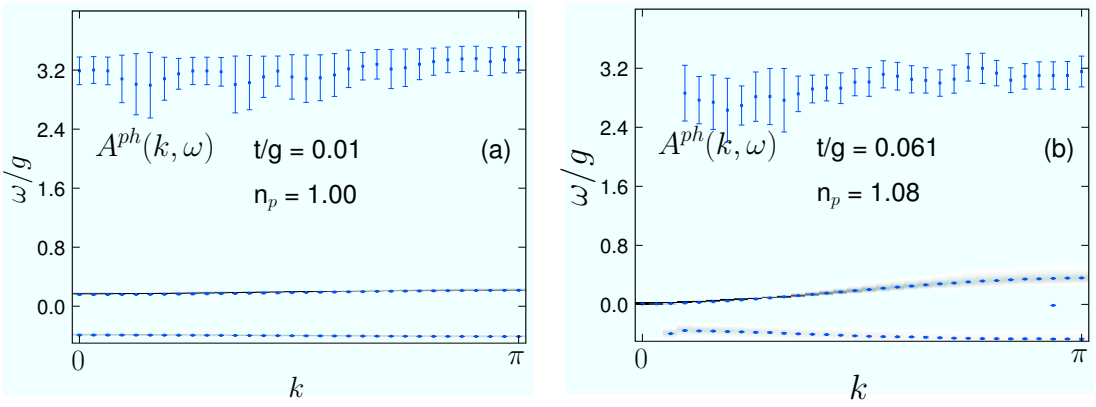

Figure 4.6: Single-photon spectral function in the Mott phase for the same parameters as in Fig. 4.5, showing additional excitations at higher energies.

higher energies, which represent an important difference between the Bose-Hubbard model and the polariton model.[59] For the Mott lobe with $n_\mathrm{p} = 1$, only one such (particle) band exists, corresponding (for small enough t/g) to a transition between the ground state $|n_\mathrm{p} = 1, -\rangle$ and the state $|n_\mathrm{p} = 2, +\rangle$ (see Eq. (4.8)). The weight of this high-energy excitation is very small compared to the dominant particle and hole modes discussed above (0.04 as compared to 1.46 for the $k = 0$ atomic-limit results in Ref. [59]); with increasing t/g the weight difference becomes even larger.[59] The energy splitting between the $-$ and $+$ branches of eigenstates increases further for detuning $\Delta \neq 0$ (Fig. 2 in Ref. [33]).

The upper polariton mode is not visible in Figs. 4.5(a) or (b). Excitations with small spectral weight are notoriously difficult to see using QMC in combination with maximum entropy. In the present case, this is aggravated by the fact that the resolution of maximum entropy decreases at high energy. Nevertheless, we see a signature of the upper polariton band in Fig. 4.6, and the latter is also present (but not shown) in the high-temperature data of Fig. 4.12(a); high-energy features are easier to resolve in QMC/maximum entropy at higher temperatures. From the eigenvalues of the states (4.8) we can determine the excitation energy of the upper mode in the atomic limit as $w_p^+/g = -(\mu - \omega_0)/g + (\sqrt{2}+1) \approx 3$ for the parameters of Fig. 4.6, in reasonable agreement with our results in Fig. 4.6(a) given the ill-conditioned nature of the problem under consideration. Note that the upper polariton mode can be seen even close to the phase transition in Fig. 4.6(b). The weight of the upper mode in Fig. 4.6 is about a factor of 100 smaller than that of the conventional particle and hole excitations. Although the upper polariton mode exists also in other results for the single-particle spectrum in the Mott phase (Figs. 4.8, 4.12 and 4.13), we focus on the low-energy conventional modes with large spectral weight. The latter can be determined accurately

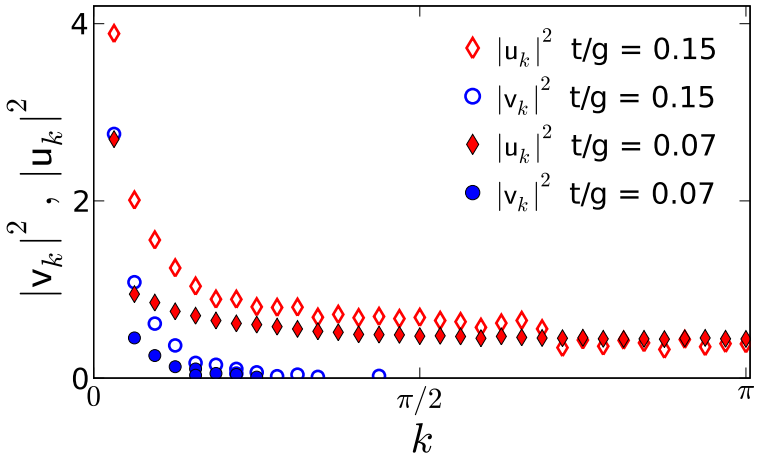

Figure 4.7: (color online) Quasiparticle weights u_k and v_k of the gapless modes of the polariton model, similar to Fig. 4.3.

from our simulations, and will be the dominant feature in experiments.

Figures 4.5(c) and (d) contain the first spectra of the polariton model in the SF phase. There is a clear signature of the gapless phonon modes starting at $k = \omega = 0$, with linear dispersion at small k. In the SF phase but close to the transition, we see an additional gapped mode at $\omega < 0$ [Fig. 4.5(c)]. Our results at these and at further couplings t/g (and t/U) suggest that these gapped modes disappear more quickly with increasing t/g than for the Bose-Hubbard model, which can be explained in terms of the photonic SF expected for the present parameters (see below).[63] Note that a simple Bogoliubov type theory for the polariton model does not exist, due to the composite nature of polariton excitations.

Figure 4.7 shows the quasiparticle weights. The general shapes resemble the Bose-Hubbard model case (Fig. 4.3), but the lower branch decays very quickly in the polariton model even at $t/g = 0.15$ quite far from the phase transition. This may be attributed to the fact that the energy cost for particle and hole excitations is different due to the dependence of U_{eff} on n_{p}. Again, most of the spectral weight in the SF phase is found at small k.

Fixed density. In Fig. 4.8 we show the single-photon spectrum across the fixed density transition ($n_{\text{p}} = 1$), obtained by selecting configurations only at that density. In Ref. [71], the critical hopping was determined as $t_{\text{c}}/g = 0.198$ [cf Fig. 4.1(b)]. The spectra in both the MI and the SF look very similar to those across the generic transition shown above. This may be different very close to the multicritical point, but this regime is most demanding numerically if the results are to be used in a maximum entropy inversion.

From the spectra obtained at constant density in the MI, we can estimate the effective

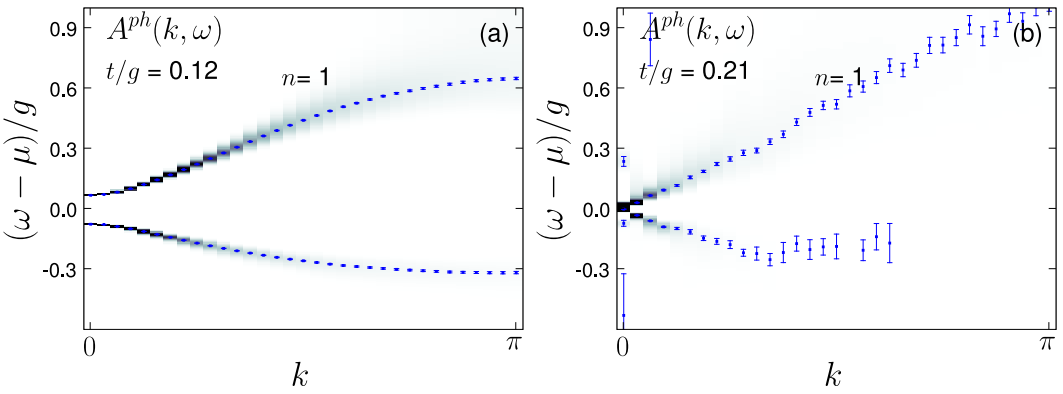

Figure 4.8: Single-photon spectrum $A^{\rm ph}(k,\omega)$ of the polariton model along the line $n_{\rm p}=1$ crossing the Kosterlitz-Thouless transition. Here $L=64$ and $\beta g=3L$.

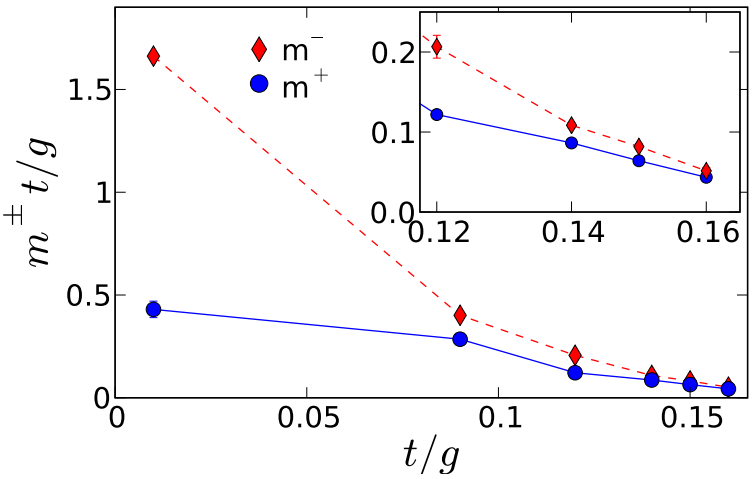

Figure 4.9: (color online) Effective particle (m^+) and hole masses (m^-) along the line $n_{\rm p}=1$, as obtained from fits to the bands in $A^{\rm ph}(k,\omega)$ near $k=0$.

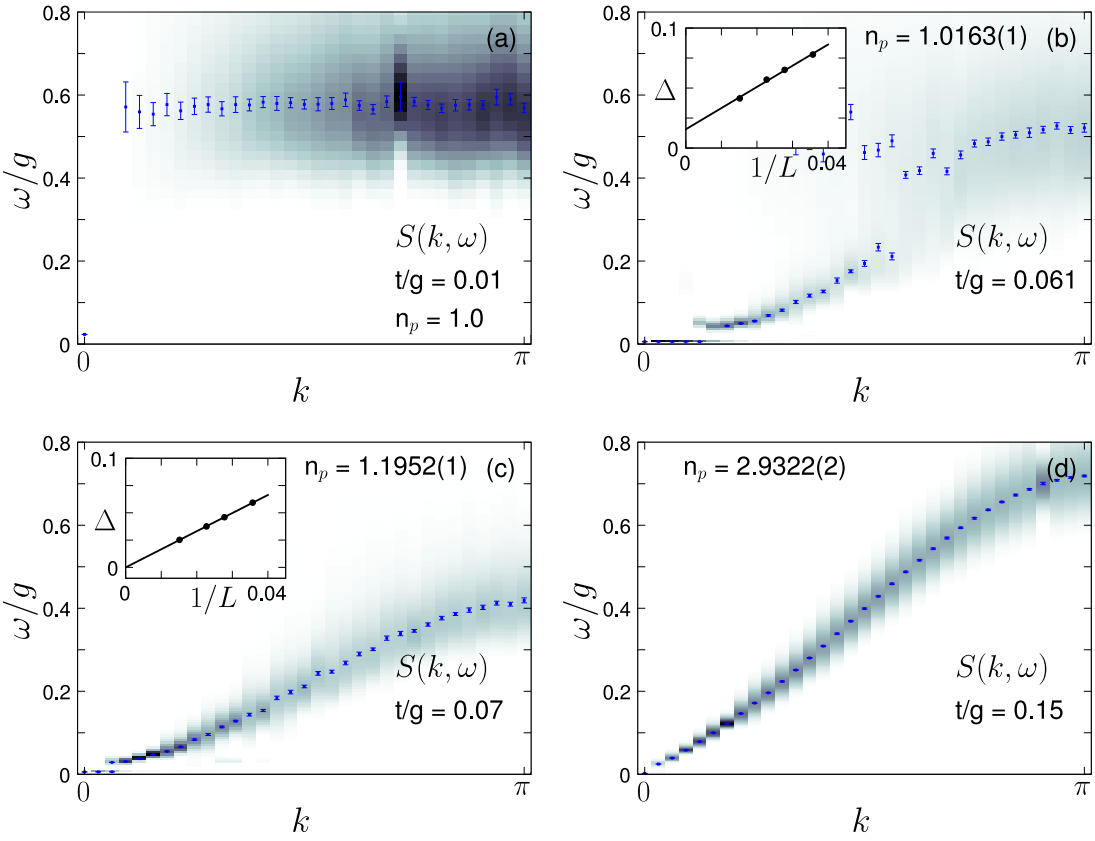

Figure 4.10: Polariton dynamic structure factor $S(k,\omega)$ for the same parameters as in Fig. 4.5. The insets show an extrapolation of the Mott gap at small k to $L \to \infty$.

particle and hole masses by fitting a quadratic dispersion to the bands in the vicinity of $k = 0$. In the Bose-Hubbard model, there is an emergent particle-hole symmetry on approaching the lobe tip,[38, 54] and similar behavior is suggested by the evolution of the particle and hole bands with increasing t/g also in the polariton model. For fixed polariton density, the two masses approach each other and vanish at the phase transition. This has been demonstrated in 2D based on a strong-coupling approach.[59] In the region not too close to the phase transition, where stable fits can be obtained, Fig. 4.9 confirms this observation also in 1D.

4.5.2.2 Dynamic structure factor

The evolution of the polariton dynamic structure factor $S(k,\omega)$ across the MI-SF transition is shown in Fig. 4.10. Remarkably, the results look very similar to those for

the Bose-Hubbard model. Close to the atomic limit [$t/g = 0.01$ in Fig. 4.10(a)] we see a gapped, almost flat feature with energy $\omega \approx 0.6g$. A look at the corresponding single-particle spectrum in Fig. 4.8(a) reveals that this value is identical to the Mott gap. The almost flat particle and hole bands cause a very weak dispersion also for the particle-hole excitations visible in $S(k, \omega)$. It is useful to remember that it is the effective polariton-polariton repulsion mediated by the atom-photon coupling that determines the Mott gap. For a single site and $n_\mathrm{p} = 1$ (i.e., for the case of adding a second polariton),

$$U_\mathrm{eff}(1) = 2\sqrt{g^2 + (\Delta/2)^2} - \sqrt{2g^2 + (\Delta/2)^2} - \Delta/2\,. \tag{4.11}$$

For zero detuning ($\Delta = 0$), $U_\mathrm{eff}(1)/g = 2 - \sqrt{2} \approx 0.59$.

As for the Bose-Hubbard model, the excitations in $S(k, \omega)$ acquire a noticeable dispersion with increasing t/g, and the $k = 0$ gap closes. Figures 4.10(b) and (c) are both close to the phase transition. An inspection of the $k = 0$ region shows a weak linear mode with very small slope $O(0.01)$, corresponding to the small superfluid density existing in both $L = 64$ systems. The massive mode extends to $k = 0$ with a tiny intensity (thus not visible in the figure). An extrapolation of the gap to $L = \infty$ (insets) shows that it scales to zero in Fig. 4.10(c), but stays finite at the smaller hopping in Fig. 4.10(b). Indeed, a finite size scaling of the superfluid density (discussed later) implies that Fig. 4.10(b) is just below the phase transition. In addition to finite size effects, we again observe finite temperature effects in the form of deviations from the expected linear spectrum close to t_c (see discussion for the Bose-Hubbard model). For even larger t/g, the spectrum exhibits a single linear mode at small k. Similar to the spectral function, gapped modes seem to be suppressed quickly in the SF phase.

Clearly, the polariton dynamic structure factor $S(k, \omega)$ represents a useful probe to distinguish between the MI and the SF phases. We have argued before that the polariton MI has fluctuations in the photon and exciton density, whereas the polariton density is pinned.

We now demonstrate that the exciton (atom) and photon structure factors, $S^\mathrm{at}(k, \omega)$ and $S^\mathrm{ph}(k, \omega)$, shown in Fig. 4.11, do not reflect this fact, and therefore cannot be used to characterize the nature of the Mott state. To this end, it is important to notice that the Jaynes-Cummings Hamiltonian has two branches of eigenstates $|n_\mathrm{p}, +\rangle$ and $|n_\mathrm{p}, -\rangle$ (the latter containing the ground state, see also Eq. (4.8)) with the same polariton number but different energy.[37] In the atomic limit, the dynamic structure factor for photons and excitons [Eq. (4.5)] is dominated by the contributions $\langle n_\mathrm{p}, -|\, \hat{\rho}_k^\dagger \,|n_\mathrm{p}, -\rangle$ (with $\omega = 0$) and $\langle n_\mathrm{p}, +|\, \hat{\rho}_k^\dagger \,|n_\mathrm{p}, -\rangle$ (with energy $\omega = 2\sqrt{ng^2 + \Delta^2/4}$, equal to 2 in Fig. 4.11). Any additional peaks at finite t/g have much smaller spectral weight and cannot be accurately resolved by our method. However, since the matrix elements of exciton and photon density operators for the combination $\langle n_\mathrm{p}, +|\, \hat{\rho}_k^\dagger \,|n_\mathrm{p}, -\rangle$ have the same modulus but opposite sign, the dominant contributions to $S^\mathrm{at}(k, \omega)$ and

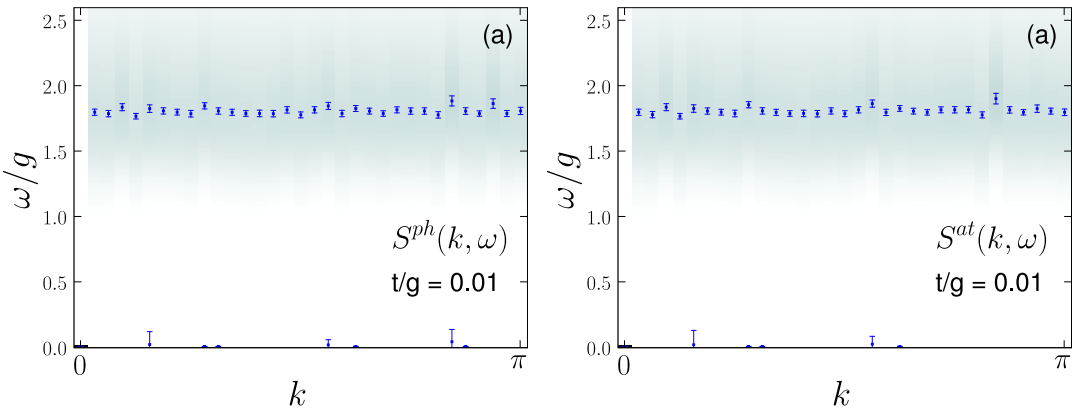

Figure 4.11: Dynamic structure factor for excitons (S^{at}) and photons (S^{ph}) for the same parameters as Fig. 4.10(a).

$S^{\mathrm{ph}}(k,\omega)$ cancel in the case of the polariton structure factor $S(k,\omega)$. The dispersionless excitations near $\omega/g = 2$ seen in Fig. 4.11 are therefore absent in $S(k,\omega)$, as confirmed by our data. Hence, while the upper polariton modes in the single-particle spectrum have small but finite weight, here their contribution is zero. Consequently, the polariton dynamic structure factor closely resembles $S(k,\omega)$ of the Bose-Hubbard model.

4.5.2.3 Temperature effects

Experimental realizations of Bose-Hubbard models using cold atomic gases are usually prepared very close to zero temperature (nK range). In contrast, due to the strong matter-light coupling achievable in cavities, realizations of polariton models offer a chance of operation at significantly higher temperatures. The critical temperature at which the MI state starts to lose its characteristic integer density has been estimated for the polariton model as $T^*/g \approx 0.03$.[58, 69] For feasible values of the coupling g, T^* falls into the mK range. Generally, Mott-like physics is expected as long as the Mott gap is significantly larger than the thermal energy (and the number of particle-hole excitations is small). The finite-temperature physics of the Bose-Hubbard model has been analyzed by several groups.[83, 93, 94, 91] Here we consider the effect of low but finite temperatures on the excitation spectra of the polariton model. This also provides information about the sensitivity of the results to the (necessarily finite) value of β used in our simulations.

The present method permits calculation of spectra also outside the MI, i.e., in the SF and the normal phase. We have pointed out above that, strictly speaking, there is no SF phase at $T \neq 0$ in 1D. Nevertheless, SF like properties can be seen for T sufficiently small. The results in Fig. 4.12 underline the discussion of finite-temperature effects on the dispersion in the SF near $k = 0$. The particle excitation is obviously not linear in

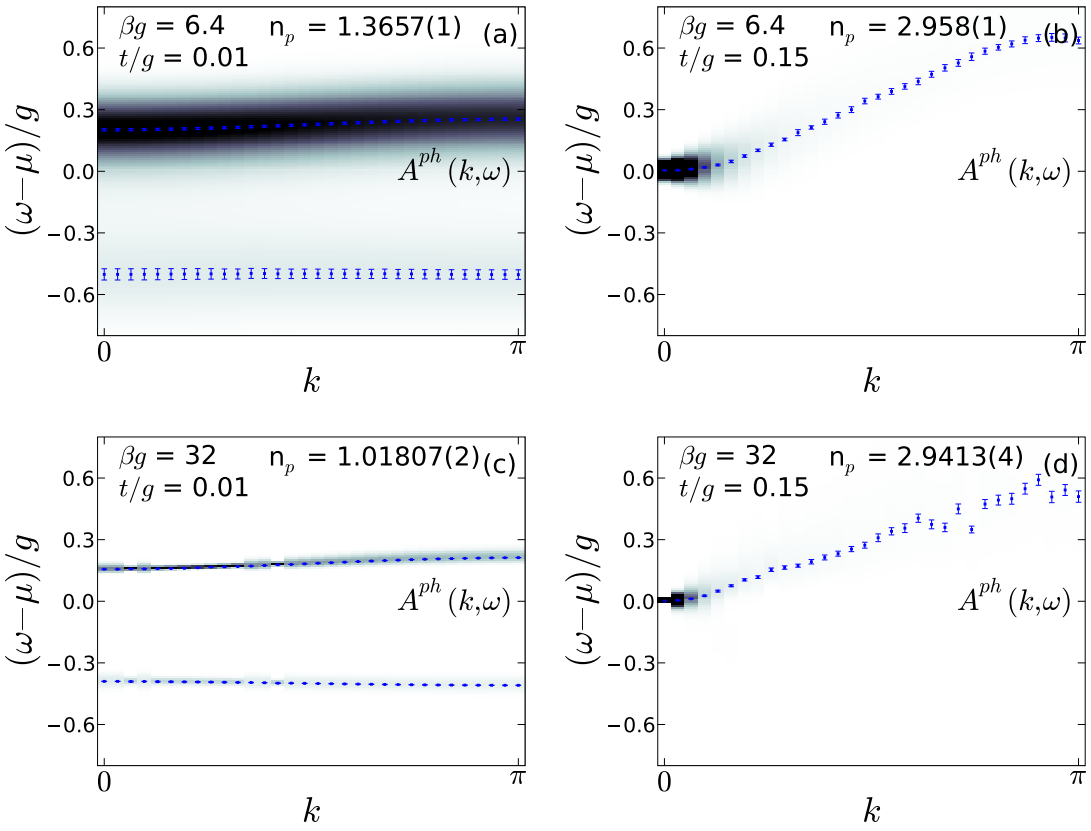

Figure 4.12: Temperature dependence of $A^{\mathrm{ph}}(k,\omega)$ in the polariton model at $\mu/g = 0.4$, in the MI (left) and in the SF phase (right). Here again $L = 64$. Corresponding results at $\beta g = 192$ can be found in Figs. 4.5(a),(d).

panels (b) and (d), for which the temperature is higher than in Fig. 4.5.

Results for $A^{\mathrm{ph}}(k,\omega)$ are shown in Fig. 4.12. At finite but low temperature [Fig. 4.12(c,d)] they still closely resemble the results at $T \approx 0$ in Figs. 4.5(a) and (d). At high temperature [Fig. 4.12(a,b)], we observe strong broadening of the particle band at all k, and strongly suppressed spectral weight for hole excitations. Existing work for the Bose-Hubbard model finds that at finite temperature additional multi-particle and hole bands arise.[93] We see an additional excitation for $\beta g = 4.4$ and $t/g = 0.01$ at an energy of $\omega/g \sim 3.1$. The weight of that excitation is about 50 times smaller than the weight of the main peak with energy $\omega/g \sim 0.2$ and thus not shown in Fig. 4.12 (a). This excitation is consistent with the upper polariton mode discussed above.

We note that a broadened "gapped" spectrum is compatible with a density that deviates from the integer value characteristic of the MI, and this has to be kept in mind for potential applications relying on integer density. The numerical results for the total density are shown in each of the panels, demonstrating that despite the large particle-hole gap the polariton density deviates significantly from the low-temperature value $n_{\mathrm{p}} = 1$ for the parameters of Fig. 4.12(a).

Some of the features observed in the SF phase can be explained by means of Bogoliubov theory for the Bose-Hubbard model. In particular, we have discussed above that with increasing temperature (where the condensate fraction $n_0 \to 0$) the spectral weight of the negative energy branch vanishes first at large k, in agreement with our numerical results. In addition the broadened positive energy branch no longer has a clear linear behavior at small k.

We would like to point out that not only finite temperature but also disorder is an inevitable feature of experimental realizations of coupled cavity systems. Although not studied here directly, it has been stated[69] that the effect of disorder (in the form of local variations of the parameters ω_0, g and t) has similar consequences as finite temperature.

4.5.2.4 Detuning

The detuning between the cavity photon mode and the atomic level splitting is an important parameter in the polariton model which is absent in the Bose-Hubbard model. Its influence on the physics has been discussed before.[58, 61, 80] Detuning can also be easily changed experimentally, motivating a calculation of the excitation spectra for $\Delta \neq 0$. Our results are shown in Fig. 4.13.

The extent of the different phases, namely excitonic or polaritonic MI and photonic or polaritonic SF in the phase diagram has been analyzed for a two-site system.[61] The way to distinguish between the polaritonic SF and the photonic SF is to monitor fluctuations in the exciton occupation number (pinned in the photonic SF but fluctuating in the polaritonic SF). The conclusion has been that for $t \approx |\Delta|$ a polaritonic SF exists only for $\Delta/g < -1$ This would match with the conjectured photonic nature of

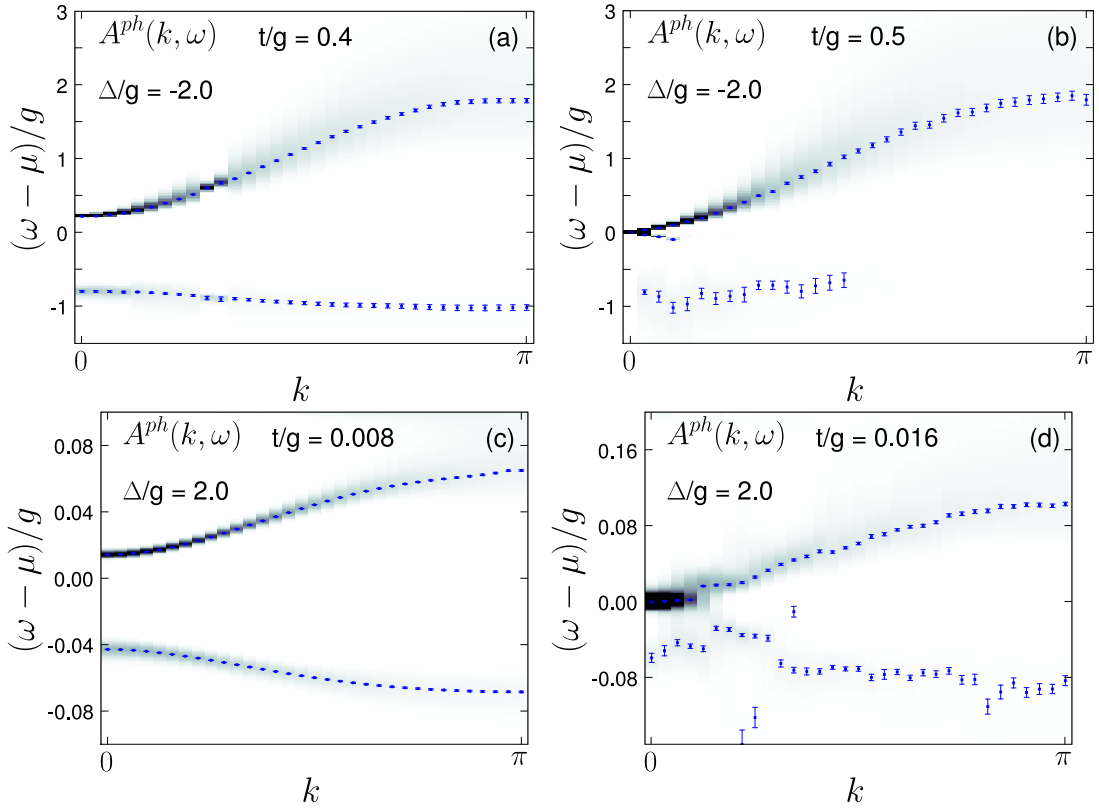

Figure 4.13: Single-photon spectra with detuning $\Delta = \varepsilon - \omega_0$ for the excitonic case $\Delta/g = -2$, $\mu/g = -0.5$ (a,b) and photonic case $\Delta/g = 2$, $\mu/g = 0.64$ (c,d), in the MI (a,b) and in the SF (c,d). Here $L = 64$ and $\beta g = 3L$.

the SF near the lobe tip in two dimensions.[80] However, it is not clear if these strict values also hold for larger systems and the thermodynamic limit. Besides, the work by Irish *et al.* [61] is exclusively concerned with the fixed density transition occurring at $t \approx |\Delta|$, whereas a polariton SF may exist also for $t < |\Delta|$ if density fluctuations are allowed (generic transition). The spectrum in Fig. 4.13(b) is for such a set of parameters.

Again pertaining to the fixed density case, the MI state is supposed to be of excitonic nature for $\Delta/g < -1$, $t < |\Delta|$, and of polaritonic nature for $|\Delta|/g < 1$ and small enough t/g respectively $t/|\Delta|$.[61] The former case is depicted in Fig. 4.13(a), whereas the latter corresponds to the $\Delta = 0$ results reported in Fig. 4.5.

For $\Delta \gg g$, photon excitations are always lower in energy, and the effective interaction approaches zero. As a result, MI regions are very small or nonexistent, and the photonic SF state is similar to that of the Bose-Hubbard model in the limit of large t/U.[58]

Here we consider $\Delta/g = \pm 2$ for comparison to previous calculations of the spectra in the Mott phase.[58] (Note that the rotating wave approximation formally requires $|\Delta| \ll \varepsilon, \omega_0$.[95]) These correspond to effective repulsions $U_{\text{eff}}/g = 0.096$ (for $\Delta/g = 2$) respectively $U_{\text{eff}}/g = 2.096$ (for $\Delta/g = -2$), in excellent agreement with the width of the $n_{\text{p}} = 1$ Mott lobes for the same parameters.[58]

Our results in Fig. 4.13 show that again the spectra are dominated by the generic features of the MI and the SF. However, the detuning in the present case changes the ratio of the bandwidths of particle and hole bands $W_{\text{p}}/W_{\text{h}}$ in the Mott state.[58] While for $\Delta = 0$, $W_{\text{p}}/W_{\text{h}} \approx 3$, we find $W_{\text{p}}/W_{\text{h}} \approx 2$ (similar to the result for the Bose-Hubbard model) for $\Delta/g = 2$ and $W_{\text{p}}/W_{\text{h}} \approx 7$ for $\Delta/g = -2$. The incoherent features observed for $\Delta/g = -2$ in Ref. [58] are not seen here. As mentioned before, the energy of the upper polariton modes (not shown) increases for $\Delta \neq 0$.[33]

In the SF, we find the expected gapless excitations, as well as gapped modes indicative of a correlated superfluid. Since for $\Delta/g = 2$, U_{eff} is very small, the Mott gap of the dispersive bands in Fig. 4.13(c) is also small ($0.057g$), but it is still larger than the temperature scale in our simulation $T/g = 0.005$. We note that, within our resolution, the positive energy spectrum in Fig. 4.13(d) looks gapless, but not clearly linear. In this respect, the spectra for finite detuning resemble those obtained at high temperatures. Apart from this issue and a scaling of energies (due to the dependence of U_{eff} on Δ), the spectra obtained for $\Delta/g = -2$ are very similar to those for $\Delta = 0$, whereas those for $\Delta/g = 2$ resemble closely the results for the Bose-Hubbard model.

4.5.2.5 Phase transition

To end with, we present a scaling analysis for the generic phase transition. As pointed out by Fisher *et al.* [38] the scaling relation

$$\rho_{\text{s}} = L^{2-d-z} \widetilde{\rho}(\delta L^{1/\nu}, \beta/L^z) \tag{4.12}$$

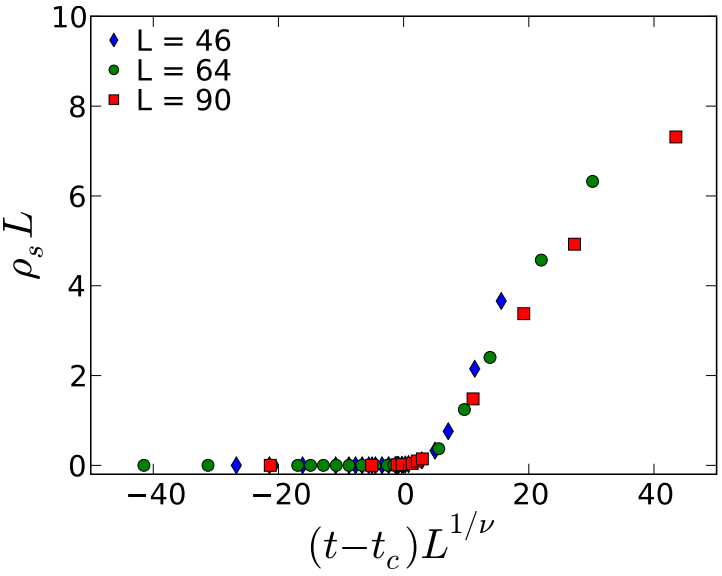

Figure 4.14: (color online) Finite size scaling for the generic transition in the polariton model at $\mu/g = 0.4$, testing the scaling hypothesis Eq. (4.12).

should hold for the superfluid density across the MI-SF transition. Here ν is the critical exponent of the correlation length which is expected to diverge like $\xi \sim \delta^{-\nu}$, and z is the dynamical critical exponent. The generic transition in the Bose-Hubbard model has mean-field exponents $z = 2$ and $v = 1/z = 1/2$.[38, 96, 84, 55] Recent field theory[44] and strong-coupling results[59] predict the same universality classes for the polariton model, in conflict with numerical results in two dimensions which suggest the absence of multicritical points.[80]

We test in 1D the scaling hypothesis Eq. (4.12) with $z = 2$ and the hyperscaling relation $z = 1/\nu$, along the line $\mu/g = 0.4$ where the generic transition is expected [see Fig. 4.1(b)].

To this end we keep the temperature constant at $\beta = L^2/10$ and plot $\rho_s L^{d+z-2}$ over $(t - t_c)L^{1/\nu}$ to obtain the universal function $\widetilde{\rho}$ (Fig. 4.14). Defining a cost function in the spirit of Ref. [97], allows us to evaluate the quality of the finite-size-scaling plot quantitatively.

We find the minimum of our cost function at $t_c = 0.0626(1)$ and $\nu = 0.50(2)$ when matching $\widetilde{\rho}$ close to the phase transition [$|(t - t_c)L^{1/\nu}| < 1$ in Fig. 4.14]. We note that with the system sizes available, this result is not very stable. A fit in a larger region of $|(t - t_c)L^{1/\nu}|$ provides a better data collapse overall (but worse close to the phase transition), with $\nu \approx 0.65$ and very slightly smaller t_c.

A similar scaling with $z = 1$ did not succeed, so that we conclude that the universality class of the generic transition in the polariton model is the same as that in the Bose-

Hubbard model, despite the composite nature of the quasiparticles. This is consistent with recent field-theory and strong-coupling results.[44, 59]

An accurate scaling analysis for the fixed density transition through the lobe tip has been found to require much larger system sizes and is therefore not shown. In the 1D case considered, the shape of the lowest Mott lobe in 1D (see Fig. 4.1) suggests that the similarity to the Bose-Hubbard model holds also in this respect, i.e. a Kosterlitz-Thouless type phase transition.

4.6 Conclusions

We calculated the single-boson spectral function and the dynamic structure factor of the Bose-Hubbard model, and for a recently proposed model of itinerant polaritons in coupled-cavity arrays. These models undergo a quantum phase transition from a Mott insulator to a superfluid state upon increasing the hopping integral of the bosons respectively photons with respect to the interaction. Results in one dimension, within and close to the Mott lobe with density one, have been obtained.

Despite the generally different nature of the conserved particles, the models exhibit very similar spectral properties, including gapped particle and hole bands in the Mott insulating phase, and Bogoliubov type excitations in the superfluid phase. Additional excitations related to the second branch of upper polariton states exist in the single-particle spectrum of the polariton model,[59] but cancel out in the dynamic structure factor. In general, these features have high energy and very small spectral weight, so that for practical purposes the excitation spectra are qualitatively similar to the Bose-Hubbard model.

Correlation effects are particularly strong in the one dimensional case considered. Our results in the superfluid phase represent the first unbiased nonperturbative spectra for $A(k,\omega)$ in both models and for $S(k,\omega)$ in the polariton model (in both phases). Good qualitative agreement with recent analytical work on the two-dimensional Bose-Hubbard model was found, and we have compared our results in the superfluid phase to Bogoliubov theory. The limiting cases of the Mott insulator close to the atomic limit, as well as the weakly interacting superfluid are described quite well by analytical approximations, whereas in the phase transition region, our nonperturbative results show considerable deviation. Emerging particle-hole symmetry on approach of the multicritical lobe tip has been demonstrated for the polariton model.

For the polariton model, we have also explored the influence of detuning and finite temperature on the spectral properties, and have presented a scaling analysis to determine the universality class of the generic phase transition. Keeping in mind experimental realizations of coupled cavity arrays, interesting open issues for future work include the excitation spectra in the two-dimensional case (and comparison to analytical results[59]), the behavior of the sound velocity across the phase transition (also for

the Bose-Hubbard model) and disorder.

The present work further highlights the fact that the physics of strongly correlated bosons as described by the Bose-Hubbard model may be observed in terms of optical models that, if realized, would have some distinct experimental advantages and further contain new degrees of freedom due to the mixed nature of the quasiparticles.

4.7 Acknowledgments

MH was supported by the FWF Schrödinger Fellowship No. J2583. PP acknowledges support from the FWF, projects P18551 and P18505. We made use of the ALPS library[74, 75] and the ALPS applications.[76] We acknowledge fruitful discussions with F. Assaad, M. J. Bhaseen, J. Keeling, D. Khmelnitskii and P. B. Littlewood. We are grateful to H. Monien and D. Rossini for providing us with data for Figure 4.1.

5 Momentum resolved and temperature dependent spectra of the two-dimensional Bose–Hubbard model

Momentum resolved and temperature dependent spectra of the two-dimensional Bose–Hubbard model

Peter Pippan, Michael Knap, and Hans Gerd Evertz
Institute of Theoretical and Computational Physics, TU Graz, 8010 Graz, AUT
(Dated: October 18, 2010)

In addition to the zero temperature phase transition from a superfluid phase to a Mott insulating phase, the two dimensional Bose-Hubbard model exhibits a superfluid to normal fluid phase transition at finite temperature. We perform precise quantum Monte-Carlo calculations to investigate the spectral signatures associated with these two transitions and compare our results whenever it is possible to analytical and alternative numerical calculations. In particular, we evaluate the single-particle spectral function and the dynamic structure factor. Both of them exhibit a gapped spectrum in the Mott phase. The gap vanishes when increasing the temperature. In superfluid phase we obtain linear and gapless Goldstone modes. For increasing temperature the excitation at positive energy develops a quadratic behavior whereas the mode with negative energy vanishes. Our results provide crucial information for Bragg spectroscopy experiments with ultracold atoms trapped in optical lattices, where it became only recently possible to measure wave vector resolved spectral excitations. Our numerical results might proof useful for interpreting the experimental data and for characterizing the measured phases.

PACS numbers: 67.25.dj,64.70.Tg,42.50.Ct,03.75.Kk

This chapter is identical to the draft of a paper which is about to be submitted.

5.1 Abstract

In addition to the zero temperature phase transition from a superfluid phase to a Mott insulating phase, the two dimensional Bose-Hubbard model exhibits a superfluid to normal fluid phase transition at finite temperature (see Fig. 5.1). We perform precise quantum Monte-Carlo calculations to investigate the spectral signatures associated with these two transitions and compare our results whenever it is possible to analytical and alternative numerical calculations. In particular, we evaluate the single-particle spectral function and the dynamic structure factor. Both of them exhibit a gapped spectrum in the Mott phase. The gap vanishes when increasing the temperature. In superfluid phase we obtain linear and gapless Goldstone modes. For increasing temperature the excitation at positive energy develops a quadratic behavior whereas the mode with negative energy vanishes. Our results provide crucial information for

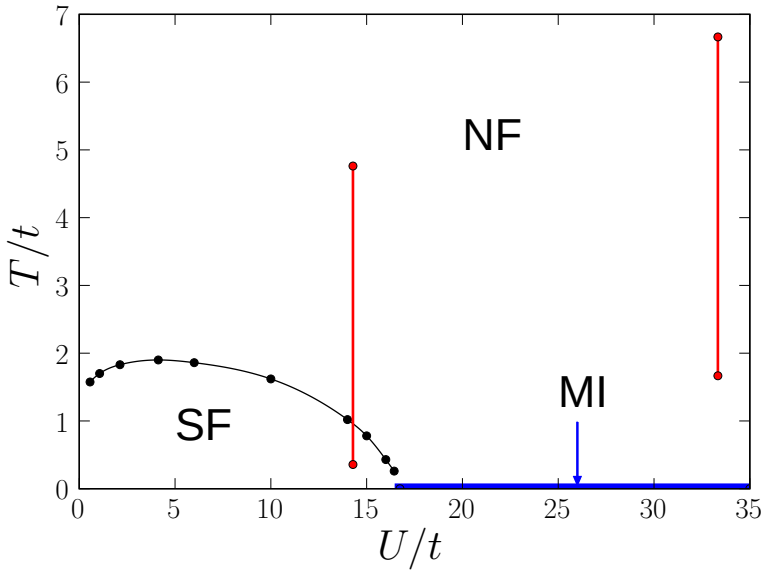

Figure 5.1: Finite temperature phase diagramm from Ref. [54]. This is for $n = 1$, i.e. along the KT phase transition line at T=0. SF stands for superfluid, NF for normal fluid, and MI for Mott insulator. The black line is a guide to the eye. The red lines mark the parameter regions, in which we perform most of the calculations.

Bragg spectroscopy experiments with ultracold atoms trapped in optical lattices, where it became only recently possible to measure wave vector resolved spectral excitations. Our numerical results might proof useful for interpreting the experimental data and for characterizing the measured phases.

5.2 Introduction

Bose-Einstein condensates (BECs) mounted in optical lattices, which are formed by interfering laser beams, allow to study the strongly correlated regime of interacting bosons.[28, 2] As opposed to strongly correlated condensed matter systems the parameters of BECs in optical lattices can be tuned easily. That has been used for instance to demonstrate the Mott insulator to superfluid phase transition experimentally.[1]

In recent experiments it was furthermore possible to study excitations in these systems, making also quantum dynamics directly accessible. [30, 3, 31, 4] In these experiments Bragg spectroscopy has been applied to study basic excitations. Inelastic scattering of photons allows to perturb the atoms with well defined momentum and frequency. The high momentum and frequency resolution of this method makes a spectroscopic measurement of the excitations possible, which in turn allows to extract the spectral properties of BECs trapped in optical lattices.[4]

These systems can be modeled with the Bose–Hubbard Hamiltonian [28]

$$\hat{H} = -t \sum_{\langle i,j \rangle} \hat{a}_i^\dagger \hat{a}_j + \frac{U}{2} \sum_i \hat{n}_i(\hat{n}_i - 1) - \mu \sum_i \hat{n}_i, \tag{5.1}$$

where $\hat{a}_i^\dagger$ and are bosonic creation and annihilation operators on lattice site i, respectively , t is the hopping amplitude, U the on-site interaction energy and μ determines the average number of particles.

Already in the seminal paper on the Bose–Hubbard model, [38] it has been shown that the model undergoes a phase transition from a Mott insulating phase to a superfluid. Since then an extensive amount of work has been done to study this model. Exemplary we want to mention that the phase diagram has been calculated very accurately in one, two, and three dimensions. [54, 48, 47, 55] Spectral properties, containing the one-particle spectral function and sometimes the dynamic structure factor as well, of the two dimensional model have been investigated using various methods, including mean field and random phase approximation (RPA) approaches, [98, 99, 100, 53] strong coupling theory, [51] high order series expansion, [47] and the variational cluster approach [101] Apart from that the oneparticle spectral function has been studied in the one dimensional model using RPA variational cluster approach, [52, 102] The dynamical structure factor has been investigated in Refs. [49, 103, 50, 6]

In this paper we calculate the dynamical properties of the Bose–Hubbard model in two dimensions using unbiased QMC simulations. In particular we evaluate the oneparticle spectral function and the dynamical structure factor at various temperatures and parameter configrations. With that we are able to unveil the phase transition from Mott to superfluid phase and superfluid to normal fluid phase directly form the spectral properties. Although some work has already been done to investigate the spectral properties of the two-dimensional BH model, a comprehensive study containing both phase transitions is still missing. As QMC is an exact simulation technique with controllable errors our results can be used as well to check whether alternative numerical and analytical calculations, which suffer from (sometimes uncontrollable) approximations, lead to the right results also on the qualitative level. To this end we compare our results, whenever it is possible, to alternative existing calculations. Finally, since in experiments a heating of the BEC occurs due to the lattice field, it remains important to know, whether normal fluid signatures are measured rather than true superfluid ones. Our results on the spectral properties will provide estimates about the necessary accuracy of Bragg spectroscopy experiments to distinguish these two phases.

This paper is organized as follows. In Sec. 5.3 we specify the QMC algorithm used to evaluate the dynamic properties of the Bose–Hubbard model. In addition, we state the inverse problem which has to be solved in order to extract the one-particle spectral function and the dynamic structure factor from the corresponding imaginary time

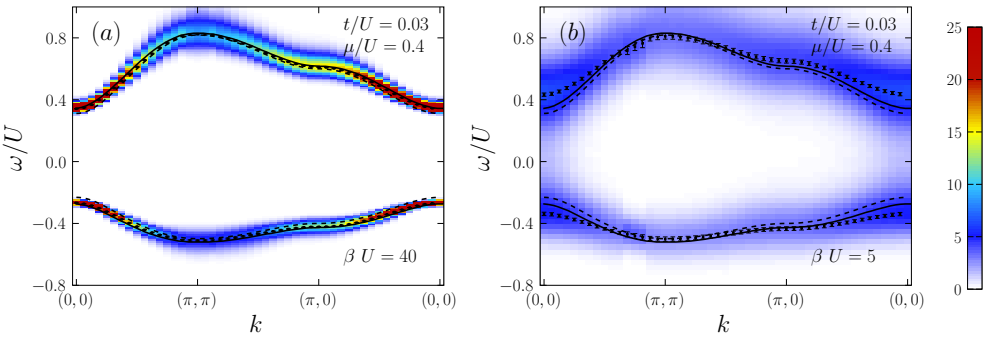

Figure 5.2: Density plot of the spectral function $A(\mathbf{k}, \omega)$ for $t/U = 0.03$ and $\mu/U = 0.4$ at $\beta U = 40$, left column, and $\beta U = 5$, right column, on the 32×32 lattice. The particle densities are $\langle n \rangle = 1.0000006(6)$ for $\beta U = 40$ and $\langle n \rangle = 0.9371(1)$ for $\beta U = 5$, respectively. The dashed lines are mean field results and the solid lines are the results obtained from variational cluster approach. [101] The black error bars mark the center of the peak as obtained from the maximum entropy method.

correlators measured in the QMC algorithm. Section 5.4 and 5.5 contain the main results of this work. In particular, in Sec. 5.4 we investigate the spectral properties of the two-dimensional Bose–Hubbard model in Mott phase, where we observe gapped excitations. In addition, we study the stability of the gap with respect to temperature which is crucial for experimental observations. Section 5.5 contains a detailed discussion of the superfluid to normal fluid phase transition based on spectral signatures. Finally, we summarize and conclude our findings in Sec. 5.6.

5.3 Method

One quantity of interest is the dynamic structure factor

$$S(\mathbf{k}, \omega) = \frac{1}{Z} \sum_{m,n} e^{-\beta E_n} |\langle m|\hat{\rho}_{\mathbf{k}}|n\rangle|^2 \delta(\omega - (\omega_n - \omega_m)). \tag{5.2}$$

It is closely related to the excitations observed in Bragg-spectroscopy as well as in lattice modulation experiments. We use the so called directed loop method,[67] a generalization of the loop algorithm,[21, 73] which is an unbiased QMC technique, that allows—due to very low autocorrelations—to simulate large systems at low temperatures. We make use of the ALPS library [74, 75] and of the ALPS applications,[76] which use the *stochastic series expansion* (SSE) representation [15] of the partition sum.

To measure imaginary time dependent correlation functions $\langle n_i(\tau) n_j(0) \rangle$ and $\langle a_i(\tau) a_j^\dagger(0) \rangle$ efficiently, we implement the stochastic mapping from the SSE representation to a continuous time formulation. [77] Finally we obtain the dynamical structure factor, which

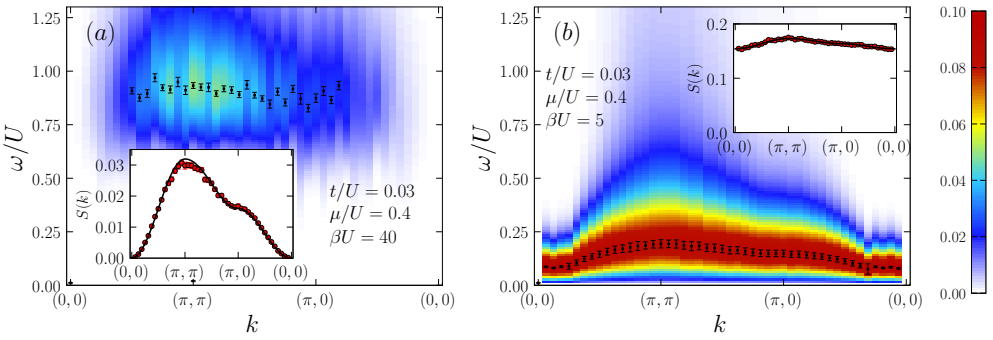

Figure 5.3: Dynamical structure factor $S(\mathbf{k},\omega)$ for the same parameters as in Fig. 5.2. The inset shows the static structure factor $S(\mathbf{k})$ directly measured in QMC (red dots) and fitted to $k + c\sum_{d=x,y}\sin(k_d/2)^2$ (black line).

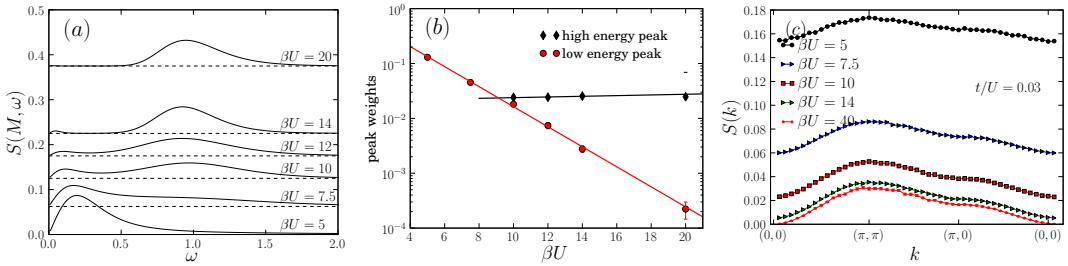

Figure 5.4: Dynamical structure factor $S(M,\omega)$ evaluated at the point $M = (\pi,\pi)$, left column, corresponding weight of the high and low energy peaks, midddle column, and static structure factor,right column, for different inverse temperatures β. $t/U = 0.03$, $\mu/U = 0.4$, and $L \times L = 32 \times 32$.

is the Fourier transformation of the density–density correlation function, by inverting

$$\langle \hat{n}_{\mathbf{k}}(\tau)\hat{n}_{-\mathbf{k}}(0)\rangle = \int d\omega S(\mathbf{k},\omega)\frac{\exp(-\tau\omega)}{\exp(\omega\beta)-1} \tag{5.3}$$

using of the aximum entropy method. We furthermore calculate the spectral function $A(\mathbf{k},\omega)$, by inverting an equation similar to Eq. 5.3, involving $\langle a_i(\tau)a_j^\dagger(0)\rangle$.

A more detailed explanation of the methods used can be found in Ref. [6].

5.4 Mott phase

In the Mott insulating phase the one-particle spectral function as well as the dynamical structure factor exhibit a gapped spectrum with the gap Δ approaching U as $t/U \to 0$. Furthermore we compare our QMC results to zero-temperature results obtained from a mean field calculation and the variational cluster approach [101] The latter fits nearly exactly to our calculations at $\beta U = 40$.

We want to point out, that at zero temperature and deep in the Mott phase already mean field calculations lead to reasonable results, which only slightly underestimate the size of the gap. This can be understood, since the size of the gap in the Mott phase can be directly extracted from the phase diagram. For a given t/U, the gap Δ is simply given by the width of the Mott lobe (in μ direction). Since mean field underestimates the size of the Mott lobe it is obvious that also the gap calculated in mean field is always smaller than the exact one. The discrepancy becomes larger when approaching the tip of the Mott lobe.

At higher temperatures, see Fig. 5.2 (b), the maximum of the particle– and hole–peaks move a bit further apart. However, since the excitations become broader, it is easier to create particles or holes leading overall to a smaller gap. Additionally to the two branches shown in the figure we observe nearly dispersionless high energy excitations with very small spectral weight,[102] which is about a factor 100 smaller than the weight of the low-energy particle or hole excitations.

We evaluate the dynamical structure factor $S(\mathbf{k}, \omega)$ at identical parameters as the single-particle spectral function $A(\mathbf{k}, \omega)$, see Fig. 5.3. At small temperatures (Fig. 5.3 (a)) the dynamical structure factor $S(\mathbf{k}, \omega)$ shows a nearly dispersionless feature at energy $\omega \sim U$. This has been observed in [53] and in the one dimensional case in [103], where it has further been that the static structure factor behaves like

$$S(\mathbf{k}) \propto \sin(\mathbf{k}/2)^2, \tag{5.4}$$

where $S(\mathbf{k}) = \int_0^\infty S(\mathbf{k}, \omega) d\omega = \langle \rho_{\mathbf{k}} \rho_{-\mathbf{k}} \rangle$. In the twodimensional case we observe the same behavior, see insets of Fig. 5.3, show the spectral weight $S(\mathbf{k})$ in the Mott insulating phase for the spectrum plotted in the main panel. We calculated the static structure factor directly in QMC, but we also integrated over $S(\mathbf{k}, \omega)$ to cross check. Both approaches yield compareable results within errorbars (data not shown).

For larger temperature an additional low energy excitation emerges, as can be seen in Fig. 5.3 (b). The behavior of the dynamical structure factor $S(\mathbf{k}, \omega)$ can be understood by simple perturbative arguments.[103, 104] For small hopping strength the ground state is occupied by n particles per lattice site, where n corresponds to the integer particle density fixed by the chemical potential. The first excited states are states where a particle is removed from one site and added to another site with respect to the ground state. We term these states *1ph*-states. The energy of the *1ph*-states is about U higher than the energy of the ground state. At zero temperature only excitations from the ground to the *1ph*-states are probed, leading to spectral weight at $\omega \approx U$, which is distributed according to Eq. (5.4). At nonzero temperature, the weight stays approximately constant, see Eq. (5.2). Yet, in addition a different kind of excitation between two *1ph*-states becomes possible. The energy difference of these states is only of the order the hopping strength t and their spectral weight is proportional to $\exp[-\beta U]$, see Eq. (5.2). In summary, the spectral weight at low energies becomes visible only at

large enough temperatures whereas the weight of the high energy excitation remains approximately constant. This behavior can be seen in Fig. 5.4, where $S(\mathbf{k}, \omega)$ (a), and the weight of the high and low energy peaks (b), are shown for various temperatures at $\mathbf{k} = (\pi, \pi)$. In addition, the temperature dependence of the static structure factor is shown in the Fig. 5.4 (c).

5.5 Superfluid to normal transition

In this section we display the spectral signatures associated with the crossover from superfluid to normal fluid phase. Please note that the investigated systems are of finite size. Thus, we do not expect to see a sharp phase transition at some specific value of temperature.

5.5.1 One-particle spectral function

At zero temperature, both the one-particle spectral function $A(\mathbf{k}, \omega)$ and the dynamic structure factor $S(\mathbf{k}, \omega)$ exhibit the characteristic, linear Goldstone modes in the superfluid phase.

Deep in the superfluid (large t/U) and at zero temperature, Bogoliubov theory is expected to be valid, which predicts excitations at energies

$$E_{\mathbf{k}}^{B} = \pm\sqrt{K_{\mathbf{k}}(2\,n\,U + K_{\mathbf{k}})} \tag{5.5}$$

with

$$K_{\mathbf{k}} = 4\,t\,(\sin(k_x/2)^2 + \sin(k_y/2)^2).$$

There are various more involved calculations, investigating the spectrum of the two-dimensional Bose Hubbard model in the superfluid phase at zero temperature. An early mean field calculation finds linear Goldstone modes. [98] In a variational mean field calculation, [53] in a work using a strong coupling approach, [51] and in RPA calculations [100, 57] coexisting linear and gaped modes have been found. But both in RPA and in strong coupling theory, for a given value of momentum $\mathbf{k}$, only two of the branches have significant weight. At positive ω/U the Goldstone mode is much stronger around $\mathbf{k} = (0, 0)$, while in the center of the Brillouin zone the gapped mode is much more significant. For $\omega < 0$ only the Goldstone mode has relevant weight. Furthermore in all of these approximations most of the spectral weight is to be found at momentum $\mathbf{k} = (0, 0)$.

The density plot in Fig. 5.5 shows our results lattice of size 32×32 and inverse temperature $\beta\,U = 40$.

The temperature is low enough to observe superfluid rather than normal fluid behavior. In addition we plotted the predictions from Bogoliubov theory, from RPA, and

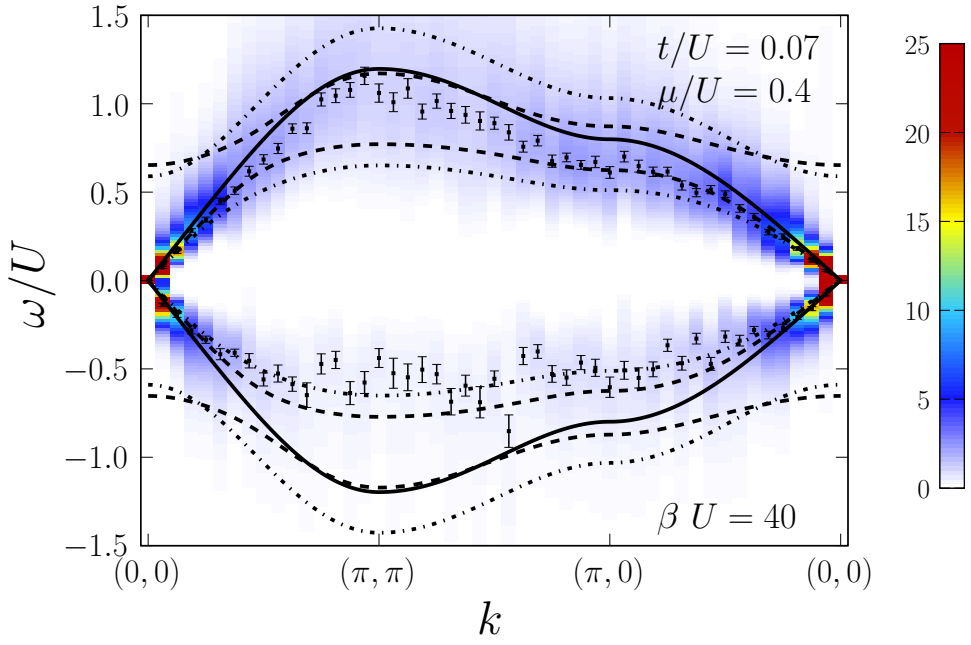

Figure 5.5: Density plot of the spectral function $A(\mathbf{k}, \omega)$ for $t/U = 0.07$ and $\mu/U = 0.4$ at $\beta U = 40$ and $L \times L = 32 \times 32$. The density is $\langle n \rangle = 1.03072(9)$. The solid lines are Bogoliubov modes Eq. C.1. The dashed lines show coupling results (Eq. 19 and 20 in Ref. [51]), and the dash dotted lines are from a RPA.

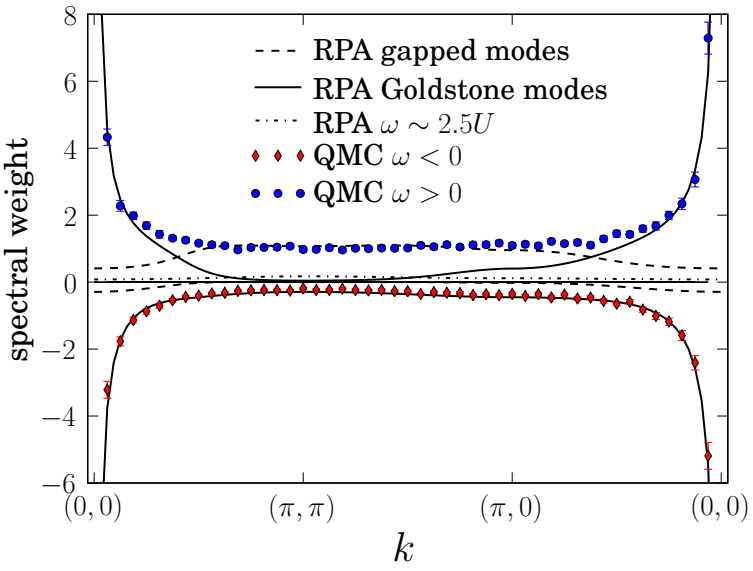

Figure 5.6: Spectral weigths of the modes shown in Fig. 5.5 and a comparison to RPA.

from strong coupling theory. Our data shows two instead of the four predicted modes. However, it is still consistent with the four mode theory, since our data exhibits the peak maximum wherever large spectral weight is expected form RPA and strong coupling theory. In the $\omega < 0$ region we only see the linear Goldstone mode. Since the gapped mode is, as mentioned before, predicted to be orders of magnitude smaller in intensity than the linear mode, we do not expect to be able to reconstruct the gapped mode from our Green's functions. What seems to be one mode in the region of $\omega > 0$ might as well be from two distinct modes, that we are unable to distinguish due to the broadness of the peak.

Let us now look into the temperature effects on the spectral function $A(\mathbf{k}, \omega)$. By increasing the temperature T, apart from the shift of spectral weight to larger momenta, we only observe significant changes at small $\mathbf{k}$. The upper linear Goldstone mode becomes quadratic, which is the signature of free bosons, while no weight remains in the branch with $\omega < 0$.

The crossover from linear to quadratic dispersion, i.e., from superfluid to normal fluid regime, is shown in Fig. 5.7. The superfluid stiffness ρ_s for the three cases are calculated according to

$$\rho_s = \frac{1}{2t} \frac{\langle W^2 \rangle \, L^{2-d}}{d \; \beta}, \tag{5.6}$$

with $\langle W^2 \rangle$ the winding number squared and dimension $d = 2$. For very small temperatures (Fig. 5.7 (a)) we observe the linear Goldstone modes. Fig. 5.7 (b) shows the

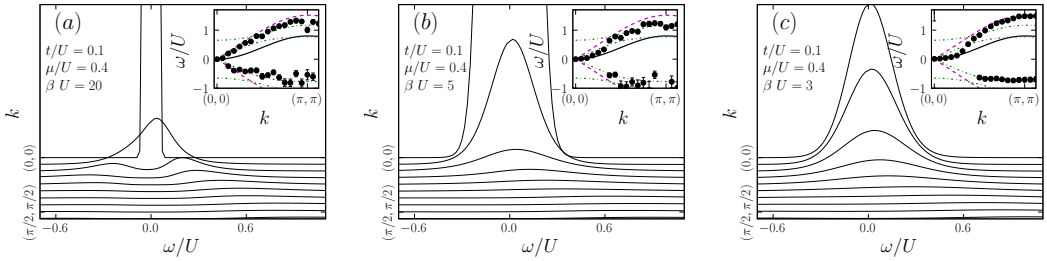

Figure 5.7: Spectral function $A(\mathbf{k},\omega)$ for $t/U = 0.1$ and $\mu/U = 0.4$ $\beta = 20$ (a), in the crossover region $\beta = 5$ (b), and in the normal fluid region $\beta = 3$ (c). $L\times L = 32\times 32$. The insets show the maxima of the peaks. The solid line is the excitation of a free boson, the dashed lines are the Bogoliubov results, and the dash dotted lines are RPA spectra. The superfluid densities are $\rho_s = 0.790(2)$, $\rho_s = 0.5343(7)$, and $\rho_s = 2(2)\ 10^{-6}$ from left to right, respectively. The associated particle densities are $\langle n\rangle = 1.12593(2)$, $\langle n\rangle = 1.10765(3)$ and $\langle n\rangle = 1.03859(9)$, respectively. The weights of the Goldstone peak from MaxEnt at $k = 0$ i.e. $\int A(0,\omega)d\omega$ are 1400, 728 and 25.4 from left to right. The approximate maximum values at $k = 0$ are 35000,3400 and 90, respectively. The same y-scale is used for all of the plots.

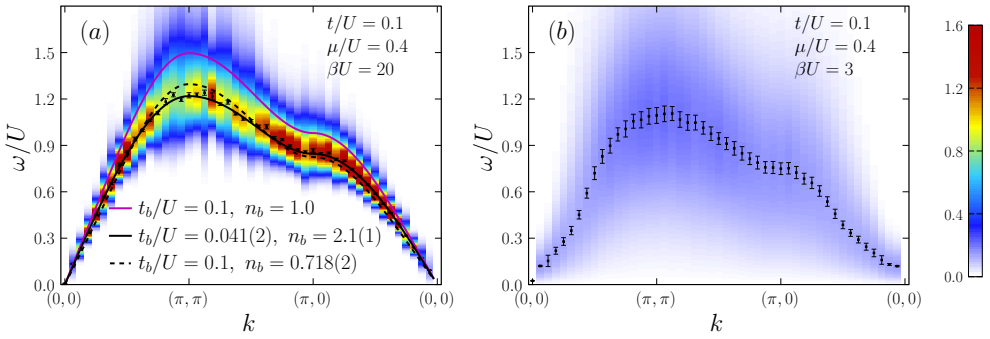

Figure 5.8: Density plot of the dynamical structure factor $S(\mathbf{k},\omega)$ at $\beta U = 20$ (left) and at $\beta U = 3$ (right). The system size is $L \times L = 32 \times 32$. The lines on the left hand side are fits to Bogoliubov theory. We use the actual parameters ($t/U = 0.1$ and $n = 1$) for the magenta line. For the solid black line, both t_b and n_b are optimized using a least squares fit and for the dashed line only the density n_b is used as a fitting parameter. The particle density is $\langle n\rangle = 1.12593(2)$ ($\langle n\rangle = 1.03859(9)$) on the left (right) hand side.

spectral weight evaluated in the crossover regime. Interestingly, in this regime already a quadratic dispersion appears , while there is still some very small weight in the $\omega < 0$ region. For larger temperatures (Fig. 5.7 (c)) we observe a quadratic dispersion for $\omega > 0$ and no spectral weight located at $\omega < 0$ as expected from normal fluid particles.

5.5.2 Dynamic structure factor

The situation is very similar in the case of the dynamic structure factor $S(\mathbf{k}, \omega)$. In the superfluid phase a linear spectrum can be observed Fig. 5.8, that can be explained at least qualitatively in terms of Bogoliubov theory (red solid line in Fig. 5.8). We plotted Eq. C.1 (solid and dashed lines) along with our data. When we use the actual parameters ($t/U = 0.1$ and $n = 1$), the agreement is only poor. However, as soon as a standard least squares fit is applied to find renormalized parameters t_b/U and/or n_b, we can always describe our data within Eq. C.1. This has to be kept in mind when e.g. experimental data is fitted to Bogoliubov theory to obtain the parameters of the model. Since Bogolibov theory is *quantitatively wrong* close to the phase transition, one should not determine parameters through a simple fit to Eq. C.1.

At high temperature this linear spectrum of the superfluid becomes slightly quadratic for small $\mathbf{k}$, see Fig. 5.8 (b). Apart from that we observe a broadening of the excitation with increasing temperature. This broadening is most pronounced in the center of the Brillouin zone. Yet, the position of the peak maximum stays nearly constant.

We thus plotted in Fig. 5.9 (a) the dynamic structure factor $S(\mathbf{k}, \omega)$ for $\mathbf{k} = (\pi, \pi)$ as a function of temperature. One can clearly see that in the superfluid region ($\beta U > 5$) the width of the peaks stays constant. This is in contrast to higher temperatures, where a dramatic increase of the width can be observed. In addition, we show the static structure factor in Fig. 5.9 (b). At low temperatures the weight of the static structure factor evaluated in superfluid phase is much larger than in the Mott phase, compare with Fig. 5.4 (c).

5.6 Conclusions

We calculated dynamic properties of the two-dimensional Bose–Hubbard model by means of quantum Monte-Carlo. In particular, we evaluate the single-particle spectral function $A(\mathbf{k}, \omega)$ and the dynamic structure factor $S(\mathbf{k}, \omega)$ at various temperatures and parameter configurations. As a technical point, we used the stochastic series expansion representation to evaluate the imaginary time correlators. The analytic continuation from imaginary time correlators to the spectral functions has been done with the maximum entropy method.

From the spectral properties we are able to characterize the three different phases present in the two-dimensional Bose–Hubbard model, which are the Mott insulating phase, superfluid phase and normal fluid phase. Strictly speaking the Mott insulating

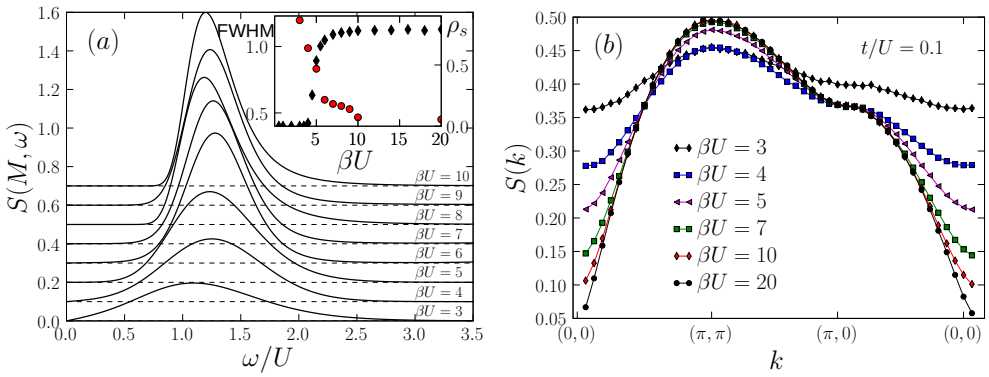

Figure 5.9: Dynamical structure factor $S(\mathbf{k}, \omega)$ at momentum $\mathbf{k} = (\pi, \pi)$, top panel, and static structure factor, botom panel, evaluated at different inverse temperatures β. $L \times L = 32 \times 32$, $t/U = 0.1$, and $\mu/U = 0.4$. The inset in the top panel shows the full width at half maximum (FWHM) of the peaks (red circles) and the superfluid stiffness ρ_s (black diamonds).

phase exists only at zero temperature. In view of spectral properties its main feature is that both the single-particle spectral function and the dynamic structure factor exhibit a gap roughly of size U. With our simulations we were able to show that the gap is still present at small but finite temperatures, which allows for an experimental observation of the Mott phase by investigating the spectral signatures. When increasing the temperature a gapless single-particle spectrum is observed and additional low energy excitations emerge in the structure factor.

At low temperatures yet for large hopping strength t/U we obtain a spectrum containing gapless and linear Goldstone modes, which indicate the superfluid phase. For increasing temperature the linear mode at positive energy becomes quadratic whereas the negative energy modes vanishe. This signales the crossover to the normal fluid phase.

Our results provide crucial information for experiments with ultracold gases of atoms trapped in optical lattices, since it became only recently possible to measure directly wave vector resolved dynamic properties in such systems. Due to the unprecedent control in experiments with ultracold gases of atoms it might become possible in near future to characterize the phases of the Bose-Hubbard model by measuring the spectral properties. Our numerical data then might be useful for characterizing these phases.

5.7 Acknowledgments

We acknowledge financial support from the Austrian Science Fund (FWF) under project no. DK W1203-N08 (P.P.) and under the doctoral program “Numerical Simulations in Technical Sciences” No. W1208-N18 (M.K.). We made use of the ALPS library and the ALPS applications.[74, 76]

6 Excitations of Trapped Bosons in One Dimension

Let us now turn to the case that is most closely related to the experimental setup. In typical experiments, an atomic beam is slowed down using Zeeman tuned laser cooling techniques. These cold gases are then trapped using magnetic or magneto–optical traps in order to keep the atoms localized. In these traps, evaporative cooling is applied to further cool the gas down until they condense into a Bose–Einstein condensate (BEC). The BEC is transferred to an optical lattice which results in a system described by the Bose–Hubbard model. As opposed to the simpler cases discussed in the previous chapters, one has to keep the gas in a trapping potential. These potentials can be created in various shapes, but quadratic potentials are most commonly used.

We consider again the Bose–Hubbard model in one dimension, but with an additional quadratic potential

$$\hat{H} = -t \sum_{\langle i,j \rangle} \hat{a}_i^\dagger \hat{a}_j + \frac{U}{2} \sum_i \hat{n}_i(\hat{n}_i - 1) - \sum_i (\mu_0 - K(i - L/2)^2)\hat{n}_i. \tag{6.1}$$

The DMRG phase diagram is shown in Fig. 4.1 on page 30. A schematic zero temperature phase diagram is replotted in Fig. 6.1. Due to the special form of the potential $\mu(r_i)$, the phase in which the atoms are depends strongly on the position r_i. Thus given that t/U is small enough, the system undergoes phase transitions from Mott insulating to superfluid regions as a function of r_i. This results in a so called wedding cake structure of the density $n(r_i)$, that is superfluid regions with varying density enclosed by Mott shells with constant integer density.

We are again mainly interested in dynamical properties like the dynamical structure factor $S(k, \omega)$ and the one particle spectral function $A(k, \omega)$. These have been measured by various groups, first with lattice modulations at $k = 0$, and later more directly with Bragg spectroscopy for a few momenta in the Mott insulator as well as in the superfluid phase [31, 3, 105, 106]. Recently even the full momentum resolution has been presented in the superfluid region [4].

Experiments have so far only been compared to simple Bogoliubov or mean field calculations. Even though they agree well in many cases, it is important to compare to results obtained from numerically exact methods - which do not need any fitting parameter to adjust.

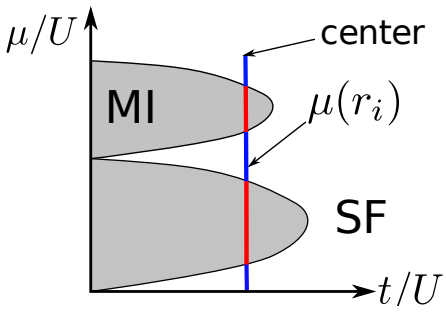

Figure 6.1: Schematic phase diagram of the Bose–Hubbard model. Mott insulating (MI) lobes enclosed by superfluid (SF) regions. For a given t/U the chemical potential $\mu(r_i)$ changes from a maximum value in the center to zero on the edge. Depending on the position r_i, the system is either in the Mott insulating (red) or in the superfluid phase (blue).

6.1 Experimental and Numerical Parameters

As mentioned earlier, for large lattices, the parameters of the microscopical Hamiltonian can directly be compared to experimental quantities [29]. The hopping amplitude is given by

$$t = \frac{4}{\sqrt{\pi}} E_r \left(\frac{V_x}{E_r}\right)^{3/4} \exp(-2\sqrt{V_x/E_r}) \tag{6.2}$$

and the on-site potential reads

$$U = 4\sqrt{2\pi}\frac{a_s E_r}{\lambda}\left(\frac{V_x V_\perp^2}{E_r^3}\right)^{1/4} \tag{6.3}$$

with V_x the depth of the periodic potential. $V_\perp$ is the potential depth in directions y and z, $E_r = \hbar^2 k^2/2m$ is the recoil energy, a_s is the s–wave scattering length and λ is the wavelength of the standing light field.

In recent experiments by the Florence group [31, 3] a 3D BEC is trapped in two orthogonal optical lattices ($\lambda = 830$nm) with an amplitude $V_\perp = 35E_r$. This results in independent 1D BECs since the transverse hopping is much smaller than the inverse time scale of the experiment. The longitudinal potential $V_x = s_x E_r$ drives the system in the strong coupling regime. Excitations as a function of the lattice depth s_x have been investigated ($0 < s_x < 30$) with two photon Bragg spectroscopy. The 3D BEC consisted of approximately $N_b = 10^5$ particles, thus in each 1D system they have approximately 300 particles.

In the experiment mentioned above, ^{87}Rb atoms have been used. We set $a_s = 5.45\,\text{nm}$ for the s-wave scattering length. Plugging the numbers in Eq. 6.2 and Eq. 6.3 we find that the hopping strength varies from $t/U = 0.005$ up to $t/U = 0.2$ (see table 6.1)

Table 6.1: Comparison of the hopping parameter t/U to the experimental parameter $V_x = s_x E_r$ for ^{87}Rb and $\lambda = 830$nm.

s_x	5	7	10	15	20
t/U	0.209	0.109	0.046	0.013	0.005

Since we know that there are about 300 particles in each 1D system and following Ref. [31, 3] we know that there are about three particles in the center of the trap we can tune μ_0/U and K such that the experimental situation is well captured by our simulation.

In the simulations presented below we chose $L = 180$, $\mu_0 = 0$ and $K = 0.001$ which results in a particle number between $n = 230$ ($t/U = 0.01$) and $n = 300$ ($t/U = 0.3$).

6.1.1 A Note on Dimensionless Quantities

In other experiments by other groups a larger number of particles has been used. This would make calculations much more time consuming. However, it has been pointed out by various authors [107, 108, 109], that only the actual shape of the density profile $n(i)$ is important rather than the exact values of the parameters. To be more precise, using a rescaled length $\xi_i = r_i/\xi$ with $\xi = \sqrt{t/K}$, the resulting density profiles only depend on the so called *characteristic density* $\widetilde{\rho} = N/\xi^d$, where d is the dimension and N the number of particles in the system. It is thus possible to compare calculations with much smaller N to experimental situations also quantitatively, by using the same characteristic density $\widetilde{\rho}$.

6.2 Static properties

Let us first discuss some static properties of the system to characterize the state. As mentioned above, the most important quantity is the shape of the density $n(i) = \langle \hat{n}_i \rangle$. Typical density profiles are shown in Fig. 6.2 (red diamonds) for various t/U and temperatures βU. Parameters are close to those of the experiments described above (Ref. [31, 3]). One can see the wedding cake structure for small t/U: i.e. Mott insulating regions (constant density) interrupted by small superfluid shells.

6.2.1 Density Fluctuations and Compressibility

To characterize the local state (superfluid or Mott insulating), we can no longer take the superfluid density ρ_s as used in the chapters above as the global world line-winding number squared. Instead of that we need some local quantity that signals whether we have a superfluid or a Mott insulating phase. One way to probe the local properties is

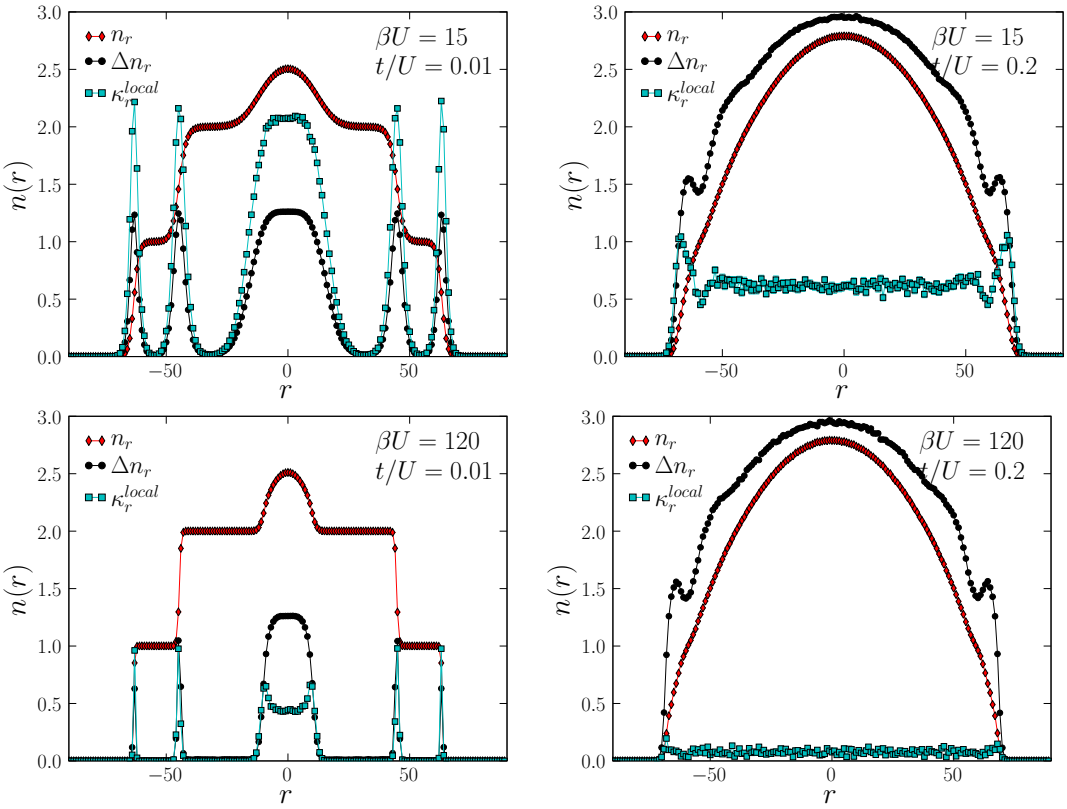

Figure 6.2: Density profiles (red) for various hopping parameters t/U and temperatures β. In addition Δn_r and κ_r^{local} is plotted in arbitrary units.

to measure the density fluctuations

$$\Delta n_r = \langle \hat{n}_r^2 \rangle - \langle \hat{n}_r \rangle^2 . \tag{6.4}$$

In Ref. [110] the so called *local compressibility*

$$\kappa_i^{local} = \frac{\partial \langle N \rangle}{\partial \mu_i} = \int_0^\beta d\tau \left(\langle n_i(\tau) N \rangle - \langle n_i(\tau) \rangle \langle N \rangle \right), \tag{6.5}$$

has been defined. That is the response to a local change of the chemical potential of the total particle number N. $n_i(\tau) = e^{\beta H} n_i e^{-\beta H}$ is the imaginary time dependent density.

We plotted Δn_r along with κ_i^{local} in Fig. 6.2. For large lattice depths $t/U = 0.01$ ($\sim s_x = 15$), one can clearly distinguish the Mott plateaus from the superfluid regions, as long as the temperature is low enough. For smaller s_x (larger t/U) the Mott regions are very narrow, thus nearly all of the particles are in the superfluid phase. Small tips

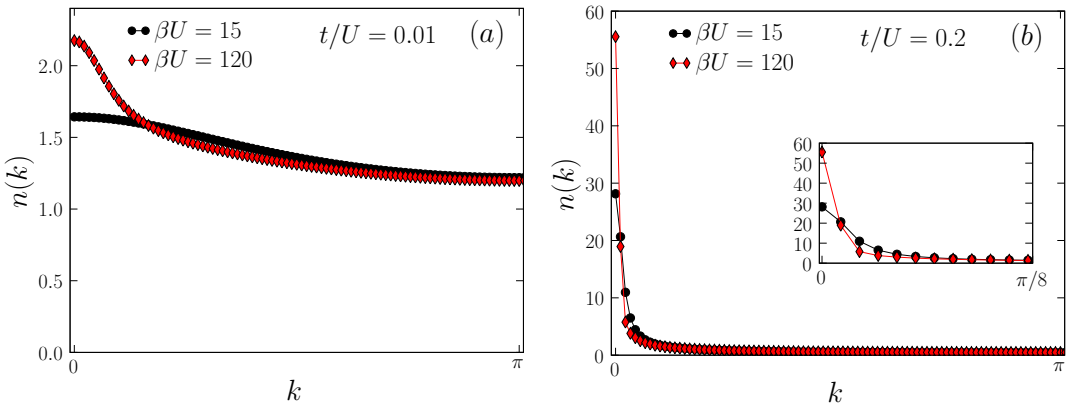

Figure 6.3: Momentum distribution function $n(k)$. $t/U = 0.01$ (a) and $t/U = 0.2$ (b). The inset in (b) is a magnification for small momenta. Compare to the density profiles in Fig. 6.2. Note the different y-scale in (a) and (b).

in the compressibility and the density fluctuations mark the regions where the Mott phase is crossed.

6.2.2 Momentum Distribution Function and Correlations

The momentum distribution function

$$n(k) = \frac{1}{N} \sum_{i,j} e^{ik(r_i - r_j)} \langle \hat{a}_i^\dagger \hat{a}_j \rangle \tag{6.6}$$

is of special interest since it can be measured directly in experiments in time-of-flight (ToF) measurements. Here N is the total number of particles, to normalize $n(k)$. Then, $n(0)$ should give the coherence fraction of the condensate. Sharp peaks in $n(k)$ are usually interpreted as the signature of superfluidity. This should be taken with care, since it has been shown by Kato *et al.* [111], that also above T_c sharp peaks are visible on a broad background. They show, that a very narrow peak on top of the broader peak, centered at $k = 0$ is the true signature of the superfluid.

Here, we show results for the 1D system, where strictly speaking a superfluid only exists at $T = 0$ (see Fig. 6.3). However one can qualitatively distinguish between the broad feature of the Mott insulator dominated region at $t/U = 0.01$ (Fig. 6.3 a) and the very sharp peak at $t/U = 0.2$ (Fig. 6.3 b). In both cases the peaks become significantly broader, when temperature is increased.

A further quantity of interest is the one particle density matrix or correlation function

$$g(i,j) = \langle \hat{a}_i^\dagger \hat{a}_j \rangle \tag{6.7}$$

In Fig. 6.4 we measure $g(s, s-r)$ for a site $s = -9$ close to the edge of the superfluid

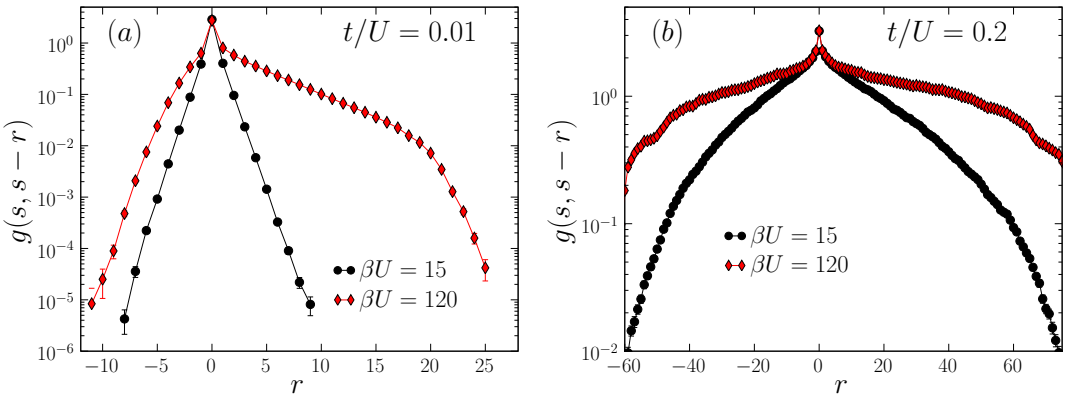

Figure 6.4: Correlation function $g(s, s-r)$ from site $s = -9$, which is close to the edge of the superfluid region in the middle. Again, $t/U = 0.01$ (a) and $t/U = 0.2$ (b). Parameters are the same as in Fig. 6.3.

region in the middle of the system. The parameters are the same as for the density profiles in Fig. 6.2. First of all, it is important to notice, that at low temperatures correlations become much more important. Further more, for large $t/U = 0.2$ where nearly all particles are superfluid, there are large spacial correlations.

The correlation length ξ is fitted using a standard least squares fit to $Ae^{-r/\xi}$ for positive r and give:

$t/U = 0.01$	$\beta = 15$	$\xi = 0.702(2)$
$t/U = 0.01$	$\beta = 120$	$\xi = 4.48(2)$
$t/U = 0.2$	$\beta = 15$	$\xi = 24.6(2)$
$t/U = 0.2$	$\beta = 120$	$\xi = 75(1)$

($r > 2$ for $t/U = 0.01$ and $r > 5$ for $t/U = 0.2$ respectively)

6.3 Excitation Spectra

Experimentally, it is fairly clear what happens overall during a Bragg-spectroscopy measurement, but the processes involved on a microscopic scale are a subject of current discussion.

Shortly before the gas expands, two Bragg pulses are applied. These are two laser beams with momenta $\hbar k_1$ and $\hbar k_2$ and energies ν_1 and ν_2 respectively. After the absorption of a photon from the first laser, the photon is emitted into the second laser via stimulated emission, transferring energy $\hbar\omega = \hbar(\nu_1 - \nu_2)$ and momentum $\hbar k = \hbar(k_1 - k_2)$ to the atomic cloud [112].

It is usually argued, that the energy transfer as function of k and ω is given by

$$E(k, \omega) \sim \omega S(k, \omega) \tag{6.8}$$

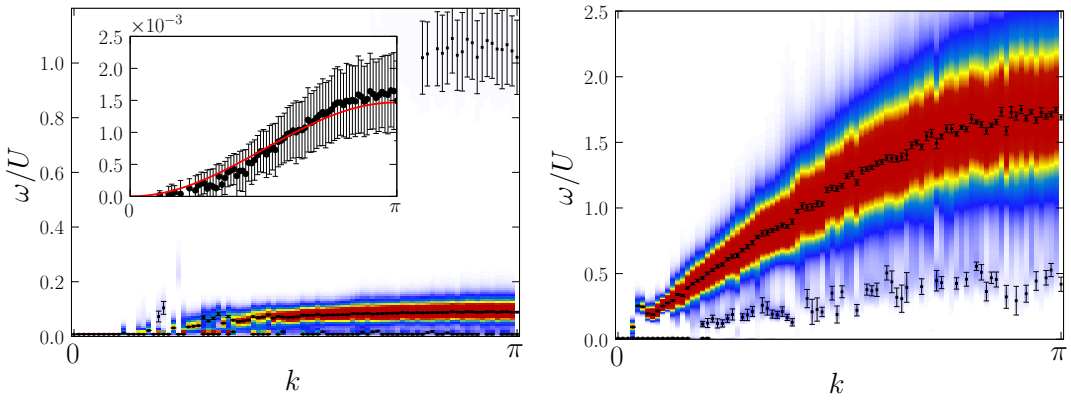

Figure 6.5: Dynamical structure factor $S(k,\omega)$ for the density profiles depicted in Fig. 6.2. $t/U = 0.01$ (left) and $t/U = 0.2$ (right) at $\beta U = 120$. The inset on the left hand side shows the weight of the excitation at $\omega/U = 1.0$ and a fit to $c\ \sin^2(k/2)$ (red line).

In Ref. [106] it is argued that, depending on the energy bands that are involved in the two photon transition, the excitations are either related to $S(k,\omega)$ or $A(k,\omega)$. The low energy response of Bragg spectroscopy (typically $\omega < 2\pi\,10$kHz) can be described by the structure factor, which corresponds to density fluctuations. For high excitation energies ($\omega > 2\pi\,30$kHz) it is argued that the single-particle spectral function is measured. Atoms which are excited into high-energy bands do not interact with the lower bands. Thus, the measured spectrum is described by a convolution of the density of states of the lower occupied with the upper unoccupied band. From this convolution the spectral function of the lower strong-correlated bands can be extracted [106, 113].

A problem that needs to be discussed is, that momentum is not conserved in the experiment. When a boson is excited and momentum is transferred, the momentum may have changed when the stimulated emission takes place. We ignore this problem and assume, that stimulated emission takes place instantaneously after the absorption. That might be a problem when small energies are involved, because small energies can be translated into large time–scales, in which the momentum is no longer conserved.

This problem is however also ignored in all simpler approaches such as mean field calculations or in perturbation theory [103]. Here we treat the system as if there were periodic boundary conditions (assuming that k is still a good quantum number) and set k equal to the momentum transfer during a Bragg experiment.

Fig. 6.5 shows two examples of the dynamic structure factor for the density profiles shown in Fig. 6.2 at temperature $\beta U = 120$.

In the small hopping regime ($t/U = 0.01$), in addition to the main feature at $\omega/U \sim 0.1$, which we attribute to the superfluid parts of the condensate, there is a very small excitation at $\omega/U \sim 1$. This is only barely visible in the density plot, but we draw the weight of the excitation as a function of k in the inset on the left hand side of

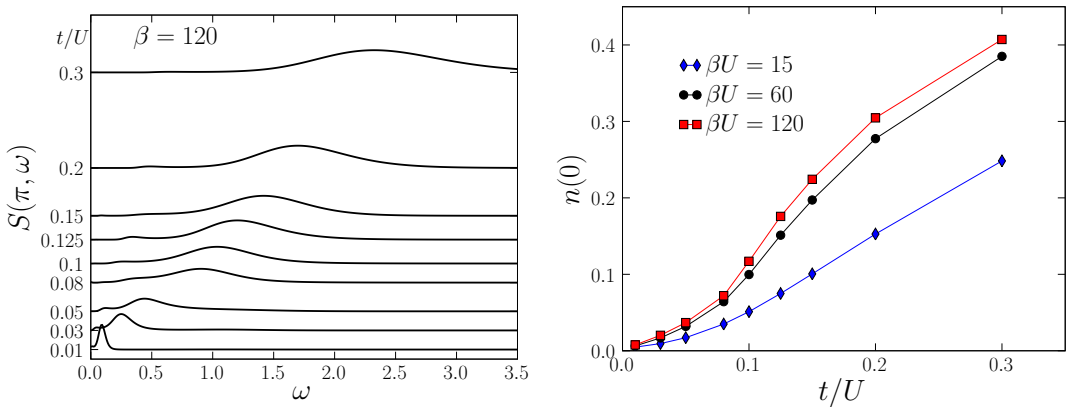

Figure 6.6: left: Dynamical structure factor at $k = \pi$ for various hopping strengths t/U and $\beta U = 120$ (left) and the condensate fraction $n(0)$ as a function of t/U for various inverse temperatures (right). The Mott excitations at $\omega \sim U$ which are only barely visible in Fig. 6.5 are too small to be seen in this figure.

Fig. 6.5. The weight of the excitation can be described with a $\sin^2(k/2)$ behavior. We thus identify this as the signature of the Mott insulating regions of the condensate (compare to the inset of Fig. 5.3 on page 59 and the discussion of Eq. 5.4 on page 60).

This feature at constant energy is absent in the pure superfluid region $t/U = 0.2$ (see right hand side of Fig. 6.5), where one main superfluid feature is visible together with a weaker excitation at smaller energies that also shows the signatures of a superfluid.

It is remarkable however that in both large and small hopping regions the superfluid signatures are dominant. This can be understood when we compare to our data of the homogeneous system. At low temperatures, the static structure factor $S(k)$, which is the integrated spectral wheight, is about 100 times larger in the superfluid region (Fig. 5.9 (b)) than in the Mott insulating region (Fig. 5.4 (c)).

In Fig. 6.6 we plot the dynamic structure factor $S(k, \omega)$ at $k = \pi$ for different hopping strengths t/U. Both the Mott bands at $\omega/U \sim 1$ and the low energy bands at larger t/U are only barely visible. The main feature (wich we attribute to the superfluid phase) grows linearly (or close to linearly). From simple Bogoliubov theory arguments (see section 4.5.1.1 on page 33) it is known that the sound velocity is proportional to $\propto \sqrt{nt}$. Given the actual form of the spectrum, the sound velocity determines the bandwidth – at least to some extend. In the simulations n is not constant but smaller for $t/U = 0.01$ than for $t/U = 0.2$. Thus, this "smaller than linear"–behaviour is consistent with our observation that this peak stems from the superfluid phase.

On the right hand side of Fig. 6.6 the condensate fraction, which is up to some normalization constant $n(0)$ where n is defined in Eq. 6.6. Since there are always superfluid regions between the Mott insulating shells, the condensate fraction never vanishes completely, as it would do in the homogeneous case for small t/U. As a matter

of course, finite temperature suppresses the amount of superfluidity significantly.

In conclusion we find, that the qualitatively different situations (see Fig. 6.2) for small and large hopping are not only visible in e.g. the momentum distribution function Eq. 6.6 but also in the Bragg spectrum.

Part III

One Dimensional Conductors Coupled to Phonons

7 QMC Simulation of the 1D Holstein Model

Different from the situation in cold atoms, in a *real* solid a description in terms of low energy Hamiltonians is always accompanied by severe approximations. Interactions with the core electrons, impurities and lattice defects are very often discarded.

In this chapter we want to include phononic degrees of freedom which is necessary very often to understand physical properties of many fascinating systems. They become even more important in low dimensional systems where strong electron-electron and electron-phonon correlations result in rich physics. Fascinating examples include conjugated polymers or quasi one dimensional charge transfer salts. [114]

The aim of this chapter is to introduce an efficient Quantum Monte Carlo method based on a world line representation of the partition sum.

We describe the method and apply it to the simplest model, that includes electronic and phononic degrees of freedom, namely the Holstein model of spinless fermions in one dimension. However the method can be applied to more involved models without algorithmic complications. After a short introduction of the model in section 7.1 we will describe the method in some detail in section 7.2.

We then present some tests and results in section 7.3. In particular we calculate dynamical properties such as the dynamical structure factor or the phonon spectral function.

7.1 Model

The Holstein model of spinless fermions in one dimension that couple to dispersionless phonons reads

$$\begin{aligned} H = & \underbrace{-t\sum_i (\hat{c}_i^\dagger \hat{c}_{i+1} + h.c)}_{\hat{H}_e} \underbrace{- g\sum_i \hat{x}_i(\hat{c}_i^\dagger \hat{c}_i - \frac{1}{2})}_{\hat{H}_{e-ph}} \\ & + \underbrace{\omega_0 \sum_i (\hat{a}_i^\dagger \hat{a}_i + \frac{1}{2})}_{\hat{H}_{ph}}, \end{aligned} \tag{7.1}$$

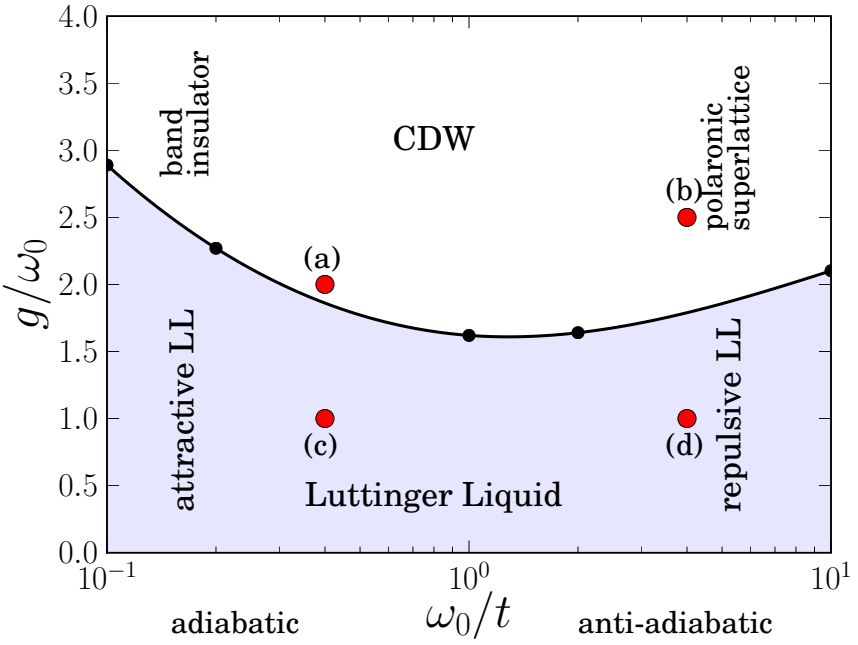

Figure 7.1: Zero temperature phase diagram of the one dimensional Holstein model of spinless fermions obtained from DMRG [115]. For small coupling the model exibits Luttinger liquid behaviour while for large g/ω_0 it is in a charge density wave (CDW) insulating phase. We distinguish the adiabatic and anti-adiabatic regions respectively. The red dots mark specific points in the phase diagram at which we perform our calculations.

with bosonic creation (annihilation) operators $a_i^\dagger$ (a_i) and fermionic ones $\hat{c}_i^\dagger$ ($\hat{c}_i$) respectively. $\hat{x}_i$ denotes the elongations of the harmonic oscillators $\hat{x}_i = (\hat{a}_i^\dagger + \hat{a}_i)$. During the last 50 years in which this model has been studied, many different definitions of the model have been introduced. In appendix D an overview over the most commonly used definitions of coupling constants is given.

Here we consider the simplest form of such a Hamiltonian, namely the Holstein model of spinless fermions coupled to Einstein phonons. We want to point out that the method described below is also applicable to more complicated models, namely to all models with momentum dependent coupling g_q and phonon dispersion ω_q as long as the electronic part of the Hamiltonian is sign problem free for $g = \omega = 0$. [1]

The Holstein model of spinless fermions exhibits a phase transition from a metallic towards an insulating phase with increasing electron phonon coupling g (see Fig. 7.1). In the limit of $\omega_0 \to 0$ (adiabatic limit) the critical coupling g_c goes to zero, meaning that every finite g leads to a Peierls distortion. In the limit of $\omega_0 \to \infty$ (anti–adiabatic limit) the model can be transformed to the XXZ model, which is exactly solvable and

[1] Applications of the method to more involved models will be published elsewhere.

exhibits a Kosterlitz-Thouless (KT) phase transition [116].

Monte Carlo [117, 115], variational [118] and RG [119] calculations determined the phase boundary, but results from the various approaches differed a lot. More precise DMRG [120, 121] and ED [122] calculations yield the now well established phase diagram (see Fig. 7.1).

Dynamical properties have been observed by Hohenadler *et al.* [123] using a exact diagonalization and the cluster perturbation theory. This is a perturbative method, where the system is divided into identical clusters. On each small cluster the Hamiltonian is diagonalized exactly and the interaction with the remaining clusters is added in a variational way. In the case of the Holstein model, there is no phonon–phonon interaction, thus there is the same information for the phonon spectral function on the total system than on a small cluster. However, the results from the small cluster are exact.

They found a phonon softening (hardening) in the attractive (repulsive) LL, and determined the phonon spectral function in the band insulator (ω_0 small, g large)and in the polaronic superlattice phase (ω_0, g large). Sykora *et al.* [124, 125] used the so called projector–based renormalization method to study the dynamics of the Holstein model obtaining results for the one–particle spectral function and the phonon spectral function. Although their results turn out to to be extremely accurate, they were unable to perform calculations in the insulating phase at large t/ω_0. Furthermore the method introduces uncontrollable sources of error and might not be the method of choice for other models.

Using a determinatal QMC, Creffield *et al.* [126] studied the phonon softening in the CDW phase. For a slightly different model – the spinfull Holstein model at quarter filling – a diagrammatic determinantal QMC procedure has been implemented to calculate e.g. the dynamic structure factor and one particle spectral functions. [127, 128] Unfortunately, these determinantal QMC calculations are limited to rather small system sizes ($L \sim 20$).

The QMC method presented below can be used for large system sizes at low temperatures. The only errors that are present are statistical errors and a time discretizetion error in the phonon coordinates. This time discretizetion error can however be controlled very well by starting from a coarse time grid which is made finer and finer until convergence is reached.

7.2 Method

The outline of our method is as follows: We start from a path integral representation of the partition sum $e^{-\beta H[\{n_i(\tau),x_i(\tau)\}]}$, with $\{n_i(\tau)\}$ denoting the electron density of some configuration in the path integral and the $\{x_i(\tau)\}$ some phonon elongation respectively. i is the site index while τ represents imaginary time. We then update

the electronic configuration using a directed loop algorithm, [24, 25] arriving at some new configuration $\{n_i'(\tau)\}$. Keeping the new electronic configuration $\{n_i'(\tau)\}$ constant we update the phonons in Fourier space, where the problem is bi-quadratic and a new phonon configuration $\{\widetilde{x}_k'(\omega)\}$ can thus be sampled from a normal distribution. The new phonon configuration is transformed back to real space, and the procedure is started again by updating the electronic configuration.

The same idea has been used by Michel and Evertz to study spin–Peierls systems [11, 12]. Instead of a path integral representation, the SSE has been used for the electronic part of the partition sum. This is however not the optimal choice, when off-diagonally dominated Hamiltonians are studied.[2] Another difference compared to Ref. [11, 12] is a slightly different treatment of the phonons. In contrast to a continous time path integral representation and a cutoff in the Matsubara frequencies in Ref. [11, 12], a discretized version of the path integral is used here. Then, no cutoff has to be introduced in Fourier space since the discretization has already been performed in real space.

In both cases an error – cutoff or time discretization – has to be introduced, which is comparable large.

Starting from a world line path integral representation we denote the partition sum as

$$\begin{aligned} Z &= \mathrm{Tr}(e^{-\beta H}) \\ &= \mathrm{Tr}_e \int \mathcal{D}x \, \exp\left(- \int_0^\beta d\tau H[\{n_i(\tau), x_i(\tau)\}] \right), \end{aligned} \tag{7.2}$$

where Tr_e is a trace over the electronic parts of freedom and $\int \mathcal{D}x$ indicates the path integral over all possible phonon elongations $x_i(\tau)$.

In order to handle the problem numerically we introduce some time grid to store the phonon elongations only on times $t = n\,\delta\tau$, $n = 0, \ldots N-1$ and $N = \beta/\delta\tau$. Note that the electronic configurations are known without any time discretization error, since we only store the times where a kink in the world line configuration occurs.

7.2.1 Update of the Electronic Configuration:

Although Eq. 7.2 is written in continous time, we start with a time discretized version of the partition sum (compare to Eq. 2.3 on page 6 or Fig. 2.1 on page 7) and perform the continous time limit for the electrons in section 7.2.1.3.

The update rules are calculated according to the directed loop algorithm (see chapter IV in Ref. [25] for a discussion of directed loops using a path integral representation).

[2] If there are no diagonal terms in the Hamiltonian, one can either simulate only at constant length of the operator string n, which is a simulation at constant energy, or introduce artificial unit operators in the Hamiltonian to overcome this problem.

One starts the electronic update by chosing one corner of one plaquette randomly from the current configuration of the partition sum (see Fig. 2.1 on page 7). Both the loop head and the loop tail are put onto this corner. While the loop tail stays on this edge, the loop head moves around, according to the rules specified below, changing the local state of each corner which has been visited. This continues until the loop head hits the loop tail again. At this piont we arrived at a valid contribution to the partition sum again.

To calculate the rules for the loop head, we need to evaluate the weights of the plaquettes W_s, depending on the spin configuration s. Furthermore the weights of the possible paths on each plaquette need to be calculated. This is done in the subsequent subsections.

7.2.1.1 Determination of the plaquette weights

Let us start with the calculation of the plaquette weights that determine the probabilities for the path of the loop head. Fist, let us rewrite the Hamiltonian in a more symmetric form, such that it acts on one plaquette

$$H_e + H_{e-ph} = -t \sum_i (\hat{a}_i^\dagger \hat{a}_i + \text{h.c.}) - \frac{g}{2} \sum_i [\underbrace{(\hat{n}_i - 1/2)}_{\hat{s}_i} \hat{x}_i + \underbrace{(\hat{n}_{i+1} - 1/2)}_{\hat{s}_{i+1}} \hat{x}_{i+1}]. \quad (7.3)$$

We defined $\hat{n}_{i+1} - 1/2 \equiv \hat{s}_i$ to simplify notation. Note that the possible quantum numbers of $\hat{s}_i$ can either be $+1/2$ or $-1/2$. Thus we will denote the associated states as $|\uparrow\rangle$ and $|\downarrow\rangle$ respectively. With this at hand we can write down the plaquette weights

$$W_p = \langle \beta | e^{-\Delta\tau H_p} | \alpha \rangle \,.$$

The states $|\alpha\rangle$ and $|\beta\rangle$ are the states of the plaquettes at the two different time slices (see fig. 7.2 upper left panel). We assume that $x_i(\tau) = x_i(\tau + \Delta\tau)$ because later on we will do the limit of $\Delta\tau \to 0$ while we will keep the finite number of time slices on which the phonon elongations $x_i(t)$ are defined constant.[3] We then find the off diagonal plaquette weight (where is $\langle\alpha|\beta\rangle = 0$) W_1 and the diagonal ones ($\langle\alpha|\beta\rangle = 1$) $W_{s_i,s_{i+1}}$ up to first order in the exponential to be

$$W_1 = \langle\uparrow\downarrow | e^{-\Delta\tau H_p} | \downarrow\uparrow\rangle = \langle\downarrow\uparrow | e^{-\Delta\tau H_p} | \uparrow\downarrow\rangle \approx t\,\Delta\tau \quad (7.4)$$

$$W_{s_i,s_{i+1}} \approx 1 + \frac{g}{2} \left[s_i(\tau) x_i(\tau) + s_{i+1}(\tau) x_{i+1}(\tau) \right] \Delta\tau, \quad (7.5)$$

where $s_i(\tau)$ is the eigenvalue of the operator $\hat{s}_i$ at time τ. Since we later let $\Delta\tau$ go to zero it is sufficient to expand the exponential up to first order.

[3] We denoted the time grid for the phonons as $t = n\,\delta\tau$ with $n = 0, \ldots N-1$ and $N = \beta/\delta\tau$. This is kept constant throughout the derivation of the electronic update. To make the assumtion $x_i(\tau) = x_i(\tau + \Delta\tau)$ valid let us assume that $\Delta\tau \ll \delta\tau$. Note that this is reasonable since the limit $\Delta\tau \to 0$ will be performed.

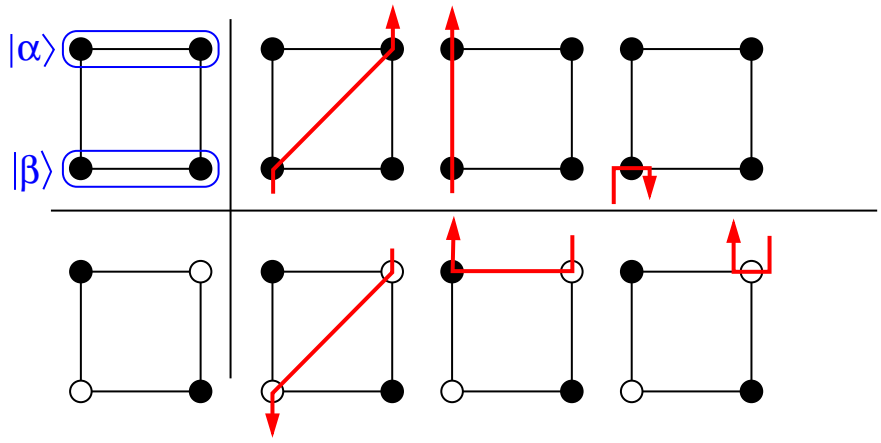

Figure 7.2: Two examples of plaquettes before the update (very left). Black and white circles denote occupied and empty sites respectively. The states $|\alpha\rangle$ and $|\beta\rangle$ are the states at the times $t + \Delta\tau$ and t respectively. The three panels on the right hand side show the possible paths of the loop head.

7.2.1.2 Detailed balance

Let us consider a plaquette with weight W_s and an electron configuration s and assume that the loop head enters the plaquette on one corner e. We want to find the probabilities that the loop leaves the plaquette on some other corner x changing the electron configuration to s' and the weight to $W_{s'}$. Let $p(x|e,s)$ be the probability that the exit leg of the loop is x. The detailed balance condition then reads

$$W_s p(x|e,s) = W_{s'} p(e|x,s'). \tag{7.6}$$

We further denote $W(s,e,x) = W_s p(x|e,s)$ as the weight of one particular path through one plaquette. Since a loop always continues – that is one exit corner is always chosen – it follows that $\sum_x p(x|e,s) = 1$. Thus

$$\sum_x W(s,e,x) = W_s. \tag{7.7}$$

By solving eq. (7.7) together with eq. (7.6) we can determine the path weights for the loop head. For example eq. (7.7) applied to the two plaquettes depicted in fig. 7.2 one has the following equation

$$W_{\uparrow\uparrow} = d + v + B_1 \tag{7.8}$$
$$W_1 = d + h + B_2 \tag{7.9}$$

where d is the weight of the diagonal path through the plaquette and v, h and B correspond to the weights of the vertical, horizontal and the bounce move respectively.

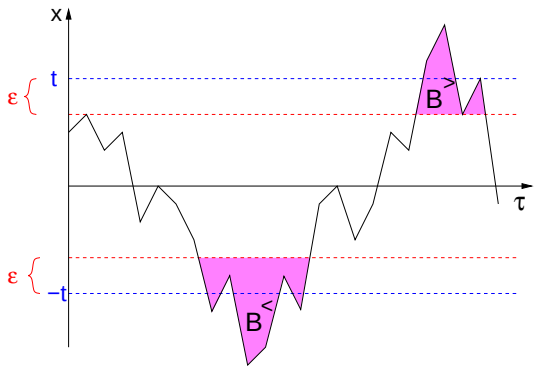

Figure 7.3: Imaginary time evolution of $x(\tau)$. If $|x|$ is larger than some threshold, bounce weights are set to some non-zero values.

The two diagonal path weights in eq. (7.8) and eq. (7.9) are equal due to the detailed balance condition eq. (7.6). One also finds the time reversal symmetry: by flipping the plaquette (and the path through it) upside-down the weights are not changed. Using these symmetries and writing down all the equations for all possible paths one finds a set of 12 linear equations with the following solution. Let us label the corner sites of the plaquette i and j, where i is the corner where the loop head enters the plaquette.

Diagonal plaquettes On a diagonal plaquette the weight for a vertical move is

$$v = 1 + \left(-\frac{t}{2} - \frac{g}{2} s_j x_j + \frac{-B_j^< - B_j^>}{2} \right) \Delta\tau, \tag{7.10}$$

where $B^>$ and $B^<$ are the only two non-zero bounce-weights. If the plaquette is "antiferromagnetic", a horizontal move can occur, if it is "ferromagnetic" a diagonal move can happen. The associated weights are

$$d = h = \left(\frac{t}{2} + \frac{g}{2} s_i x_i + \mathrm{sign}(s_i) \frac{B_i^< - B_i^>}{2} \right) \Delta\tau. \tag{7.11}$$

From the equation above we see why we called the bounce weights $B^>$ and $B^<$. If $s_i = 1/2$ and $x_i < -\frac{2t}{g}$ the weight would become negative if we would not add $B^<$. If $s_i = -1/2$, a weight $B^>$ has to be added if $x > \frac{2t}{g}$ (fig. 7.3). Thus given a phonon configuration $\{x_i(\tau)\}$ we assign a value to $B_i^<(\tau)$ if x is smaller than some threshold $-\frac{2(t+\varepsilon)}{g}$ and we will set $B_i^>(\tau) = x_i(\tau) - \frac{2(t-\varepsilon)}{g}$ if $x > \frac{2(t-\varepsilon)}{g}$. This is done once after each update of the phonon configuration such that all weights are positive. We store $B_i^{</>}(\tau)$ at all sites and times $t = n\delta\tau$. We will see in a subsequent paragraph why we added the constant value ε.

Off diagonal plaquettes On an off diagonal plaquette only horizontal and diagonal moves can occur.

$$d = h = \left(\frac{t}{2} + \frac{g}{2} s_j x_j + \text{sign}(s_j) \frac{B_j^< - B_j^>}{2} \right) \Delta\tau. \tag{7.12}$$

Note that these are the bounce weights of the exit corner. The bounce weights of the entry corner can be set to zero.

7.2.1.3 The continuum limit

A downside of the path integral formulation in discrete imaginary time is the fact that if $\Delta\tau$ becomes smaller – to decrease the error of the Trotter decomposition – the vertical move becomes more and more probable. Thus even if we make our time grid finer, the number of jumps remains the same. Beard and Wiese [22] have shown, that the continuum limit $\Delta\tau \to 0$ can directly be taken. The constant probability per unit time for a jump corresponds to a Poisson process. So instead of randomly chosing the move of the path on each plaquette, a new time for a diagonal or horizontal jump is drawn out of a Poisson distribution.

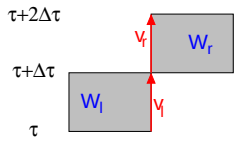

Figure 7.4: The probability that a loop does not jump to another site is $\frac{v_l}{W_l}\frac{v_r}{W_r}$ with plaquette weights W and path weights v.

In our case it is slightly more complicated, since the probability for a vertical move is not constant but a function of $x_i(\tau)$. First consider the probability that a loop goes from time τ to $\tau + 2\Delta\tau$ without jumping to another site (fig. 7.4)

$$P_{straight}(\tau \to \tau + 2\Delta\tau) = \frac{v_l(\tau)}{W_l(\tau)} \frac{v_r(\tau + \Delta\tau)}{W_r(\tau + \Delta\tau)},$$

with left and right path weights $v_{l/r}$ and plaquette weights $W_{r/l}$. Consequently the probability that a loop goes straight up to a time τ' and that one of the processes d or h happens at τ' is

$$P(\tau \to \tau')\Delta\tau = \left(1 - \frac{v_l(\tau')}{W_l(\tau')} + 1 - \frac{v_r(\tau')}{W_r(\tau')} \right) \prod_{t=\tau}^{\tau'} \frac{v_l(t)}{W_l(t)} \frac{v_r(t)}{W_r(t)}. \tag{7.13}$$

To simplify notation we assumed that the two neighbouring plaquettes are at the same time t[4]. Note that v Eq. 7.10 and W Eq. 7.5 are both of the the same form

$$\begin{aligned} W_{l/r}(t) &= 1 + a_{l/r}(t)\Delta\tau \\ v_{l/r}(t) &= 1 + b_{l/r}(t)\Delta\tau. \end{aligned}$$

[4]Since they are only seperated by one time slice this will be ok in the continuum limit.

Plugging this into Eq. 7.13 the limit $\Delta\tau \to 0$ can be taken (the time index is omitted for better readability)

$$\begin{aligned}
\lim_{\Delta\tau\to 0} P(\tau \to \tau')\Delta\tau &= \lim_{\Delta\tau\to 0}\left(\frac{(b_l + b_r - a_l - a_r)\Delta\tau + O(\Delta\tau^2)}{1 + (a_l + a_r)\Delta\tau + O(\Delta\tau^2)}\right) \times \\
&\quad \exp\left(\sum_t \underbrace{\ln(1 + (b_l + b_r)\Delta\tau)}_{\to (b_l+b_r)\Delta\tau} - \underbrace{\ln(1 + (a_l + a_r)\Delta\tau)}_{\to (a_l+a_r)\Delta\tau}\right) \\
&= \underbrace{a_l + a_r - b_l - b_r}_{\lambda(\tau')} \exp\left(-\int_\tau^{\tau'} \underbrace{(a_l + a_r - b_l - b_r)}_{\lambda(t)}\, dt\right) d\tau \\
P(\tau \to \tau')d\tau &= \lambda(\tau') e^{-\int_\tau^{\tau'} \lambda(t)dt} d\tau. \qquad (7.14)
\end{aligned}$$

Instead of a poisson distribution with constant density λ we arrived at a time dependent density. Using the actual form of v eq. (7.10) and W eq. (7.5) we see that

$$\lambda(\tau) = t + g(n_i(\tau) - 1/2)x_i(\tau) + B_i^<(\tau) + B_i^>(\tau). \qquad (7.15)$$

Due to the time dependence of the probability distribution we are faced with another problem. A poisson distribution can easily be sampled because it can be inverted. Here we have to use a different strategy. If we can find some function

$$m(\tau) \geq \lambda(\tau') e^{-\int_\tau^{\tau'} \lambda(t)dt}, \qquad (7.16)$$

that can be sampled efficiently, we can use the rejection method to draw a new time τ aut of the distribution eq. (7.14). A probability distribution with the property Eq. 7.16 can easily be found

$$m(t) = \max_\tau \lambda(\tau) e^{-t \min_\tau(\lambda(\tau))}. \qquad (7.17)$$

From our construction of $B^<$ and $B^>$ (see text above and fig. 7.3) it is obvious that $\min_\tau(\lambda(\tau)) > \varepsilon > 0$, thus $m(t)$ is a decreasing function and can be normalized.[5] Thus we proceed as follows: We draw a time τ out of $m(t)$. We then draw a uniformly distributed random number r out of $[0, m(\tau)]$. If $r < p(\tau)$ we accept the new time. If not, we start again with drawing a time out of $m(t)$ until it is accepted.

The integral over $x_i(\tau)$ is done only once after an update of the phonon configuration, where we calculate and store the field $X_i(\tau) = \int_0^\tau x_i(t)dt$, for imaginary times $\tau = 0, \delta\tau, \ldots \beta$. The computational cost is thus of order $L \times \beta$.

After the phonon update, $X_i(\tau)$, $B_i^{</>}(\tau)$, and $x_i(\tau)$ are stored for each point on the space-time grid. If during the loop update one of these quantities is needed for an arbitrary time $k\delta\tau < \tau < (k+1)\delta\tau$ we apply a linear interpolation between the two time points $k\delta$ and $(k+1)\delta$.

[5] We added ε in order to guarantee that $m(t)$ decreases *strictly* monotonic.

7.2.2 Update of the phonon elongations

The phononic update is performed on the basis of Ref. [11, 12]. In these references the phononic part of the path integral was formulated in a continous version. This results in infinitely many Matsubara frequencies ω_n after a Fourier transformation, and a cutoff in ω_n needs to be introduced. Furthermore, the continous phonons have to be discretized later to do the actual simulations.

Here we already start from time discretized phonon coordinates which lead to a slightly different form of the Fourier transformed frequencies (see below). We need no artificial cutoff frequency, since the number of frequencies is equal to the number of time slices.

The phononic part of the partition sum can readily be written as

$$\begin{aligned} Z_{\{\mathbf{ph}\}} &= \int \mathcal{D}x\, e^{-S_{ph}} = \int \mathcal{D}x \exp\Big(- H_{e-ph} - H_{ph}\Big) \\ &= \int \mathcal{D}x \exp\Big(- \frac{\beta}{N} \sum_{i,\tau} \Big\{ - g x_i(\tau)\big(n_i(\tau) - \frac{1}{2}\big) \\ &\qquad + \frac{p_i(\tau)^2}{2} + \omega_0^2 \frac{x_i(\tau)^2}{2} \Big\}\Big), \end{aligned} \tag{7.18}$$

with the momentum $p_i(\tau) = \left(x_i(\tau) - x_i(\tau - \delta\tau)\right)/\delta\tau$. After a Fourier-transformation of $x_i(\tau) \to \widetilde{x}_{k,n}$ and $n_i(\tau) - 1/2 \to \widetilde{n}_{k,n}$ respectively, $\delta\tau^2 p_i(\tau)^2$ becomes

$$\begin{aligned} \sum_{\tau} \left(x_k(\tau) - x_k(\tau - \delta\tau)\right)^2 &= \sum_{n} \left|1 - e^{2\pi i n/N}\right|^2 |\widetilde{x_{k,n}}|^2 \\ &= 4 \sin^2\left(\frac{\pi n}{N}\right) |\widetilde{x_{k,n}}|^2 \end{aligned} \tag{7.19}$$

and consequently the action reads

$$S_{ph} = \frac{\beta}{2N} \sum_{k}^{1.\ \mathrm{B.Z.}} \sum_{n} -2\, g\, \widetilde{x}_{k,n} \widetilde{n}_{k,n} + \underbrace{\left(\omega_0^2 + \omega_n^2\right)}_{=:\omega_{k,n}} \widetilde{x}_{k,n}^2 \tag{7.20}$$

where we defined $\omega_n = \frac{2N}{\beta} \sin\left(\frac{\pi\, n}{N}\right)$. By completing the square we can easily see that both real and imaginary part of $\{x_{k,n}\}$ can be sampled from a normal distribution with mean μ and variance σ^2

$$\begin{aligned} \mu_{k,n} &= - g \frac{\widetilde{n}_{k,n}}{\omega_{k,n}} \\ \sigma_{k,n}^2 &= \frac{N}{\omega_{k,n}^2 \beta}. \end{aligned} \tag{7.21}$$

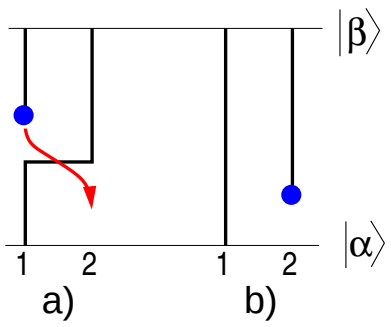

Figure 7.5: During the loop update, a sign change of the propagator can occur (See text for explanation).

We used the hermitian symmetry $\widetilde{x}^*_{k,n} = \widetilde{x}_{-k,-n}$ and $\widetilde{n}^*_{k,n} = \widetilde{n}_{-k,-n}$. Since Eq. (7.20) is biquadratic in $\widetilde{x}_{k,n}$, we always accept our proposal Eq. (7.21).

A generalization to more complex models with dispersion of ω and/or g is simply made by replacing $\omega_0 \to \omega_k$ and $g \to g_k$ respectively.

7.2.3 The fermionic sign problem

Since we simulate fermions, a sign problem occurs in the path integral Monte Carlo simulation. However a negative sign of one specific configuration only occurs if the winding number is odd and the number of fermions is even. If one tunes the parameters such that there is an odd number of fermions in the system and if the temperature is low enough – to prevent density fluctuations – the average sign in a simulation is nearly one.

We perform our simulations at half filling with systems of length L, where $L/2$ is odd. In all of our simulations, the average sign was exactly one.

7.2.4 Measurements of dynamical properties

The phonon spectral function $S_x(k,\omega)$ is obtained by inverting

$$\langle x_{-k,n} x_{k,n} \rangle = \int_{-\infty}^{\infty} \frac{\omega \; S_x(k,\omega)}{\omega^2 + \omega_n^2} d\omega, \tag{7.22}$$

which is done using the maximum entropy method. [26, 27] The correlation function can be written as

$$\langle x_{-k,n} x_{k,n} \rangle = \sigma^2_{k,n} + \mu^2_{k,n}, \tag{7.23}$$

i.e. for a given electron configuration it can be measured exactly in the (k, ω_n)-plane where we already integrated over the phonon degrees of freedom.[6]

Also the dynamic structure factor can easily be evaluated by measuring the density density correlation function and an inversion of the following equation

$$\langle n_{-k}(\tau) n_k(0) \rangle = \int_{-\infty}^{\infty} \frac{S_n(k,\omega) e^{-\tau\omega}}{e^{-\beta\omega}+1} d\omega. \tag{7.24}$$

The same holds for the one particle spectral function

$$\langle c_k(\tau) c^\dagger_{-k}(0) + c^\dagger_k(\tau) c_{-k}(0) \rangle = \int_{-\infty}^{\infty} \frac{A(k,\omega) e^{-\tau\omega}}{e^{-\beta\omega}+1} d\omega. \tag{7.25}$$

Measuring of the correlation function (e.g. $c_k(\tau) c^\dagger_{-k}(0)$) is straight forward during one loop update. Given a loop head at time t_1 and site i and the loop tail at t_2[7] and site j one obtains for the weight of the propagator $w = \langle \alpha | c_i(t_2 - t_1) c^\dagger_j(0) | \beta \rangle = 1$ where $\langle \alpha |$ and $|\beta\rangle$ are the electron configurations prior to the loop update.

As mentioned above, the fermionic sign problem is not relevant for certain system sizes at low temperature. However there is a small complication for the measurement of the propagator. Due to the fermionic nature of the operators c and $c^\dagger$ also the sign of the propagator can change during an update. There are several reasons for a sign change:

(i) In one dimension, two spinless fermions on neighboring sites can not switch its positions – which would result in a sign change. However, during a loop update, in this extended configuration space it is also possible for spinless fermions to change places. This is depicted in Fig. 7.5 (a) and (b). Denoting the weight of the propagator in Fig. 7.5 (a) as $w = \langle \alpha | c_1 c^\dagger_2 c^\dagger_1 | \beta \rangle$ it becomes $w' = \langle \alpha | c^\dagger_2 | \beta \rangle = -w$ after the jump of the loop head to site two in Fig. 7.5 (b).

(ii) If there is an even number of fermions, the sign of the propagator changes when the loop head crosses the boundary.

Although spinless fermions in 1D can be mapped onto the XXZ model via the Jordan-Wigner transformation, this is the reason, why the spectral functions of the XXZ model and of free fermions differ significantly [129].

[6] Note that $\sigma_{k,n}$ and $\mu_{k,n}$ solely depend on the electron configuration.

[7] These times are in practice taken to be on a time grid, with some spacing Δt. This limits the maximum energy that can be resolved $E_{max} \sim 1/\Delta t$. This time grid is independent from the phononic one with spacing $\delta\tau$. Furthermore it does not affect the continous time directed loop algorithm.

7.2.4.1 Exact Moments of the Phonon Spectral Function

The accuracy of the maximum entropy method can be substancially improved, if exact known moments of the spectral function are used as input of the inversion as well [11].

Given the spectral function $S_x(k,\omega)$, the i^{th} moment is given as

$$M_x^{(i)} = \int_{-\infty}^{\infty} S_x(k,\omega)\omega^i d\omega \tag{7.26}$$

One can find an expression of the moment in terms of commutators with the Hamiltonian

$$M_x^{(i)} = \langle [\underbrace{[[[\hat{x}],\hat{H}],\dots\hat{H}]}_{i-j \text{ times}}, \underbrace{[\hat{H}\dots,[\hat{H},[\hat{H},\hat{x}]]]}_{j \text{ times}}] \rangle\,, \qquad 0 \le j \le i. \tag{7.27}$$

Using the canonical commutation relation $[\hat{x}_m,\hat{p}_n] = i\delta_{m,n}$, one can easily calculate $[\hat{H},\hat{x}_n] = -i\hat{p}_n$ and $[\hat{H},\hat{p}_n] = -i\omega_0^2\hat{x}_n$. This leads together with Eq. 7.27 to the first and third moment

$$M_x^{(1)} = 1 \tag{7.28}$$

$$M_x^{(3)} = \omega_0^2, \tag{7.29}$$

respectively. We use that in all results presented below.

In general on obtains $M_x^{(2n+1)} = \omega_0^{2n}$. These moments are not taken into account in the maximum entropy procedure.

7.3 Results

All of the results presented below are simulations of the $L = 66$ sites chain with periodic boundary conditions and an inverse temperature $\beta = 10\,L$. We take 10 β time slices for the phonons. For the measurement of dynamical properties we have to introduce a time grid on which we measure correlation functions. We chose $\Delta t = 0.1$.

As mentioned in many previous works, there are four distinct regions in the phase diagram that show different physics (see Fig. 7.1). The parameter ω_0/t controls the adiabaticity of the system. In the adiabatic regime $\omega_0/t \ll 1$ phonons can be seen as static while in the anti-adiabatic limit $\omega_0/t \gg 1$ the lattice deformation is adjusted instantaneously by the movement of electrons. For weak electron phonon coupling $g^2/t \ll \omega_0$ the system is in a Luttinger liquid (LL) phase with attractive (repulsive) interactions in the adiabatic (anti-adiabatic) regime. Above some critical coupling strength $g_c(\omega_0)$ the model shows a charge density wave (CDW) insulating phase which can either be a band insulator ($\omega_0/t \ll 1$) or a polaronic superlattice ($\omega_0/t \gg 1$), meaning that the electrons are heavily dressed by phonons.

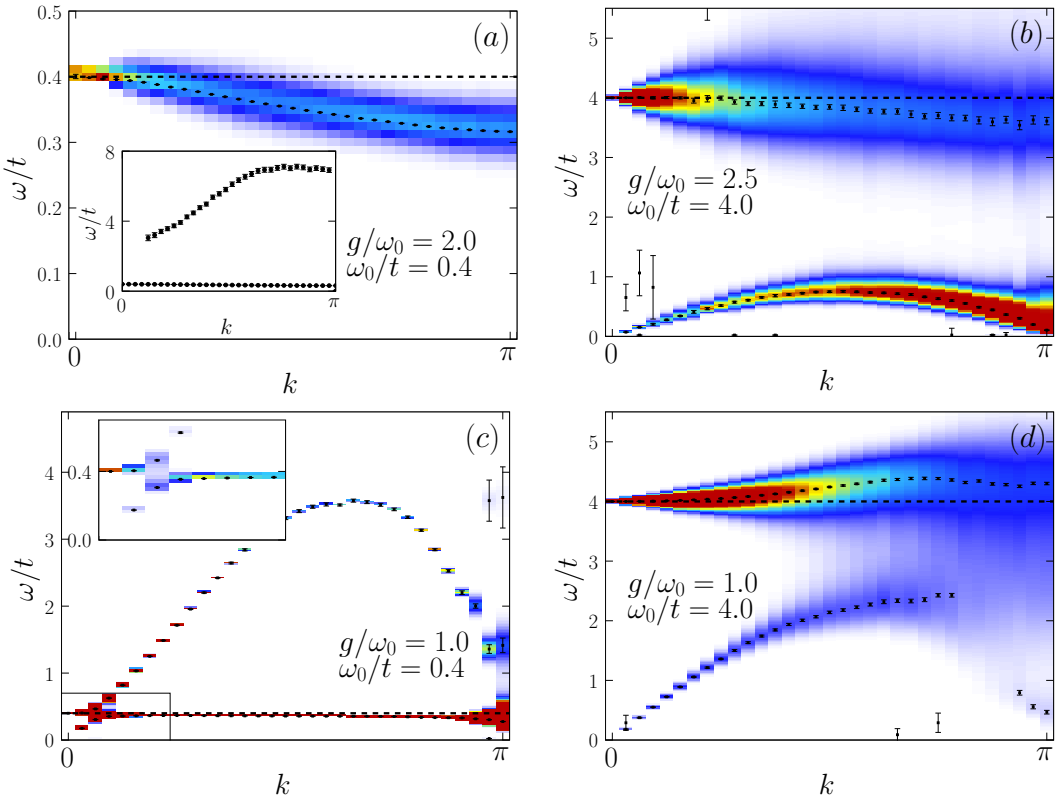

Figure 7.6: Phonon spectral function $S_x(k, \omega)$ in the four distinct regions of the phase diagram. The letters (a)-(d) correspond to the letters (a)-(d) in Fig. 7.1. The black error bars mark the center of the peaks. The dashed line is at $\omega = \omega_0$. The inset in (c) shows that there are indeed two bands splitting at small k. The inset in (a) shows the 100 times less intense excitations at larger energies. An additional weak dispersion-less feature at $\omega/t \sim 8$ is not shown in (b).

In Fig. 7.6, the phonon spectral function $S_x(k, \omega)$ is shown in the four regions discussed above. Our results agree well with previous calculations. [123, 124, 125]

In the articles by Sykora *et al.* [124, 125] and by Hohenadler *et al.* [123] two distinct scenarios for $S_x(k, \omega)$ have been described in the LL regime. While they reported phonon softening in the adiabatic region ($\omega_0/t \ll 1$) they saw a hardening scenario in the anti-adiabatic region ($\omega_0/t \gg 1$). This is in accordance to the $\omega \sim \omega_0$ bands at $k = \pi$ in Fig. 7.6 (c) and (d).

However, we want to point out, that the two scenarios are not that distinct. In both cases there exist two bands (see Fig. 7.6 (c) and (d)). One starting at $k = 0$ at an energy $\omega = \omega_0$ which is, according to Ref.[124, 125], strongly dressed by the free electrons. Thus the phonons are hardened and show the features of a cosine-like free electron dispersion. A second band with linear dispersion for small k is observed

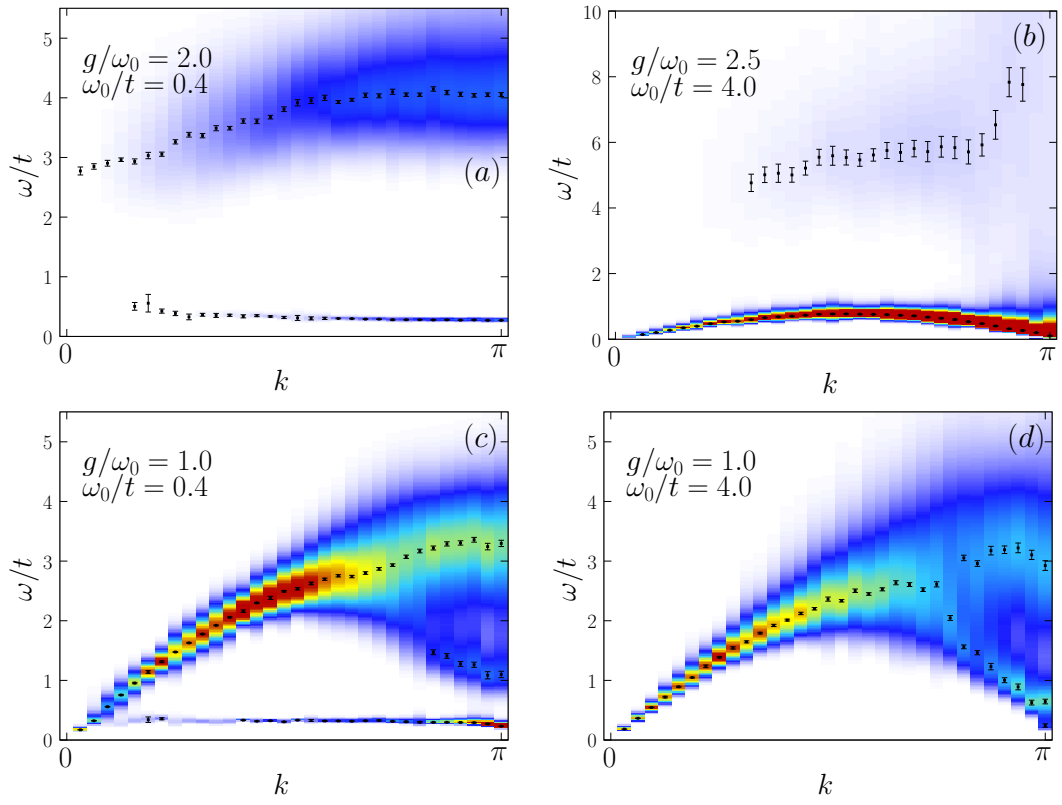

Figure 7.7: Dynamic structure factor $S_n(k,\omega)$ in the same parameter regions as in Fig. 7.6.

in both the adiabatic and the anti-adiabatic regime as well. This is the soft phonon band. We want to point out, that only the weights of the two bands and the amount of softening (hardening) differ in the two regions of small and large ω_0/t – but the situation of two bands, one soft and one hard one, remains the same.

In the CDW insulating phase (Fig. 7.6 (a) and (b)) the situation differs a lot for small and large ω_0. While we observe a gapped mode at $\omega \sim \omega_0$ that is slightly softened in both cases, there is an additional gapped mode at high energy in the band insulating region (Fig. 7.6 (a)) and a gapless mode with sine-like dispersion in the polaronic superlattice (Fig. 7.6 (b)). This low energy excitation in the polaronic superlattice has been observed by Hohenadler *et al.* [123] too. However, due to their small lattice sizes, the sine-like dispersion has not been resolved.

For free fermions the dynamic structure factor $S_n(k,\omega)$ should be equivalent to that of the XXZ model, which displays the magnon continuum between $2t\sin(2k)$ and $4t\sin(k)$. This is also the main behaviour of the Holstein model in the LL phase Fig. 7.7(c) and (d). In addition one can observe excitations exactly at the

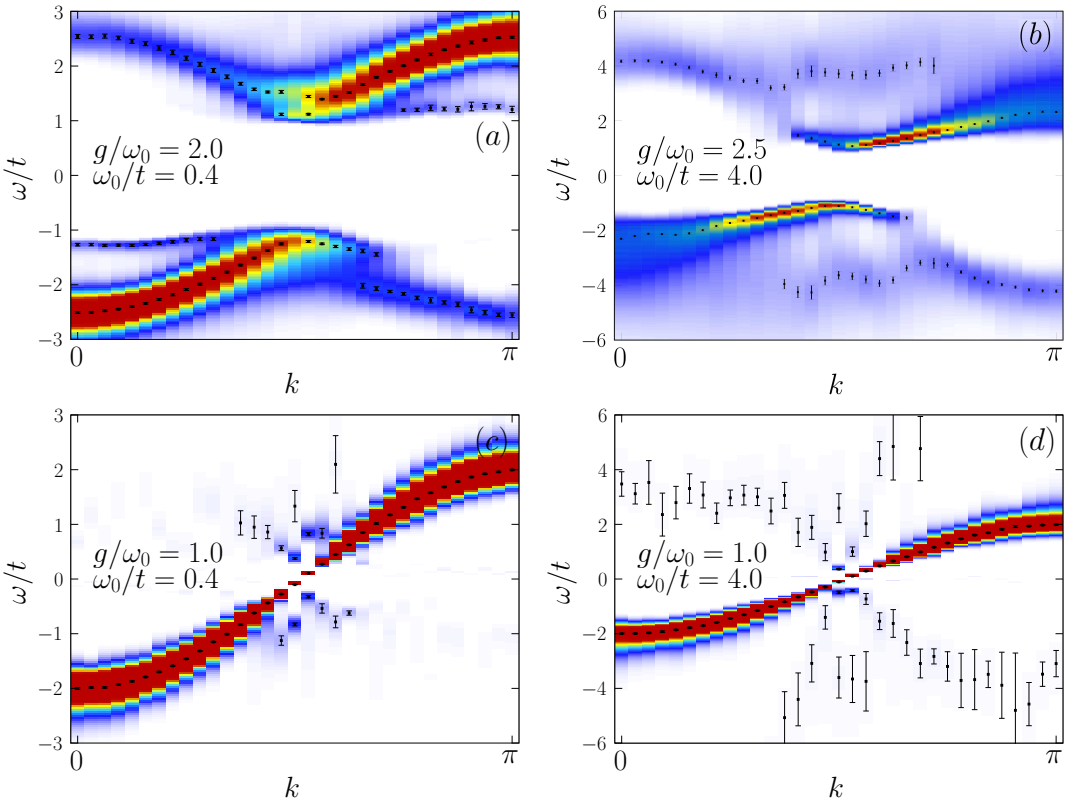

Figure 7.8: One particle spectral function $A(k, \omega)$ in the four distinct physical regions. Free electrons in the LL (c) and (d) and gapped modes in the CDW with (a) and without dispersion (b).

energy of the Einstein phonons at $\omega = \omega_0 = 0.4$ in the adiabatic region.

This is in contrast to the insulating phase, where nearly dispersion-less and gapped modes at $\omega/t \sim 4$ can be seen (see Fig. 7.7(a) and (b)). While in the adiabatic limit, a strong excitation at the bare phonon frequency ω_0 is observed, in the antiadiabatic limit the sine-like dispersion, that has already be seen in the phonon spectra (Fig. 7.6 (b)), is present as well.

In Fig. 7.8 we show our results for the one particle spectral function $A(k, \omega)$. In the LL phase, i.e. for small coupling g/ω_0 we observe the dispersion of free electrons with only small precursors of a gap both in the adiabatic and in the antiadiabatic limit, see Fig. 7.8(c), and (d).

In the insulating phase one can distinguish the band insulator Fig. 7.8(a) with gapped but dispersive excitations from the so called polaronic superlattice, where non dispersive bands at multiples of $\omega = 2t$ occur, see Fig. 7.8(d).

7.4 Conclusions

We presented an efficient method to study electron phonon models by means of Quantum Monte Carlo. We benchmarked our approach to calculate dynamical properties of the half filled Holstein model of spinless fermions. Results from previous calculations [123, 124, 125] for single particle spectra are confirmed and we presented the dynamic structure factor $S(k, \omega)$ for the first time in the four distinct physical regions of the Holstein model.

Furthermore we note that the method is applicable to more complicated models that include dispersive phonons $\omega(k)$ and electron–phonon coupling $g(k)$.

8 Overall Conclusions

This thesis consists of two major parts. In the first part, experimental realizations of strongly correlated systems are investigated by means of very well established QMC methods. In particular, the Bose-Hubbard model describing gases of cold atoms in optical lattices and a polariton model that can be realized in terms of arrays of coupled cavities, is studied.

The directed loop algorithm in the SSE representation, together with a mapping to continuous time and the Maximum Entropy method is applied to obtain spectral properties.

Unbiased results for the one-particle spectral function and the dynamic structure factor for the one– and two–dimensional Bose–Hubbard model are presented. These quantities are accessible in experiment from Bragg spectroscopy – allowing to measure excitations with high energy and momentum resolution.

QMC data is compared to analytical results, that are usually taken to fit experimental data. In the atomic limit (t/U small), the one-particle spectral function shows a gapped spectrum and can be described very well by simple mean field approaches. Both the spectral weight and the associated energies compare well to the unbiased results. The dynamic structure factor has a gapped mode at energy $\sim U$ and an associated weight proportional to $\sin^2(k/2)$, which has previously been predicted by perturbation theory calculations.

Close to the Mott insulator to superfluid phase transition, mean field calculations become quantitatively wrong. This is not unexpected, since it is known that mean field approaches underestimate the size of the Mott lobe, resulting in wrong phase boundaries.

In one dimension, in the superfluid region linear Goldstone modes are observed. Bogoliubov theory gives qualitatively right results. However on the quantitative level it fails close to the phase transition and is thus not appropriate to describe experimental data.

In two dimensions the QMC data is consistent with RPA and strong coupling theory, while there are large discrepancies when comparing to Bogoliubov theory. In addition to the linear modes, also gapped modes are predicted from RPA and strong coupling theory. Due to the small spectral weight of the gapped modes at $k \sim 0$ we can not resolve these additional modes with our method.

Furthermore, the finite temperature behavior in the two dimensional case is inves-

tigated. This is important, since temperature effects may be relevant in experiments since both the lattice lasers as well as the Bragg lasers heat the condensate significantly. Furthermore most analytic approaches work at zero temperature and may not be accurate in the general case.

The dynamic structure factor shows the most severe dependence on temperature. While in the Mott phase the relevant energy scale for the excitation is $\sim U$ in the high temperature normal fluid phase it is governed by t/U which is very small. Thus, although the Mott insulator only exists at $T = 0$ one can clearly distinguish the Mott like physics at low temperature from the high temperature normal fluid phase.

In the superfluid region, there is a phase transition to a normal fluid phase. In the one particle spectrum this can be observed by a transition from linear modes to quadratic modes. The dispersion of the dynamic structure factor shows only little dependence on temperature. However, above the critical temperature there is a severe broadening of the peaks which might aid the determination of temperature in experiments.

The so called Jaynes–Cummings–Hubbard model describes the polaronic nature of light modes in coupled cavities that couple to two-level systems. Interestingly, although there is no interaction term present in the Hamiltonian, the physics is very similar to that of the Bose–Hubbard model. Again excitation spectra are calculated, which have in general the same properties as those of the Bose–Hubbard model. However due to the polaronic nature of the excitations, additional bands with very small spectral weight occur. Furthermore, the possibility of detuning of the laser fields lead to richer physics.

The Mott insulator to superfluid phase transition is investigated in more detail. From a finite size scaling the dynamical critical exponent $z = 2$ is obtained, leading to the conclusion that the generic phase transition (i.e. away from the lobe tip) is of the same nature as that of the Bose–Hubbard model. Another similarity can be seen at the KT transition (that is the transition at constant polariton density $n_p = 1$), where an emergent particle hole symmetry is demonstrated on approach of the tip of the lobe.

In the second part of the thesis, existing QMC methods are extended to be applicable to electron–phonon models. The main idea of using global cluster updates for the electrons and an update in Fourier space for the phonons has already been used previously to study spin-Peierls transitions [11, 12]. In that approach the SSE representation has been used for the electronic part of the partition sum. This is however not the optimal choice for Hamiltonians that are dominated by off-diagonal terms.

Here a slightly different approach is used, formulating the electronic update in a continuous time path integral representation. To benchmark the method it is applied to the well known Holstein model of spinless fermions in one dimension. It proves to be an efficient method to obtain unbiased results, including correlation functions and

spectral properties.

Furthermore this method can be applied to more complicated models including dispersive phonons ω_k and electron-phonon couplings g_k without any algorithmic complications.

Part IV

Appendices

A Error Propagation by Jackknife and Fourier Transformation

Some Greens's function $g_r(\tau)$[1] is measured within some uncertainty $g_r = \bar{g}_r \pm \Delta g_r$[2]. $\bar{g}_r$ is the estimator for the mean of g_r and Δg_r is the statistical error (e.g. the estimator for the square root of the variance). Our aim is to fourier transform g_r. Thus a correct error propagation should be applied.

We want to know the error of the Fourier transformed values

$$G_k = \sum_r e^{ikr} g_r \equiv f_k(\mathbf{g})$$

where we defined the vector $\mathbf{g} = (g_1, g_2, \dots g_N)$ and the linear function f.

Let us assume that the measurements are uncorrelated, then a linear approximation for the combined standard uncertainty ΔG_k of the measurement result G_k is given by

$$(\Delta G_k)^2 = \sum_j \left(\frac{\partial f_k(\mathbf{g})}{\partial g_j} \right)^2 (\Delta g_j)^2. \tag{A.1}$$

Since $\frac{\partial f_k(\mathbf{g})}{\partial g_j}$ is simply e^{ikj} we have

$$(\Delta G_k)^2 = \sum_j e^{2ikj} (\Delta g_j)^2 \tag{A.2}$$

This is however only true if the measurements are uncorrelated, which is not the case here. A correct treatment of the correlations can be done by including all covariances with is very cumbersome.

A.1 The Jackknife method

An alternative approach is the so called Jackknife method, which is a systematic way of obtaining error estimates for a set of stochastic measurements. Within this so called *resampling* method, the original data is split into blocks of length M (to avoid auto-correlation effects, one choses $M \gg \tau$). Then, for each block $m = 1 \dots M$, expectation values $\langle O \rangle_m$ are calculated by using all data *except* the m-th block.

[1] E.g. the $\langle a(\tau) a^\dagger(0) \rangle$ Green's function.

[2] we drop the time dependence τ for better readability.

An error estimate of one observable can be calculated as

$$\Delta \langle O \rangle = \sqrt{\frac{M-1}{M} \sum_{m=1}^{M} [\langle O \rangle_m - \langle O \rangle]^2}, \tag{A.3}$$

where $\langle O \rangle$ is the expectation value, calculated with all of the data. The error estimate for functions of observables $f(\langle O \rangle)$ are easily evaluated with

$$\Delta f = \sqrt{\frac{M-1}{M} \sum_{m=1}^{M} [f(\langle O \rangle)_m - f(\langle O \rangle)]^2}. \tag{A.4}$$

Note that Jacknife is robust, even when f is nonlinear, and/or when the data is correlated.

Since Jackknife is already part of ALPS, it is easy to implement a Fourier transformation of a vector of `RealObsEvaluator`'s

A.2 Details of the Implementation

First, I defined different types of the Fourier transformation (FT) in analogy to the fftw3 package:

```
enum fftw3_TYPE { REDFT00,REDFT10,REDFT01,REDFT11,
                  ERROR00 };
```

The definitions for `REDFTXX` can be found in the fftw3 documentation. `ERROR00` is the same as REDFT00, but with $k \to 2k$ to evaluate Eq. (A.2).

The FT–class is templated with some double type T wich can also be a `RealObsEvaluator`. The constructor takes the size of the input array and the type of the FT. The matrix elements of $\texttt{kernel}_{-k,j}$ are $exp(ikj)$, or a variant of it, depending on the fftw3_TYPE.

```
template<class T>
class FourierTransform
{
public:
  typedef T double_type;
  typedef boost::numeric::ublas::vector<double_type>
                                                  vector;
  typedef boost::numeric::ublas::matrix<double> matrix;

  FourierTransform(int L = 2,
```

```
                    fftw3_TYPE fftw_type = REDFT00);
  vector transform(const vector & in)
  {
    if ( in.size() != size_ )
      boost::throw_exception(
                    std::runtime_error("..."));
    return norm_*my_prod<double_type>(kernel_,in);
  }
  void resize(int L)
private:
  fftw3_TYPE fftw_type_;
  uint size_;
  double norm_;
  matrix kernel_;
};
```

Unfortunately, the boost matrix–vector product does not work with `RealObsEvaluator`. Thus I implemented the product in a straight forward way:

```
template<class T>
boost::numeric::ublas::vector<T>
my_prod(const boost::numeric::ublas::matrix<double> & m,
        const boost::numeric::ublas::vector<T> & v)
    // Straight forward matrix vector product.
{
  boost::numeric::ublas::vector<T> result(v);
  for (uint r = 0 ; r < v.size() ; r++)
    result[r] *= 0.0; // to get the same number of runs
                      // necessary for +=
  for (uint k = 0 ; k < m.size1() ; k++)
    for (uint r = 0 ; r < m.size2() ; r++)
      result(k) += m(k,r)*v(r);
  return result;
}
```

From a user point of view, the only thing that needs to be done is storing the observables in a boost vector

```
boost::numeric::ublas::vector<RealObsEvaluator> in(size),out(size);
```

defining a FT

```
FourierTransform<RealObsEvaluator> ft(size,REDFT00);,
```

and performing the FT

```
out = ft.transform(in);
```

One can easily access the mean and the error of the element i of the vector with `out(i).mean()`, `out(i).error()`, or with `out(i).variance()`.

B Extensions to the ALPS `dirloop_sse` program

In this appendix a few extensions to the ALPS `dirloop_sse` program, which implements directed loops in the SSE representation, are presented. In particular the measurement of dynamical correlation functions are explained.

All of the extensions are made to the ALPS version 1.3.4.

B.1 "Canonical" Monte Carlo

Although the QMC algorithm always works in the grand canonical ensemble, one can easily get a canonical algorithm, by just selecting measurements with some specific value of some quantum number. One can e.g. evaluate only those measurements with an average particle number of $n = 1$.

Therefor, the parameters

```
CANONICAL=true
CONSTRAINT="n"
CONSTRAINT_VALUE=1
```

have to be set in the input file. One can use any diagonal operator that is defined in the model (`"n"`,`"Sz"`, ...).

In the output file, the observable `counts` gives the average number of updates that are done, until a measurement is performed.

This has been used to study the fixed density KT tranistion in the Bose Hubbard model.

B.2 Correlation functions

In the ALPS-input file, the following settings invoke a measurement of dynamical Green's functions

```
MEASURE[Dynamic_Green]=true
MEASURE[Dynamic_SzSz]=true
GREENS_FUNCTION_DISCRETISATION=300
correlation file="file_to_store_correlation_function"
```

The first line invokes a measurement if $\langle a_i(\tau)a_j^\dagger(0)\rangle$ (or $\langle S_i^-(\tau)S_j^+(0)\rangle$ for spin models), while the second one does $FT(\langle n(\tau)n(0)\rangle) = \langle|\widetilde{n}_{k,\omega}|^2\rangle$ (or the same for S^z for spin models).

`GREENS_FUNCTION_DISCRETISATION` is the number N of time slices for the correlation function measurement. Thus $\Delta\tau = \beta/N$ is the time difference between to time slices and $\sim 1/\Delta\tau$ is the maximal energy that can be resolved.

Note, that the correlations are not stored in the usual way. The output is not seen in the `*.out.xml` file because of the large amount of data. The correlation functions are only stored in the `correlation file` in binary format.

The data can only be extracted with the `evaluate_greens` program.

B.2.1 Additional Measurements

The static structure factor

$$S_O(k) = \langle O_{-k}O_k\rangle$$

is already implemented in ALPS, where the operator O is either the density n or the S^z operator for spin models. It can be used by setting

```
MEASURE[ Structure Factor]=true
```

I added the Suzeptibility

$$\chi_O(k) = \int_0^\beta d\tau\, \langle O_{-k}(\tau)O_k(0)\rangle\,.$$

See `SSE.Measurements.cpp` for details of the implementation.

```
MEASURE[ Susceptibility]=true
```

The name of the observabele in the `*.out.xml` file is `Density Susceptibility` or `Spin Susceptibility` depending on the model.

If the standard ALPS parameter

```
MEASURE[ Local Density] = true
```

is set, not only the local density $\langle n_i\rangle$ (or $\langle S_i^z\rangle$) is stored under the name `Local Density` but also $\langle n_i^2\rangle$ is stored (`Local Density`$\hat{\mathbf{2}}$).

B.3 Technical Details

B.3.1 Mapping to continuous time

To each element of the operator string, a time τ_i is attached. These M times are randomly chosen in the interval $[0, \beta]$ from a uniform distribution. Note that in the

SSE program all times are between $[0, 1]$ in some cases this has to be taken into account. To sample the times, I take the cumulative sum of $M + 1$ exponentially distributed numbers and divide it with the last number. This is *much* faster than sorting M uniformly distributed numbers.

The variable

```
std::vector<double> tau;
```

stores the times of the vertices.

B.3.2 Implementation of Green's function measurements

The `Greens` class stores the value of the Green's function on a discrete space–time grid. The first index of `std::vector<std::valarray<double> > greens_;` is the site index, the second one the (discrete) time index.

```
class Greens
{
public:
  Greens(int L = 1,int nTau = 1) :
    L_(L),nTau_(nTau),worm_counter_(0)
  virtual ~Greens(){}
  void setWeight(double w){weight_ = w;};
  void startNewWorm()
    {  worm_counter_++;  }
  void add(const int &l,
           const time_struct& t1,const time_struct& t2,
           bool up);
  void add_trivial_loop(const int & s);
  void add_zero_zero(double weight00,int zero_site = 0);
  std::valarray<double> getTimeSlice(int t) const
  { return greens_[t]/(worm_counter_*1.0); }
protected:
  std::vector<std::valarray<double> > greens_;
  double weight_;
  int L_,nTau_;       // size of discretized space and time
  int worm_counter_;
};
```

Additionally, operators = and + are defined, as well as the operators >> and << for input and output to an ALPS dump.

```
public:
```

```
Greens& operator=(const Greens & other);
friend Greens operator+(const Greens &g1,const Greens &g2);
friend std::ostream& operator<<(std::ostream&, const Greens&);
friend alps::ODump& operator<<(alps::ODump&, const Greens&);
friend alps::IDump& operator>>(alps::IDump&, Greens&);
```

In the program it is very simple to use this class. First, initialize an instance of greens. Resizing can be done afterwards.

```
Greens green1();
Greens green2(100,134); //100 sites and 134 time slices
green1.resize(50,12)
```

During the loop – update one can add some weight along the path of the worm. In the following example the loop has a weight of 0.5 and is added from t_1 in upward direction if direction is `true` until t_2 at site `s`.

```
green2.setWeight(0.5);
green2.startNewWorm();
during the loop update:
   time_struct t1(time1);
   time_struct t2(time2);
   bool direction = true;// true ... move up,
                         // false ... move down in time
   green2.add(s,t1,t2,direction)
```

Measurements within the ALPS framework can be done as follows. First, a `RealVectorObservable` has to be added to the `ObservableSet measurements`

```
ObservableSet measurements;
measurements << alps::make_observable(
                alps::RealVectorObservable("Greens function"),
                is_signed_);
```

Later, after the Greens function has been measured, one can add it to the ObservableSet. If you want to measure the equal time greens function,

```
std::valarray<double> g = green2.getTimeSlice(0);
measurements["Greens function"] << g;
green2.reset(); // reset all values to zero
```

After the simulation finished, the data can be stored into a file:

```
std::string name = "green.data";
OXDRFileDump dump(name.c_str());
```

```
dump << correlations_;
```

In some cases, e.g. for the $\langle S^z(\tau)S^z(0)\rangle$ correlation function, it is convenient to perform a Fourier Transformation (FT) in space and time. The values of $\langle S_i^z(\tau)\rangle$ are stored, then a FT is applied to obtain $\widetilde{S}_{k,\omega} = FT(S_i^z(\tau))$. In Fourier space, the convolution is a product, and the correlation function can easily be measured $FT(\langle S^z(\tau)S^z(0)\rangle) = \langle|\widetilde{S}_{k,\omega}^z|^2\rangle$.

To use this fact, the class `FFTGreens` is derived from `Greens`.

```
class FFTGreens : public Greens
{
public:
  FFTGreens(int L = 2,int nTau = 8);
  FFTGreens(const FFTGreens & other);
  void transform();
  std::valarray<double> get_w_slice(int);
  std::valarray<double> get_k_of_w(int);
  std::valarray<double> get_k_of_tau(int);
  void resize(int L,int nTau);
  FFTGreens& operator=(const FFTGreens & other);
  void operator+=(const FFTGreens &other);
  friend FFTGreens operator+(const FFTGreens &g1,
                             const FFTGreens &g2);
private:
  std::vector<std::valarray<double> > fft_greens_;
};
```

One can choose between $g_\omega(k)$, $g_k(\omega)$ and ,$g_k(\tau)$ where the variable in brackets is the index in the `valarray<double>` that is returned from the functions `get_w_slice(int)`, `get_k_of_w(int)`, or `get_k_of_tau(int)` respectively.

As a non trivial example, I show how to measure the polariton density–density correlation function. First record all $S_i^z(\tau)$ values for both site types (Atoms live on sites with site type 1 and photons have site type 0). Since the operators + = are defined, it can be calculated as follows:

```
FFTGreens szsz0, // sz on site_type 0
          szsz1; // sz on site_type 1
for loop over sites s:
   szsz0.add(s,...) // record Sz values

FFTGreens polariton;
polariton  = szsz0;  // do this in two steps to
```

```
polariton += szsz1;  // avoid fft_init()
polariton.transform();
std::valarray<double> g = polariton.get_k_of_tau(3);
measurements["Greens function at k = 3"] << g;
```

Helper classes To apply the periodic boundary conditions in continuous time I used the very convenient class `time_struct` from the worms code of the ALPS library. This is a double variable which is defined on the interval $[0, 1]$. The operators $+$, $-$ and $=$ and a conversion to double operator `double()` are available. The operators $+$, and $-$ care for the pbc. Since the Green's functions are measured on time grid I also wrote a small helper class `discrete_time_struct` which is an integer with periodic boundary conditions.

B.3.3 Problems with the SSE ALPS program

Special care has to be taken for the measurement of $\langle a_i(0)a_i^\dagger(0)\rangle$. I drop the time and site indices for better readability, then $\langle aa^\dagger\rangle = \langle n\rangle + \langle [a, a^\dagger]\rangle$. For bosons, $[a, a^\dagger]$ would be 1. On a computer, we have to limit our self to hardcore bosons with some maximum quantum number N_{max} and the commutation relation reads

$$[a, a^\dagger] = \begin{cases} -n & \text{if } n = N_{max} \\ 1 & \text{otherwise} \end{cases}$$

To include this behaviour, the function `add_zero_zero(weight,distance)` has been added to the `Greens` class. It allows to manually add some weight to the correlation function at zero distance in imaginary time.

The default value for `distance=0`. The distance between two sites is calculated in ALPS with the function `distance(i,j)`. On a lattice with more than one sitetype `distance(i,i)` may give different results depending on the sitetype of `i`. E.g. in the Jaynes–Cummings–Hubbard one has to distinguish whether the loop starts on sitetype 0 (photonic site) or 1 (atomic site). If `siteype(i)=0`, then `distance(i,i) = 0`. If `siteype(i)=1`, then `distance(i,i)` may give some result not equal to zero.

Thus, `add_zero_zero(weight,distance(s,s))` should be used with the ALPS internal distance function where `s` is the site where the loop starts.

B.3.3.1 Start of the loop update

The right way to start the loop update, is to randomly choose a point in the space–time plane (i, τ). In the original program a vertex has been chosen randomly which is ok as long as the Green's function is not going to be measured. Assume we want to start our at some point S in the (i, τ)-plane (see Fig. B.1). We chose the direction of the

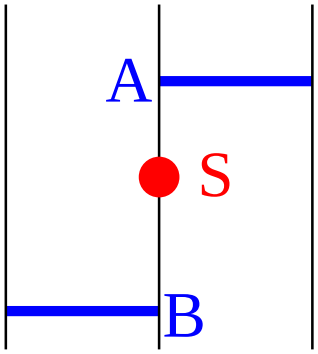

Figure B.1: Part of an SSE configuration with two operators (blue). S marks the starting point of the loop if we used a worldline representation. A and B are the vertices where an SSE loop may start.

loop stochastically and search for the vertex which is closest to S in that direction. If we went upwards we would use A as our starting vertex. Thus we have to add the measurement of the propagator for the distance $S - A$ prior to the start of the loop. When the loop closes, we have to check whether the loop head comes from somewhere above A or from vertex B. If the loop closes from somewhere above we have to add the propagator on the line $A - S$. If it closes from B we have to subtract along $A - S$.

C Fit to Bogoliubov Theory

In this appendix we want to point out some issues with a simple maximum likelihood fit of spectral data to Bogoliubov theory. Since there are too many parameters in the fit, there is not one minimum in the least squares procedure but a broad distribution of possible parameters that are consistent with the data.

In particular we want to show, that a simple fit of the data in Fig. 5.8 (a) to Bogoliubuv theory should always be taken with care. We replotted the maxima of the spectral function in Fig. C.1 (black diamonds). Let us call the maxima of the peaks (our data) $D_{\mathbf{k}} \pm \sigma_{\mathbf{k}}$.

We want to fit the peak maxima to Bogoliubov theory, which predicts excitations at energies

$$E^B_{\mathbf{k}}(n, t/U) = \pm 1/U \sqrt{K_{\mathbf{k}}(2\,n\,U + K_{\mathbf{k}})} \tag{C.1}$$

with

$$K_{\mathbf{k}} = 4\,t\,(\sin(k_x/2)^2 + \sin(k_y/2)^2).$$

(The $1/U$ stems from the fact that we usually measure $E^B_{\mathbf{k}}$ in units of U)

Performing a simple least squares fit one wants to maximize the likelihood function

$$R(n, t/U) = \frac{1}{Z} \exp\left\{ -\frac{(D_{\mathbf{k}} - E_{\mathbf{k}}(n, t/U))^2}{2\sigma^2_{\mathbf{k}}} \right\}. \tag{C.2}$$

Since we are only interested in the maximum we can neglect the normalization factor Z.

In Fig. C.1 we show the function $E_{\mathbf{k}}(n, t/U)$ for the maximum of the $R(n, t/U)$ in the space $(n, t/U)$. Looking only at the figure one could be perfectly satisfied. However, much more important than the maximum of R is the actual shape, which is plotted in Fig. C.2. If R was just of Gaussian form – i.e. one peak that drops exponentially with the distance from the center of the peak – one could indeed take just the maximum of R. In our case we see a narrow region of large R. Thus if we keep one parameter fixed, say t/U which is usually known from the experimental setup, we can find a fairly good approximation to our data varying only n.

To be precise, the parameters of our simulation are $t/U = 0.1$ and $n = 1$, while the best fit to Bogoliubov theory gives $t/U_{bog} = 0.042$ and $n_{bog} = 2.09$.

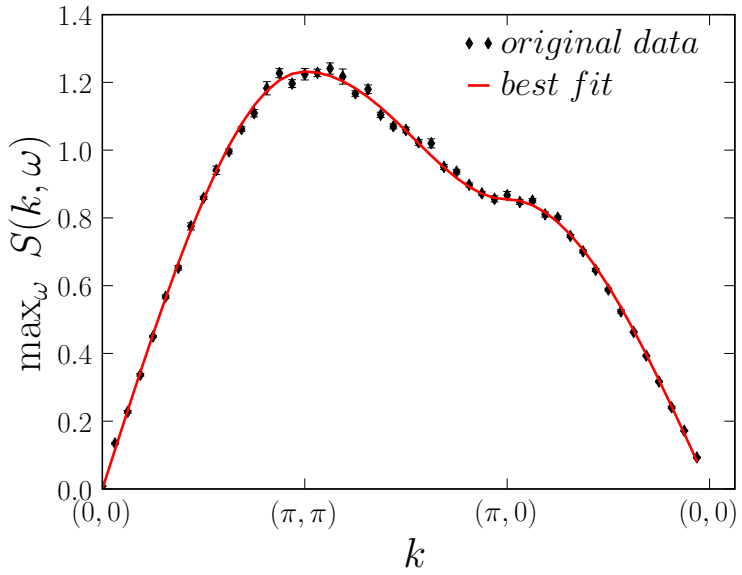

Figure C.1: Original data and best maximum likelihood (least squares) fit. Data is taken from Fig. 5.8 (a). Original data $D_{\mathbf{k}} \pm \sigma_{\mathbf{k}}$ and best fit $E^B_{\mathbf{k}}(n, t/U)$.

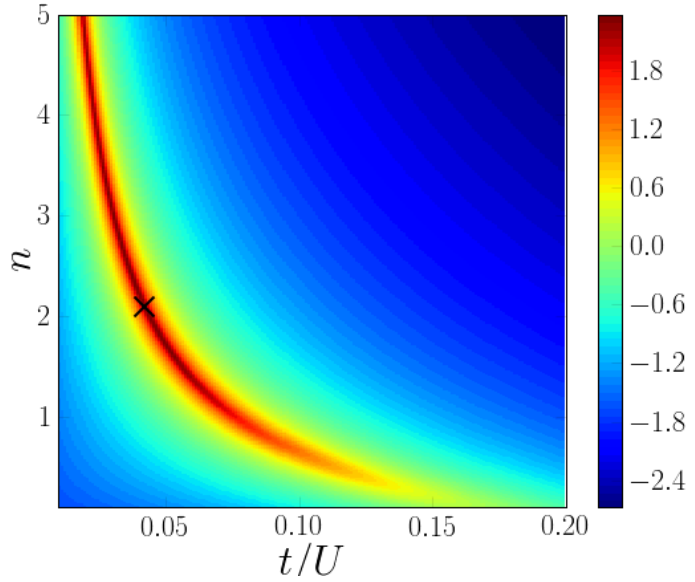

Figure C.2: Logarithm of the likelihood obtained from the data in Fig. 5.8 and Fig. C.1. The cross marks the maximum of the likeli-hood.

This is a problem, which occurs when experimental data is fitted to Bogoliubov theory. As long as the dispersion is "Bogoliubov-like", one can *always* find a good approximation to Bogoliubov theory – although with renormalized parameters. Thus, given only one experimental parameter, one can not deduce the other parameter from a maximum likelihood fit to Bogoliubov theory.

D The Tower of Babel: Conventions for the Holstein model

The Holstein model of spinless fermions has been studied intensively for more than 50 years. Unfortunately there are nearly as many definitions of the parameters of the model as there are papers on it. In this appendix I want to summarize some of the different definitions.

In all of the works considered the electron hopping parameter is called t and the bare phonon Hamiltonian is $\omega_0 \sum_i b_i^\dagger b_i$ plus some constant terms that only shift the energy.

(i) The most commonly used version of the electron phonon coupling is

$$H_{e,ph} = g_I \sum_i (b_i^\dagger + b_i) n_i \tag{D.1}$$

This has been used by Sykora *et al.*, [130, 124, 125], in the QMC paper by McKenzie *et al.*,[115], in the DMRG work by Bursill *et al.*. [120], in Jeckelmann *et al.* [131, 121] where $g_{II} = \gamma$ (in Ref. [121] they use the additional parameter α which is g_{III}, see below),

In Ref. [115] a dimensionless parameter $\lambda = \frac{g_I^2}{\pi t \omega}$ has been defined which is similar to that discussed in (ii) up to a constant factor $\pi/2$.

The definition above is also used within this work.

(ii) The alternative definition

$$H_{e,ph} = \sqrt{\varepsilon_p \omega_0} \sum_i (b_i^\dagger + b_i) n_i \tag{D.2}$$

has been used in works from Fehske *et al.* [122, 132, 133] and by Hohenadler *et al.* [123].

In these works, the dimensionless parameters $\alpha = \omega_0/t$ (the adiabaticity parameter), $g_{II} = \sqrt{\varepsilon_p/\omega_0}$, and $\lambda = \varepsilon_p/2t$ have been introduced to characterise the adiabatic ($\alpha \ll 1$), the anti-adiabatic ($\alpha \gg 1$), the strong coupling ($\lambda \gg 1$), and weak coupling ($\lambda \ll 1$) regimes.

With these definitions Eq. D.2 reads

$$H_{e,ph} = g_{II}\omega_0 \sum_i (b_i^\dagger + b_i) n_i, \tag{D.3}$$

which can be found in Jeckelmann and White [134], in the works of Fehske and coworkers [135, 136], in Loos *et al.* [137],

(iii) Furthermore, the definition

$$H_{e,ph} = g_{III} \sum_i x_i n_i \tag{D.4}$$

can be found in Jeckelmann and White. [121] ($g_{III} = \alpha$), in the work of Hirsch and Frandkin [117] ($g_{III} = \lambda$) and in Creffield *et al.* [126].

(iv) Mona Berciu [138] studied the polaron problem and defined the Holstein model as

$$H_{e,ph} = \frac{g}{\sqrt{N}} \sum_{k,q} c_{k-q}^\dagger c_k (b_q^\dagger + b_{-q}), \tag{D.5}$$

which is the same as in (i) appart from factors proportional to N due to the Fourier transformation of $c_i \to c_k$.

One could in principle change from definition (i) to (iii) easily, by using the phonon elongation instead of creation and anihilation operators $x_i = \frac{1}{\sqrt{2\omega_0}}(b_i^\dagger + b_i)$. In many works however, the phonon elongation has been defined as $x_i = b_i^\dagger + b_i$, redefining the units of the phonon elongation. [131, 120, 123]

Acknowledgments

First of all I would like to thank my advisor Hans Gerd Evertz, who gave me the opportunity to work in a challenging and active field. There where many fruit-full discussions that helped me in understanding the subtleties of QMC as well as the underlying physics.

I am grateful to Franz Michel who's ideas and code I was allowed to use to study the Holstein model and to Martin Hohenadler for pointing me to the direction of the interesting field of correlated light.

Furthermore I would like to thank all my friends and colleagues, in particular Heinz Georg Flesch, Anna Fulterer, Ralf Gamillscheg, Martin Ganahl, Jorge Cham, Michael Knap, Armin Moser and Christian Scheiber for making this time as enjoyable as it has been.

Special thanks goes to my family without whom I would not have had the opportunity to make my own mistakes and last but not least I would like to thank my girlfriend Kathrin for her ongoing love and support.

I acknowledge financial support from NAWI Graz and from FWF Projects No. P18551 and No. P18505.

Bibliography

[1] M. Greiner, O. Mandel, T. Esslinger, T. W. Hänsch, and I. Bloch, Nature **415**, 39 (2002). 3, 17, 19, 56

[2] I. Bloch, J. Dalibard, and W. Zwerger, Rev. Mod. Phys. **80**, 885 (2008). 3, 17, 19, 56

[3] D. Clement, N. Fabbri, L. Fallani, C. Fort, and M. Inguscio, Phys. Rev. Lett. **102**, 155301 (2009). 3, 19, 56, 67, 68, 69

[4] P. T. Ernst *et al.*, Nat Phys **6**, 56 (2010). 3, 19, 56, 67

[5] M. Hartmann, F. Brandao, and M. Plenio, Laser & Photonics Review **2**, 527 (2008). 3, 19, 21, 24, 26, 27

[6] P. Pippan, H. G. Evertz, and M. Hohenadler, Phys. Rev. A **80**, 033612 (2009). 3, 23, 57, 59

[7] N. Kawashima and K. Harada, J. Phys. Soc. Jpn. **73**, 1379 (2004). 5

[8] M. Troyer, F. Alet, S. Trebst, and S. Wessel, physics/0306128 (2003), AIP Conf. Proc. 690, 156 (2003). 5

[9] H. G. Evertz, Advances In Physics **52**, 1 (2003). 5, 11

[10] A. W. Sandvik, R. R. P. Singh, and D. K. Campbell, Phys. Rev. B **56**, 14510 (1997). 6, 10, 27

[11] F. Michel and H. Evertz, 0705.0799 (2007). 6, 10, 82, 88, 91, 98

[12] F. Michel, *Quantum Monte Carlo Simulations for Spin and Spin-phonon Systems*, PhD thesis, TU Graz, 2007. 6, 10, 82, 88, 98

[13] M. Suzuki, Commun. Math. Phys. **51**, 183 (1976). 6

[14] H. F. Trotter, Proc. Am. Math. Soc. **10**, 545 (1959). 6

[15] A. Sandvik and J. Kurkijärvi, Phys. Rev. B **43**, 5950 (1991). 7, 27, 58

[16] D. Handscomb, Proc. Cambridge Philos. **58**, 594 (1962). 7

[17] D. Handscomb, Proc. Cambridge Philos. **60**, 115 (1964). 7

[18] A. W. Sandvik, Journal of Physics A: Mathematical and General **25**, 3667 (1992). 9

[19] A. Dorneich and M. Troyer, Phys. Rev. E **64**, 066701 (2001). 9, 27

[20] N. V. Prokof'ev, B. V. Svistunov, and I. S. Tupitsyn, Pis'ma v Zh.Eks.Teor.Fiz., **64(12)**, 853 (1996), cond-mat/9612091. 10

[21] H. G. Evertz, G. Lana, and M. Marcu, Physical Review Letters **70**, 875 (1993). 11, 27, 58

[22] B. B. Beard and U.-J. Wiese, Phys. Rev. Lett. **77**, 5130 (1996). 11, 86

[23] N. Prokofev, B. Svistunov, and I. Tupitsyn, Journal of Experimental and Theoretical Physics **87**, 310 (1998). 11

[24] A. W. Sandvik, Phys. Rev. B **59**, R14157 (1999). 11, 82

[25] O. F. Syljuåsen and A. W. Sandvik, Phys. Rev. E **66**, 046701 (2002). 11, 82

[26] J. E. Gubernatis, M. Jarrell, R. N. Silver, and D. S. Sivia, Phys. Rev. B **44**, 6011 (1991). 13, 89

[27] W. von der Linden, Applied Physics A: Materials Science & Processing **60**, 155 (1995). 13, 89

[28] D. Jaksch, C. Bruder, J. I. Cirac, C. W. Gardiner, and P. Zoller, Phys. Rev. Lett. **81**, 3108 (1998). 17, 18, 56, 57

[29] W. Zwerger, J. Opt. B **5**, S9 (2003). 19, 68

[30] X. Du *et al.*, http://arxiv.org/abs/0704.2623 (2007). 19, 56

[31] N. Fabbri *et al.*, Phys. Rev. A **79**, 043623 (2009). 19, 56, 67, 68, 69

[32] W. S. Bakr *et al.*, Science **329**, 547 (2010). 19

[33] A. D. Greentree, C. Tahan, J. H. Cole, and L. C. L. Hollenberg, Nat. Phys. **2**, 856 (2006). 19, 24, 26, 27, 29, 31, 41, 50

[34] M. J. Hartmann, F. G. S. L. Brandão, and M. B. Plenio, Nat. Phys. **2**, 849 (2006). 19, 24, 26

[35] D. G. Angelakis, M. F. Santos, and S. Bose, Phys. Rev. A **76**, 031805(R) (2007). 19, 26, 27

[36] M. J. Hartmann and M. B. Plenio, Phys. Rev. Lett. **100**, 070602 (2008). 19, 26

[37] E. T. Jaynes and F. W. Cummings, Proc. IEEE **51**, 89 (1963). 20, 26, 45

[38] M. P. A. Fisher, P. B. Weichman, G. Grinstein, and D. S. Fisher, Phys. Rev. B **40**, 546 (1989). 24, 29, 30, 31, 33, 44, 50, 51, 57

[39] M. Greiner, O. Mandel, T. Esslinger, T. W. Hänsch, and I. Bloch, Nature **415**, 39 (2002). 24

[40] K. M. Birnbaum *et al.*, Nature **436**, 87 (2005). 24

[41] F. Brennecke *et al.*, Nature **450**, 268 (2007). 24

[42] J. M. Fink *et al.*, Nature **454**, 315 (2008). 24

[43] M. J. Bhaseen, M. Hohenadler, A. O. Silver, and B. D. Simons, arXiv:0812.0356 (2008). 24, 25, 27

[44] J. Koch and K. L. Hur, Physical Review A **80**, 023811 (2009). 24, 27, 29, 31, 51, 52

[45] W. Zwerger, J. Opt. B: Quantum Semiclass. Opt. **5**, 9 (2003). 24

[46] K. Sheshadri, H. R. Krishnamurthy, R. Pandit, and T. V. Ramakrishnan, Europhys. Lett. **22**, 257 (1993). 25, 33

[47] N. Elstner and H. Monien, Phys. Rev. B **59**, 12184 (1999). 25, 31, 33, 57

[48] T. D. Kühner, S. R. White, and H. Monien, Phys. Rev. B **61**, 12474 (2000). 25, 26, 29, 30, 31, 57

[49] R. Roth and K. Burnett, J. Phys. B: At. Mol. Opt. Phys. **37**, 3893 (2004). 25, 26, 38, 39, 57

[50] G. G. Batrouni, F. F. Assaad, R. T. Scaletter, and P. J. H. Denteneer, Phys. Rev. A **72**, 031601(R) (2005). 25, 26, 39, 57

[51] K. Sengupta and N. Dupuis, Phys. Rev. A **71**, 033629 (2005). 25, 33, 35, 57, 61, 62

[52] W. Koller and N. Dupuis, J. Phys.: Condens. Matter **18**, 9525 (2006). 25, 26, 33, 57

[53] S. D. Huber, E. Altman, H. P. Büchler, and G. Blatter, Phys. Rev. B **75**, 085106 (2007). 25, 33, 35, 36, 38, 39, 57, 60, 61

[54] B. Capogrosso-Sansone, S. G. Söyler, N. Prokof'ev, and B. Svistunov, Phys. Rev. A **77**, 015602 (2008). 25, 32, 33, 44, 56, 57

[55] B. Capogrosso-Sansone, N. V. Prokof'ev, and B. V. Svistunov, Phys. Rev. B **75**, 134302 (2007). 25, 32, 51, 57

[56] M. Ohliger and A. Pelster, arXiv:0810:4399v1 (2008). 25, 31, 33

[57] C. Menotti and N. Trivedi, Phys. Rev. B **77**, 235120 (2008). 25, 32, 33, 35, 36, 61

[58] M. Aichhorn, M. Hohenadler, C. Tahan, and P. B. Littlewood, Phys. Rev. Lett. **100**, 216401 (2008). 25, 26, 27, 29, 31, 33, 39, 46, 48, 50

[59] S. Schmidt and G. Blatter, Physical Review Letters **103**, 086403 (2009). 25, 27, 29, 31, 39, 41, 44, 51, 52

[60] A. Griffin, *Excitations in a Bose-Condensed Liquid* (Cambridge University Press, 1993). 25, 26, 38

[61] E. K. Irish, C. D. Ogden, and M. S. Kim, Phys. Rev. A **77**, 033801 (2008). 25, 27, 48, 50

[62] S. C. Lei and R. K. Lee, Phys. Rev. A **77**, 033827 (2008). 25, 27

[63] E. K. Irish, arXiv:0903.3380 (2009). 25, 27, 42

[64] J. Cho, D. G. Angelakis, and S. Bose, arXiv:0807.1802v2 (2008). 25

[65] J. K. Freericks and H. Monien, Phys. Rev. B **53**, 2691 (1996). 25, 31

[66] L. Pollet, S. M. A. Rombouts, and P. J. H. Denteneer, Phys. Rev. Lett. **93**, 210401 (2004). 25, 32

[67] O. F. Syljuåsen and A. W. Sandvik, Phys. Rev. E **66**, 046701 (2002). 25, 27, 58

[68] A. Griffin and H. Shi, Phys. Rep. **304**, 1 (1998). 26

[69] M. I. Makin, J. H. Cole, C. Tahan, L. C. L. Hollenberg, and A. D. Greentree, arXiv:0710.5748 (2007). 26, 27, 29, 46, 48

[70] D. Rossini and R. Fazio, Phys. Rev. Lett. **99**, 186401 (2007). 27, 29, 30, 31

[71] D. Rossini, R. Fazio, and G. Santoro, EPL **83**, 47011 (2008). 27, 42

[72] J. Koch *et al.*, Phys. Rev. A **76**, 042319 (2007). 27

[73] H. G. Evertz, Adv. Phys. **52**, 1 (2003). 27, 58

[74] A. Albuquerque *et al.*, J. Magn. Magn. Mater. , 1187 (2007). 27, 53, 58, 66

[75] M. Troyer, B. Ammon, and E. Heeb, Lecture Notes in Computer Science **1505**, 191 (1998). 27, 53, 58

[76] F. Alet, S. Wessel, and M. Troyer, Phys. Rev. E **71**, 036706 (2005). 27, 53, 58, 66

[77] F. Michel and H. G. Evertz, arXiv.org/0705.0799 (2007). 28, 58

[78] E. L. Pollock and D. M. Ceperley, Phys. Rev. B **36**, 8343 (1987). 28

[79] N. V. Prokofev and B. V. Svistunov, Phys. Rev. B **61**, 11282 (2000). 28

[80] J. Zhao, A. W. Sandvik, and K. Ueda, arXiv:0806.3603v1 (2008). 29, 32, 48, 50, 51

[81] J. K. Freericks and H. Monien, Europhys. Lett. **26**, 545 (1994). 31

[82] T. D. Kühner and H. Monien, Phys. Rev. B **58**, R14741 (1998). 31

[83] F. Gerbier, Phys. Rev. Lett. **99**, 120405 (2007). 31, 32, 46

[84] F. Alet and E. S. Sorensen, Phys. Rev. B **70**, 024513 (2004). 32, 51

[85] B. Paredes *et al.*, Nature **429**, 277 (2004). 32

[86] N. Fabbri *et al.*, arXiv:0901.1805 (2009). 32

[87] N. N. Bogolyubov, J. Phys. (USSR) **11**, 23 (1947). 32

[88] J. M. Vogels, K. Xu, C. Raman, J. R. Abo-Shaeer, and W. Ketterle, Phys. Rev. Lett. **88**, 060402 (2002). 32

[89] A. M. Rey *et al.*, Journal of Physics B: Atomic, Molecular and Optical Physics **36**, 825 (2003). 32, 34, 35

[90] D. van Oosten, P. van der Straten, and H. T. C. Stoof, Phys. Rev. A **63**, 053601 (2001). 33, 34, 35

[91] X. Lu, J. Li, and Y. Yu, Physical Review A (Atomic, Molecular, and Optical Physics) **73**, 043607 (2006). 33, 46

[92] A. B. Bhattacherjee, Journal of Physics B: Atomic, Molecular and Optical Physics **40**, 143 (2007). 33

[93] D. B. M. Dickerscheid, D. van Oosten, P. J. H. Denteneer, and H. T. C. Stoof, Phys. Rev. A **68**, 043623 (2003). 46, 48

[94] L. I. Plimak, M. K. Olsen, and M. Fleischhauer, Phys. Rev. A **70**, 013611 (2004). 46

[95] N. B. Narozhny, J. J. Sanchez-Mondragon, and J. H. Eberly, Phys. Rev. A **23**, 236 (1981). 50

[96] G. G. Batrouni, R. T. Scaletter, and G. T. Zimanyi, Phys. Rev. Lett. **65**, 1765 (1990). 51

[97] K. Harada and N. Kawashima, J. Phys. Soc. Jpn. **67**, 2768 (1998). 51

[98] K. Sheshadri, H. R. Krishnamurthy, R. Pandit, and T. V. Ramakrishnan, Europhys. Lett. **22**, 257 (1993). 57, 61

[99] D. van Oosten, P. van der Straten, and H. T. C. Stoof, Phys. Rev. A **63**, 053601 (2001). 57

[100] Y. Ohashi, M. Kitaura, and H. Matsumoto, Physical Review A **73**, 033617 (2006). 57, 61

[101] M. Knap, E. Arrigoni, and W. von der Linden, Phys. Rev. B **81**, 024301 (2010). 57, 58, 59

[102] M. Knap, E. Arrigoni, and W. von der Linden, arXiv:1002.2449 (2010). 57, 60

[103] V. N. Golovach, A. Minguzzi, and L. I. Glazman, 0907.0483 (2009). 57, 60, 73

[104] A. M. Rey, P. B. Blakie, G. Pupillo, C. J. Williams, and C. W. Clark, Phys. Rev. A **72**, 023407 (2005). 60

[105] D. Clément, N. Fabbri, L. Fallani, C. Fort, and M. Inguscio, New Journal of Physics **11**, 103030 (2009). 67

[106] D. Clément, N. Fabbri, L. Fallani, C. Fort, and M. Inguscio, Journal of Low Temperature Physics **158**, 5 (2010). 67, 73

[107] M. Rigol and A. Muramatsu, Phys. Rev. A **69**, 053612 (2004). 69

[108] G. G. Batrouni, H. R. Krishnamurthy, K. W. Mahmud, V. G. Rousseau, and R. T. Scalettar, Phys. Rev. A **78**, 023627 (2008). 69

[109] M. Rigol, G. G. Batrouni, V. G. Rousseau, and R. T. Scalettar, Phys. Rev. A **79**, 053605 (2009). 69

[110] S. Wessel, F. Alet, M. Troyer, and G. G. Batrouni, Phys. Rev. A **70**, 053615 (2004). 70

[111] Y. Kato, Q. Zhou, N. Kawashima, and N. Trivedi, Nat Phys **4**, 617 (2008). 71

[112] D. Jaksch, Physics **2**, 29 (2009). 72

[113] M. Knap, E. Arrigoni, and W. von der Linden, arXiv:1007.2716 (2010). 73

[114] H. Seo, C. Hotta, and H. Fukuyama, Chem. Rev. **104**, 5005 (2004). 79

[115] R. H. McKenzie, C. J. Hamer, and D. W. Murray, Phys. Rev. B **53**, 9676 (1996). 80, 81, 119

[116] G. Benfatto, G. Gallavotti, and J. Lebowitz, Helvetica Physica Acta , 312 (1995). 81

[117] J. E. Hirsch and E. Fradkin, Phys. Rev. B **27**, 4302 (1983). 81, 120

[118] H. Zheng, D. Feinberg, and M. Avignon, Phys. Rev. B **39**, 9405 (1989). 81

[119] L. G. Caron and C. Bourbonnais, Phys. Rev. B **29**, 4230 (1984). 81

[120] R. J. Bursill, R. H. McKenzie, and C. J. Hamer, Phys. Rev. Lett. **80**, 5607 (1998). 81, 119, 120

[121] E. Jeckelmann, C. Zhang, and S. R. White, Phys. Rev. B **60**, 7950 (1999). 81, 119, 120

[122] A. Weiße and H. Fehske, Phys. Rev. B **58**, 13526 (1998). 81, 119

[123] M. Hohenadler, G. Wellein, A. R. Bishop, A. Alvermann, and H. Fehske, Phys. Rev. B **73**, 245120 (2006). 81, 92, 93, 95, 119, 120

[124] S. Sykora, A. Hübsch, K. W. Becker, G. Wellein, and H. Fehske, Phys. Rev. B **71**, 045112 (2005). 81, 92, 95, 119

[125] S. Sykora, A. Hübsch, and K. W. Becker, Europhys. Lett. **76**, 644 (2006). 81, 92, 95, 119

[126] C. E. Creffield, G. Sangiovanni, and M. Capone, Eur. Phys. J. B **44**, 145 (2005). 81, 120

[127] F. F. Assaad and T. C. Lang, Phys. Rev. B **76**, 035116 (2007). 81

[128] F. F. Assaad, Phys. Rev. B **78**, 155124 (2008). 81

[129] M. Kohno, M. Arikawa, J. Sato, and K. Sakai, 1002.1147 (2010). 90

[130] S. Sykora, A. Hübsch, and K. Becker, Eur. Phys. J. B **51**, 181 (2006). 119

[131] C. Zhang, E. Jeckelmann, and S. R. White, Phys. Rev. Lett. **80**, 2661 (1998). 119, 120

[132] A. W. e, H. Fehske, G. Wellein, and A. R. Bishop, Phys. Rev. B **62**, R747 (2000). 119

[133] G. Wellein and H. Fehske, Phys. Rev. B **58**, 6208 (1998). 119

[134] E. Jeckelmann and S. R. White, Phys. Rev. B **57**, 6376 (1998). 120

[135] H. Fehske *et al.*, Physica B **359-361**, 699 (2005). 120

[136] S. Ejima and H. Fehske, EPL **87**, 6 (2009). 120

[137] J. Loos, M. Hohenadler, A. Alvermann, and H. Fehske, Journal of Physics: Condensed Matter **19**, 236233 (2007). 120

[138] B. Lau, M. Berciu, and G. A. Sawatzky, Phys. Rev. B **76**, 174305 (2007). 120